# COPSE reloaded: An improved model of biogeochemical cycling over Phanerozoic time

**Timothy M. Lenton[a]*, Stuart J. Daines[a], Benjamin J. W. Mills[b]**

[a]Earth System Science group, College of Life and Environmental Sciences, University of Exeter, Exeter EX4 4QE, UK

[b]School of Earth and Environment, University of Leeds, Leeds LS2 9TJ, UK

*Corresponding author: Tim Lenton

E-mail address: t.m.lenton@exeter.ac.uk

Full postal address: Earth System Science group, College of Life and Environmental Sciences, University of Exeter, Laver Building (Level 7), North Park Road, Exeter EX4 4QE, UK

## Abstract

The 'COPSE' (Carbon, Oxygen, Phosphorus, Sulphur and Evolution) biogeochemical model predicts the coupled histories and controls on atmospheric $O_2$, $CO_2$ and ocean composition over Phanerozoic time. The forwards modelling approach utilized in COPSE makes it a useful tool for testing mechanistic hypotheses against geochemical data and it has been extended and altered a number of times since being published in 2004. Here we undertake a wholesale revision of the model, incorporating: (1) elaboration and updating of the external forcing factors; (2) improved representation of existing processes, including plant effects on weathering and ocean anoxia; (3) inclusion of additional processes and tracers, including seafloor weathering, volcanic rock weathering and $^{87}Sr/^{86}Sr$; (4) updating of the present-day baseline fluxes; and (5) a more efficient and robust numerical scheme. A key aim is to explore how sensitive predictions of atmospheric $CO_2$,

$O_2$ and ocean composition are to model updates and ongoing uncertainties. The revised model reasonably captures the long-term trends in Phanerozoic geochemical proxies for atmospheric $pCO_2$, $pO_2$, ocean [$SO_4$], carbonate $\delta^{13}C$, sulphate $\delta^{34}S$ and carbonate $^{87}Sr/^{86}Sr$. It predicts a two-phase drawdown of atmospheric $CO_2$ with the rise of land plants and associated cooling phases in the Late Ordovician and Devonian-early Carboniferous, followed by broad peaks of atmospheric $CO_2$ and temperature in the Triassic and mid-Cretaceous – although some of the structure in the $CO_2$ proxy record is missed. The model robustly predicts a mid-Paleozoic oxygenation event due to the earliest land plants, with $O_2$ rising from ~5% to >17% of the atmosphere and oxygenating the ocean. Thereafter, atmospheric $O_2$ is effectively regulated with remaining fluctuations being a Carboniferous-Permian $O_2$ peak ~26% linked to burial of terrestrial organic matter in coal swamps, a Triassic-Jurassic $O_2$ minimum ~21% linked to low uplift, a Cretaceous $O_2$ peak ~26% linked to high degassing and weathering fluxes, and a Cenozoic $O_2$ decline.

## Keywords

Phanerozoic; Biogeochemistry; Carbon; Oxygen; Climate; Modelling

## 1. Introduction

How the composition of the atmosphere and the global biogeochemical cycling of major elements have changed over geologic time is a subject of broad inter-disciplinary interest. In particular atmospheric $CO_2$ and $O_2$ are 'master variables' of the Earth system that have been affected by both geological drivers and biological evolution (Lenton and Watson, 2011). Variations in atmospheric $CO_2$ are in turn a key contributor to long-term climate regulation (Walker et al., 1981), and variations in atmospheric $O_2$ have been linked to the evolution of aerobic life forms (Sperling et al., 2015a). The Phanerozoic is the best studied Eon with the most data. Yet despite numerous proxies to reconstruct past atmospheric $CO_2$ levels there are still lingering disagreements among those proxies and important gaps in the record especially before ~420 Ma (Royer, 2014). For past atmospheric $O_2$

46 levels there are only indirect constraints during parts of the Phanerozoic (Bergman et al., 2004). The
47 best established constraint on $O_2$ is a lower limit of 15-17% from combustion experiments combined
48 with the near continuous presence of fossil charcoal over the past ~420 Myr (Belcher and McElwain,
49 2008; Glasspool et al., 2004; Scott and Glaspool, 2006). A more uncertain upper limit on $O_2$ of 25-
50 35% has been inferred from the sensitivity of fire frequency to increasing $O_2$ and the continuous
51 presence of forests over the past ~370 Myr (Glasspool and Scott, 2010; Lenton and Watson, 2000b).

52 The limitations of the proxy record mean that models, combined with data, have a key role to play in
53 trying to reconstruct past variations in atmospheric $CO_2$ and $O_2$. However, model predictions should
54 not be confused with reality. In particular, inferences about the supposed effects of predicted
55 variations in atmospheric $O_2$ on animal evolution (Berner et al., 2007; Falkowski et al., 2005; Graham
56 et al., 1995; Graham et al., 2016) should be treated with caution, given that there are already several
57 quite different model predictions of Phanerozoic $O_2$ variations (Mills et al., 2016). Before making
58 such inferential leaps, the focus should be on which (if any) of the features in past $O_2$ (and $CO_2$)
59 reconstructions are robust to model and data uncertainty.

60 The aim of this paper is therefore to try to better understand, mechanistically and quantitatively, the
61 controls on atmospheric $CO_2$ and $O_2$ over Phanerozoic time, and to assess how sensitive predictions
62 of these variables are to factors we are scientifically uncertain about. To undertake such an exercise
63 we need to be clear about our scientific method and specifically the role we want a model to play in
64 gaining knowledge (our epistemology). Hence we start by briefly reviewing existing approaches to
65 modelling Phanerozoic biogeochemical cycling.

## 66 1.1. Review of existing modelling approaches

67 All models of biogeochemical cycling over Phanerozoic timescales typically have some
68 representation of sedimentary reservoirs (e.g. of carbon and sulphur in reduced and oxidised forms)
69 coupled to much smaller ocean-atmosphere reservoirs (e.g. of carbon, oxygen and sulphate).

However, there are two very different ways in which the models are used to try and gain knowledge; the inverse (data-driven) and forwards modelling approaches (Fig. 1).

Most previous studies following Garrels and Lerman (1981; 1984), and including the GEOCARB family of models (Berner, 1991, 1994, 2006a; Berner and Kothavala, 2001), have taken the inverse (data-driven) modelling approach (Fig. 1a). Whilst some models are driven by rock abundance data (Berner and Canfield, 1989), most are driven by isotopic data, notably the $\delta^{13}C$ and $\delta^{34}S$ records and a set of associated assumptions about how they are related to key processes (burial of organic carbon and pyrite sulphur, respectively). This leaves the only remaining data to test the model against as the uncertain proxies for $CO_2$ (Royer, 2014), and the even sparser and more uncertain constraints on $O_2$. Furthermore it is unclear how strongly reconstructing $CO_2$ constrains past $O_2$ variations (or *vice versa*). Such isotope-driven models are sensitive to the chosen $\delta^{13}C$ and $\delta^{34}S$ input data, particularly in their predictions of atmospheric $O_2$ (Mills et al., 2016), yet these isotope records are imperfectly known with considerable regional variations superimposed on an underlying global signal. Isotope-driven model predictions, particularly of $O_2$, are also sensitive to assumptions made about the carbon and sulphur isotope mass balances, to the extent that they are unable to produce plausible reconstructions of atmospheric $O_2$ without assuming sensitivity of C and S isotope fractionation to $O_2$, which provides stabilising negative feedback (Berner et al., 2000; Lasaga, 1989). Isotope-driven models have also typically had to assume 'rapid recycling' of deposited sediments, whereby sedimentary rock reservoirs are divided into 'young' (rapidly recycled) and 'old' components – with the young sedimentary reservoirs assumed to be comparable in size to the ocean-atmosphere reservoirs of C and S, and the old reservoirs typically assumed to be much larger and constant in size. This introduces another form of negative feedback whereby changes in the burial of reduced or oxidised carbon or sulphur are relatively rapidly counteracted by changes in the size and isotopic composition of the young reservoirs (Berner, 1987).

In designing the original COPSE model a different, forwards modelling approach was taken (Fig. 1b). A key target was to predict $\delta^{13}C$ and $\delta^{34}S$ records for comparison to data – as a means of testing the model's external forcing assumptions and internal mechanistic assumptions (Bergman et al., 2004). This means that COPSE explicitly simulates relevant biogeochemical fluxes such as organic carbon and pyrite sulphur burial (as a function of other variables and forcing parameters) rather than simply driving them with the isotope records. To this end nutrient (P, N) cycling is explicitly represented – a major difference from the GEOCARB family of inverse models – and a range of feedbacks in the coupled C, O, P, S and N cycles are considered. Notably, plausible predictions of atmospheric $O_2$ variation are achieved by assuming some negative feedback(s) within the surface Earth system between $O_2$ and its sink and/or source fluxes, and several of these candidate feedbacks are mediated by phosphorus cycling (Lenton and Watson, 2000b). The model does not assume rapid recycling of recently deposited sediments (although this may be a geologically reasonable mechanism). Nor does it assume constant sized ancient sedimentary reservoirs (which are hard to justify over Phanerozoic timescales). Instead, for simplicity, single, variable sedimentary reservoirs are assumed for organic carbon, carbonate carbon, pyrite, and gypsum.

A more elaborate forwards model is MAGic (Arvidson et al., 2006, 2011, 2013, 2014; Guidry et al., 2007), which shares elements in common with both COPSE and GEOCARB and is particularly focused on the inorganic side of the carbon cycle. MAGic tracks atmospheric $CO_2$ and $O_2$ and includes a much more detailed approach to ocean composition and the rock cycle than either GEOCARB or COPSE, with a total of 40 state variables. It tracks seven major ions of seawater (using a Pitzer approach to computing activities), plus phosphate as a limiting nutrient, and marine organic matter. It distinguishes a range of crystalline continental rocks (silicates), shelf/continental sediments and sedimentary rocks, sediments buried in deep cratons, seafloor basalt components, pelagic (deep ocean floor) sediments, and clays. MAGic includes feedback on atmospheric $CO_2$ from silicate weathering and feedback on atmospheric $O_2$ from redox-dependent phosphorus burial/recycling (Van Cappellen and Ingall, 1996). The model is driven by a range of geological forcing factors taken

120 from GEOCARB III (Berner and Kothavala, 2001), BLAG (Berner et al., 1983), and rock abundance data
121 (including coal). It is not driven by isotope records, nor are these used as a model prediction target.
122 Instead model predictions are compared to $CO_2$ proxies and to reconstructions of ocean
123 composition. A key difference from COPSE is that the burial flux of terrestrially-derived organic
124 carbon is assumed to be tiny (Arvidson et al., 2006). Hence there is no predicted secular change in
125 atmospheric oxygen levels with the rise of land plants, although greatly enhanced coal deposition in
126 the Carboniferous-Permian is sufficient to drive a predicted $O_2$ peak at that time (Arvidson et al.,
127 2013).

128 Whilst both forwards and inverse modelling approaches have merits, the scope for testing the
129 predictions of inverse modelling against data is limited by design – because much of the available
130 data has gone into the model as drivers. As so many factors concerning the drivers and feedbacks
131 controlling atmospheric $CO_2$ and $O_2$ are uncertain, and given that we only have uncertain proxies for
132 $CO_2$ and a lower bound on $O_2$ (neither of which extend to the early Paleozoic), we continue to pursue
133 the forwards modelling approach here – because it gives us several more opportunities to test our
134 understanding and hypotheses (as represented by the model) against independent data (proxy
135 records). One of the key aims here is to see to what degree those proxy records constrain the model
136 mechanisms.

137 Both of the existing modelling approaches have revealed some useful lessons as to how to model
138 the coupled histories of $CO_2$ and $O_2$. In particular, there are several good reasons to first understand
139 what controls atmospheric $CO_2$ and then try to understand what controls $O_2$. Firstly, ocean-
140 atmosphere carbon has a shorter residence time than oxygen (at least after the early Paleozoic) so
141 $CO_2$ can be treated as at steady state on a ~1 Myr timescale over which $O_2$ varies. Secondly, the
142 control exerted by the $CO_2$ cycle on the $O_2$ cycle appears to be stronger than *vice versa* (Bergman et
143 al., 2004). Thirdly, our understanding of controls on atmospheric $CO_2$ is more broadly agreed upon
144 than our understanding of controls on $O_2$ – notwithstanding some on-running discussion about the

cause(s) of Cenozoic $CO_2$ change (e.g. Caves et al., 2016; Li and Elderfield, 2013; Mills et al., 2014a; Torres et al., 2014; Willenbring and von Blanckenburg, 2010).

Existing models suggest that long-term atmospheric $CO_2$ concentration is governed largely by geologic and biologic forcing factors and by the functional dependencies of terrestrial silicate weathering and seafloor weathering on $CO_2$ and/or temperature, which provide negative feedback. Whilst organic carbon burial is an important sink of $CO_2$ and provides coupling to the $O_2$ cycle (where it is the major source of $O_2$), in current models it only exerts second-order control on $CO_2$ (Bergman et al., 2004; Berner, 2006a). However, variations in $O_2$ may significantly affect vegetation and thus silicate weathering and $CO_2$ (Bergman et al., 2004).

Understanding what controls atmospheric $O_2$ (and at what resulting levels) remains an outstanding puzzle, with a wider range of feedbacks proposed than for $CO_2$ (Kump, 1988; Lenton and Watson, 2000b; Van Cappellen and Ingall, 1996), together with biologic and geologic forcing. The coupling from the $CO_2$ cycle to the $O_2$ cycle may be of first-order importance, with silicate and carbonate weathering potentially providing a large fraction of the phosphorus supply that can ultimately determine organic carbon burial, which is the dominant source of oxygen (Bergman et al., 2004; Lenton et al., 2014). However, selective weathering of phosphorus by plants could act to decouple silicate weathering and organic carbon burial (Lenton et al., 2012, 2016). Changes in the C/P ratio of buried organic matter, especially a large increase in this ratio with the rise of land plants, also exert first-order control on $O_2$ (Bergman et al., 2004; Berner, 1989; Kump, 1988; Lenton et al., 2016). Furthermore, it has been argued that erosion rates exert a first-order control on organic carbon burial (Berner, 2006a; Blair and Aller, 2012; Hedges and Keil, 1995), providing a further coupling between the $CO_2$ and $O_2$ cycles insofar as physical weathering rates control chemical weathering rates and thereby increases in erosion may decrease $CO_2$ and increase $O_2$.

## 1.2. Motivation and aims

In keeping with the original COPSE study (Bergman et al., 2004), our aim here is to produce a quantitative model that incarnates various mechanistic hypotheses and makes resulting predictions which can be tested against multiple, independent proxy data constraints.

We have several reasons to update the COPSE model. Firstly, some of the model assumptions have been critiqued, suggesting alternative hypotheses to test, including the aforementioned argument that organic carbon burial is controlled more by erosion fluxes than by phosphorus supply (Berner, 2006a). Secondly, although the original COPSE model sought to make the model forcing independent of isotope inversion, the forcing of uplift was ultimately derived from inversion of the strontium isotope record – an inconsistency which we have subsequently addressed for the Mesozoic and Cenozoic by making $^{87}Sr/^{86}Sr$ a predicted variable (Mills et al., 2014a). This modification gives an additional target to test the model against, especially given previously published difficulties in fitting the complete Phanerozoic strontium isotope record (Francois and Walker, 1992). Thirdly, the field of Phanerozoic modelling has advanced. Notably Bob Berner published a combined model of Phanerozoic atmospheric $O_2$ and $CO_2$, GEOCARBSULF (Berner, 2006a), which he subsequently updated to distinguish weathering of volcanic rocks (Berner, 2006b), and revised carbon isotope forcing data and fractionation (Berner, 2009). The importance of volcanic rock weathering in $CO_2$ consumption has been more widely recognised with the emplacement of large igneous provinces (LIPs) linked to both short-term release and long-term drawdown of $CO_2$ (Schaller et al., 2011), and phosphorus supply from volcanic rock weathering linked to organic carbon burial (Horton, 2015). Partly in response to this we began to extend COPSE to include LIP emplacement and volcanic rock weathering for the Mesozoic-Cenozoic (Mills et al., 2014a). New work on the biogeochemical effects of early plants also motivated other updates to the Paleozoic predictions of COPSE (Lenton et al., 2012, 2016). Finally, in the wider geochemical literature there have also been significant revisions to

192 estimates of key fluxes in the coupled C, O, P and S cycles, for example silicate weathering
193 (Hartmann et al., 2009; Moon et al., 2014).

194 In the following we undertake a thorough review, reconsideration and revision (where warranted),
195 of all aspects of the COPSE model, including bringing together developments of the model since the
196 original paper (Lenton, 2013; Lenton et al., 2012, 2016; Mills et al., 2014a). Our central aim is to
197 illustrate for the reader the effects of the many uncertain aspects of the coupled C, O, P, and S cycles
198 on long-term predictions of atmospheric $CO_2$, $O_2$, and ocean composition. In keeping with the
199 philosophy behind the model, we use it as a framework to test mechanistic hypotheses, by making
200 quantitative predictions of $\delta^{13}C$, $\delta^{34}S$, $^{87}Sr/^{86}Sr$, alongside $CO_2$ and $O_2$, which are tested against
201 available data. This evaluation of input assumptions and different mechanistic hypotheses ultimately
202 leads to an assessment of which predicted features of Phanerozoic variation in atmospheric $CO_2$, $O_2$
203 and ocean composition are robust to current uncertainties, and which critical uncertainties remain
204 that could be targeted by future work. The remainder of the paper is structured as follows: Section 2
205 describes a comprehensive series of updates to the COPSE model. Section 3 tests their effects by
206 comparing the resulting predictions against multiple proxy records, and arrives at a new baseline
207 model. Section 4 concludes.

208 ## 2. Model description

209 A schematic of the revised COPSE model structure is shown in Figure 2. Panel A shows the mass
210 fluxes in the linked C-S-O cycles, which feature in both COPSE and GEOCARBSULF. Panel B shows the
211 feedback-based biosphere component, which is unique to COPSE and is used to calculate the burial
212 fluxes of organic carbon and pyrite sulphur in a forwards manner from other model processes (as
213 opposed to inferring these fluxes through isotope mass balance as in e.g. GEOCARBSULF). All terms
214 in Figure 2 are defined in Tables 1 and 2.

Our revision of the model spans changes to its internal structure, changes to its parameters, and changes to the forcing factors driving it. We start by introducing the model reservoirs, i.e. state variables, and the most fundamental structural changes, i.e. addition of new fluxes. Next we describe changes to the model forcing factors. Then we work through the model processes and corresponding equations, including some further structural changes at the level of changing functional dependencies. Finally we consider changes to the baseline fluxes of the model.

## 2.1. Reservoirs and new fluxes

The revised COPSE model retains at its core the coupled C, O, P and S cycles, and an oceanic cycle of N. Sr is added as an illustrative tracer cycle (which does not affect the overall dynamics) (Mills et al., 2014a). The oceanic N and P cycles are tightly coupled such that versions of the model that remove the N cycle and relate new production directly to P concentration give comparable results (Lenton et al., 2012), but we retain both cycles here.

In previous updates to the model, some new fluxes have been introduced (Mills et al., 2014a), notably seafloor weathering is included as a sink of $CO_2$, and terrestrial silicate weathering is subdivided into contributions from volcanic rocks (termed 'basalt') and from all other non-volcanic igneous silicate rocks (termed 'granite'). Here we also add pyrite and gypsum degassing fluxes of sulphur in line with GEOCARBSULF (Berner, 2006a). The original COPSE had a partial, interactive Ca cycle, but as gypsum degassing is a source of volatile S but not of Ca, whereas gypsum burial removes both Ca and S from the ocean, this poses a mass balance problem for Ca. Hence we opt to remove the partial, interactive Ca cycle from COPSE. Only the gypsum burial flux was related to modelled calcium, and we now relate this to a prescribed reconstructed change in ocean [Ca] (Horita et al., 2002). Modelling by others has given a more complete treatment of Ca variation over Phanerozoic time (Arvidson et al., 2013).

The core model includes surface reservoirs of atmosphere-ocean oxygen (***O***) and carbon (***A***), and oceanic nitrogen (***N***), phosphorus (***P***), and sulphur (***S***), with sedimentary rock reservoirs of organic

(reduced) carbon (***G***), carbonate (oxidised) carbon (***C***), pyrite (reduced) sulphur (***PYR***), and gypsum (oxidised) sulphur (***GYP***). These are shown as circles in Figure 2. In our notation, upper case bold italic lettering (e.g. ***A***) indicates reservoir size in moles and lower case bold italic lettering (e.g. ***a***) indicates reservoir size normalised to the present. Differential equations and present-day reservoir sizes are summarised in Table 1. The meaning of different flux terms and their original baseline values are introduced in Table 2. The additional tracer cycle of strontium includes ocean (***OSr***) and sedimentary carbonate (***CSr***) reservoirs. It is introduced briefly below and described in full in Appendix A.

## 2.2. Forcing factors

The original COPSE model was forced by changing solar insolation (*I*), metamorphic and volcanic degassing (*D*), tectonic uplift (*U*), plant evolution and land colonisation (*E*), plant enhancement of weathering (*W*), apportioning of carbonate burial between shallow and deep seas (*B*), and changing C:P burial ratio of terrestrial plant material ($CP_{land}$) (Table 3). Changing solar insolation is based on established stellar physics and is implicit in the time-dependent calculation of global temperature hence is not discussed further here. Subsequent work using COPSE has suggested several updates to the original geological and biological forcing factors (Fig. 3), and has introduced volcanic, non-volcanic and carbonate rock area, paleogeography effects on runoff (Mills et al., 2014a) and selective biotic weathering of P (Lenton et al., 2012, 2016) as additional forcing factors. Here we first describe further updates to the original set of forcing factors (Fig. 3) and then describe an expanded and updated list of additional forcing factors (Fig. 4). In developing the model we also explored yet further forcing factors (Table 3) which are not included here (in the interests of simplicity), because they had little effect or generated easily falsified results.

### 2.2.1. Degassing (*D*)

The controls on metamorphic and volcanic degassing (*D*) – here of sedimentary volatiles – are a subject of ongoing debate. On the longest timescales degassing is expected to be driven by the

Earth's decaying internal heat source, but with the supercontinent cycle and associated changes in plate tectonics causing substantial fluctuations about the long-term trend – including recent suggestions that more $CO_2$ degassing occurs at continental arcs than oceanic arcs (Lee et al., 2013; McKenzie et al., 2016). The original degassing forcing of COPSE followed GEOCARB II (Berner, 1994) in linking subduction rates to seafloor spreading rates estimated based on direct estimates of subduction for the last 180 Myr (Engebretson et al., 1992) and sea-level change prior to that (Gaffin, 1987). Recent work has linked degassing for the past 230 Myr to inferred subduction zone length from seismic tomographic imaging of subducted slabs (Van Der Meer et al., 2014), and this forcing has been tried in COPSE (Mills et al., 2014a). Other recent work has sought to quantitatively reconstruct plate tectonics through parts of Phanerozoic time, including changes in subduction zone length (Matthews et al., 2016). However, a complete Phanerozoic reconstruction is currently unavailable. Hence here instead we derive degassing using the original sea-level inversion approach (Gaffin, 1987) applied to a more recent Phanerozoic sea-level dataset (Haq, 2014; Haq and Al-Qahtani, 2005; Haq and Schutter, 2008). The original method (Gaffin, 1987) is simplified, with little effect on the results (Mills et al., 2017). The main change from updating the sea-level data is an increase in inferred degassing from the late Permian to the mid Cretaceous (Fig. 3a).

#### 2.2.2. Uplift ($U$)

Uplift forcing ($U$) is updated (Mills et al., 2014a), following GEOCARBSULF (Berner, 2006b; Royer et al., 2014), such that it is based on a polynomial fit to sediment accumulation rates over Phanerozoic time (Ronov, 1993) rather than inversion of the strontium isotope record. This produces a smoother forcing that follows the same long-term trend as the original forcing (Fig. 3b). It captures the overall modulation of uplift by the supercontinent cycle, but does not resolve specific orogenic events. In recent versions of GEOCARBSULF (Royer et al., 2014), variation in the uplift/erosion forcing is scaled down by a 2/3 power, but here we use the original smooth fit to the Ronov data, reasoning that this represents the supply of new rock available for chemical weathering. For application of the model to specific events within the Phanerozoic, and for capturing some of the fine-scale structure in the

strontium isotope record, the uplift forcing could be modulated to capture specific orogenic events, but we do not pursue this here.

### 2.2.3. Plant evolution (*E*)

We retain separate forcing factors for plant evolution (*E*) and plant effects on weathering (*W*) for consistency with earlier work, although they follow similar trajectories and are multiplied together where they appear in the model weathering equations. For plant evolution (*E*; Fig. 3c), we update the rise of the earliest non-vascular plants to capture their higher potential productivity and spatial coverage (Porada et al., 2016) with *E* increasing from 0 to 0.15 over 465 to 445 Ma (Lenton et al., 2016). We also revise the subsequent rise of rooted vascular plants, including forests, with *E* increasing more rapidly from *E*=0.15 at 400 Ma to *E*=1 at 350 Ma, in contrast to a slower rise to *E*=1 at 300 Ma in the original COPSE model, and a later starting rise from 380 Ma to 350 Ma in GEOCARBSULF.

### 2.2.4. Plant effects on weathering (*W*)

We update the effect of the earliest non-vascular plants on weathering (*W*; Fig. 3d) to capture stronger effects suggested by recent experimental results and ecophysiological modelling studies (Lenton et al., 2012; Porada et al., 2016) with *W* increasing from 0 to 0.75 over 465 to 445 Ma (Lenton et al., 2016). Here we also increase weathering amplification *W* from 0.75 to 1 over 400-350 Ma associated with the evolution of rooted vascular plants, including deep rooted trees. We correspondingly remove the original increase in weathering amplification with the Cretaceous rise of angiosperms (*W* from 0.75 to 1 over 115-100 Ma), which was taken from GEOCARB I and II (Berner, 1991; Berner, 1994), noting that GEOCARB III also explores no effect of angiosperms and opts for *W*=0.875 prior to angiosperms (Berner and Kothavala, 2001). Whilst there is some evidence that angiosperms can increase weathering rates relative to gymnosperms (Moulton et al., 2000), there is other evidence that they can suppress weathering rates (Andrews et al., 2008). Hence the assumption of no increase in weathering rates seems a reasonable baseline. In contrast to our

316 chosen forcing, GEOCARBSULF assumes that plants only start to affect weathering at 380 Ma with
317 the rise of trees and that a major increase to $W$=0.875 is complete by 350 Ma, with a further
318 increase to $W$=1 associated with the rise of angiosperms over 130 to 80 Ma (Royer et al., 2014).

319 ### 2.2.5. Plant stoichiometry ($CP_{land}$)

320 We update the forcing of land plant stoichiometry ($CP_{land}$; Fig. 3e) to capture a high C/P of earliest
321 non-vascular plants and associated peats. The original model assumed a default C/P = 1000 burial
322 ratio of terrestrially-derived organic matter but increased this to C/P = 2000 over 355-345 Ma then
323 decreased it back to C/P = 1000 over 290-280 Ma in a crude attempt to capture the effect of
324 abundant deposition of coals from swamps in the Carboniferous (and early Permian). Subsequent
325 work noted that non-vascular plant matter has a high C/P ~2000 (Lenton et al., 2016) and that
326 peatland transformation to coaly shales had started by the early Devonian (Kennedy et al., 2013).
327 Hence C/P was increased to 2000 with the rise of the first non-vascular plants, over 465-445 Ma
328 (retaining the decrease to C/P = 1000 over 290-280 Ma). Here we first adopt that forcing, then when
329 we introduce an additional forcing factor of coal basin depositional area ($b_{coal}$) we change the timing
330 of the decline of C/P to 345-300 Ma, to avoid excessive Carboniferous organic carbon burial as $b_{coal}$
331 ramps up over this interval.

332 ### 2.2.6. Pelagic calcification ($B$)

333 We update the shape of the shift in the location of carbonate burial from shelves to the deep sea
334 with the rise of pelagic calcifiers ($B$; Fig. 3f), which increases carbonate degassing. The approach
335 originally used in COPSE is from GEOCARB I and involves a sharp rise which then saturates. This can
336 be questioned given that the extra carbonate getting subducted should be an integral of what has
337 previously been deposited on slowly moving ocean plates, hence should not increase abruptly even
338 if the deposition flux increases abruptly. In GEOCARB II, Berner (1994) used a linear rise from 150-0
339 Ma and experimented with different initial values of 0.5 to 1 as well as the standard 0.75, showing

that this has a substantial effect on $CO_2$ predictions. Here we adopt the GEOCARBSULF choice of a linear rise from 0.75 to 1 over 150-0 Ma (Royer et al., 2014).

### 2.2.7. Volcanic silicate rock area ($a_{bas}$)

In recent work (Mills et al., 2014a) we introduced a distinction between volcanic silicate rocks (termed 'basalt') and non-volcanic silicate rocks (termed 'granite'), and a new normalised model forcing representing the exposed area of volcanic rocks ($a_{bas}$). This forcing captures the combined area of large igneous provinces and volcanic islands (ocean island basalts and island arcs). Here we extend this approach back in time using initial LIP areas from an updated version of the Large Igneous Provinces Commission compilation starting at 720 Ma (Ernst, 2014). The cumulative LIP area forcing was calculated assuming exponential decay with time of each individual LIP from their initial estimated area to their present area. Decay rates for each major LIP were set to retrieve their present day area, and an overall decay rate for other LIPs set to retrieve a cumulative present day area of $4.8 \times 10^6$ km$^2$ (Mills et al., 2014a). We assume volcanic island area scales with subduction-related degassing ($D$) as the majority of volcanic islands are linked to island arcs driven by crust subduction (Allegre et al., 2010). The resulting forcing shows a ~2.5 fold increase in volcanic rock area over Phanerozoic time (Fig. 4a).

We also estimated an additional contribution to degassing from the emplacement of large igneous provinces ($D_{LIP}$), but as this is only a small fraction of total degassing, the principal effects of which are on short-term events (Mills et al., 2014a), we do not include it here.

### 2.2.8. Non-volcanic silicate rock area ($a_{gran}$)

In previous work (Mills et al., 2014a), a normalised forcing of the area of non-volcanic silicate rocks ($a_{gran}$) was introduced, taken to be the remainder of total continental area (from GEOCARBSULF) minus exposed carbonate area (from GEOCARBSULF) minus volcanic rock area ($a_{bas}$). Here instead we estimate a kinetically-weighted area forcing of the non-volcanic component of silicate weathering ($a_{gran}$) based on the Phanerozoic paleogeology reconstructions of Bluth and Kump

(1991). We took the midpoint of geologic intervals from the latest geological timescale (Cohen et al., 2013; updated) and interpolated linearly between them. $a_{gran}$ is assumed to comprise cation contributions from shield rocks ($a_{sil}$) and from secondary minerals in sedimentary rocks ($a_{sed}$), which make a large contribution to today's non-volcanic silicate weathering flux (Amiotte-Suchet et al., 2003; Hartmann et al., 2009). 'Shales' have been estimated to contribute ~77% of the non-volcanic silicate weathering $CO_2$ consumption flux (Amiotte-Suchet et al., 2003), although a more sophisticated treatment of current lithology suggests that all non-carbonate sedimentary rocks contribute ~62% of the non-volcanic silicate weathering flux (or ~52% of total silicate weathering) (Hartmann et al., 2009). Hence we define $a_{gran} = k_{sed} \cdot a_{sed} + (1- k_{sed}) \cdot a_{sil}$, as a kinetic and area weighted forcing factor, and opt for $k_{sed} = 0.6$ as a reasonable estimate. The sedimentary rock types assumed to contribute significantly to silicate weathering are shales, coals, and evaporites. (Sandstone and siliceous chert are neglected because they do not contribute greatly to silicate weathering and COPSE does not keep track of their sedimentary reservoirs.) We sum together the areas of these three rock types to create a normalised forcing ($a_{sed}$), making one adjustment from the original dataset of Bluth and Kump (1991) in that we neglect an inferred sharp increase in exposed shale area from the Pliocene to the present (taking the Pliocene value as the present value). Exposed shield silicate area ($a_{sil}$) from Bluth and Kump (1991) shows a large decline over Phanerozoic time and replacement largely by sandstones, which (as they discuss) may be partly an artefact. In $a_{gran}$ it is somewhat counteracted by an increase in the area of shales, coals and evaporites, although $a_{gran}$ still declines by a factor ~2.5 over Phanerozoic time (Fig. 4b).

We also calculated normalised forcing factors for exposed areas of carbonate ($a_{carb}$), shale ($a_{shale}$), organics (shale + coal) ($a_{org}$), and evaporites ($a_{evap}$), and experimented with using them to force the weathering fluxes of carbonate ($a_{carb}$), pyrite ($a_{shale}$), organic carbon ($a_{org}$), and gypsum ($a_{evap}$), but leave them out here as they either failed to improve the results or clearly degraded them.

### 2.2.9. Paleogeography (*PG*)

Following GEOCARBSULF and Mills et al. (2014a), we consider an additional weathering forcing representing the combined effects of changes in paleogeography (*PG*) on global river runoff and on the fraction of land area undergoing chemical weathering (thus excluding dry regions) (Fig. 4c). For this we use GCM-based estimates that exclude the effects of changing $CO_2$ and solar luminosity (Royer et al., 2014), multiplying together their $f_D$ forcing and a normalised-to-present version of their $f_{Aw}/f_A$ forcing. We do not further scale the resulting forcing by total land area, as is done in GEOCARBSULF (Royer et al., 2014), because exposed areas of relevant rock types are dealt with separately.

### 2.2.10. Coal deposition ($b_{coal}$)

Coal deposition on land has at times been a significant contributor to global organic carbon burial, controlled by a combination of the occurrence of subsiding low-relief cratons and a moist climate (Nelsen et al., 2016). Following other Phanerozoic modelling studies, e.g. Bartdorff et al. (2008), here we add a coal basin depositional area forcing ($b_{coal}$, labelled '*b*' for burial to distinguish it from '*a*' for exposed area forcing), which is ultimately derived from data for coal abundance (Ronov, 1993) (and hence comparable to what Bluth and Kump, 1991, find for coal depositional area as that too is based on Ronov's data). $b_{coal}$ is normalised to 1 at present and has a peak of ~12 at the end of the Carboniferous (~300 Ma), but it falls to 0 prior to the Carboniferous, which is at odds with recent discoveries of early Devonian coaly shales (Kennedy et al., 2013) and with the observation that the earliest plants were tied to wetland settings by their physiology, so would be expected to have created peatlands. Hence we set $b_{coal} = 1$ initially until it starts to increase above that at ~345 Ma. The resulting fluctuations in coal depositional area (Fig. 4d) are only assumed to operate on the small fraction (~0.2; see below) of today's terrestrial organic carbon burial flux that is actually buried in coal basins rather than marine sediments, whereas changes in the C/P ratio of terrestrial organic matter will operate on the whole burial flux, whether burial occurs in terrestrial or marine settings. Hence when introducing $b_{coal}$ we combine it with $CP_{land}$ (rather than replacing it).

### 2.2.11. Selective biotic weathering of phosphorous (*F*)

An additional forcing factor (*F*) has previously been introduced that represents the selective biotic weathering of P relative to host rock dissolution (Lenton et al., 2012, 2016). This captures the observations that plants and their fungal mycorrhizal symbionts have evolved mechanisms to selectively 'mine' P-rich mineral inclusions in rocks, and experiments show large relative enhancements of P weathering relative to bulk cations (Ca, Mg) by non-vascular plants (Lenton et al., 2012; Quirk et al., 2015). Such selective P weathering represents a mechanism to decouple the inorganic (silicate weathering) and organic (carbon burial) sides of the carbon cycle. It may have been particularly pertinent when early plants were colonising fresh rock surfaces before the establishment of rooting systems, deeper soils and effective P recycling systems. Hence it has been used as a means of forcing mid-Paleozoic increases of organic carbon burial in COPSE (Lenton et al., 2012, 2016). Here we explore an increase from *F*=1 to *F*=1.5 over 465-445 Ma followed by a decrease from *F*=1.5 to *F*=1 over 410-400 Ma (Lenton et al., 2016) (Fig. 4e).

### 2.2.12. Calcium concentration ($c_{cal}$)

In place of the original interactive marine Ca reservoir we explore forcing gypsum burial with a prescribed variation in normalised marine [$Ca^{2+}$] ($c_{cal}$, where 'c' is for concentration) following the fit to the data in Figure 8 of Horita et al. (2002) (Fig. 4f). We also considered forcing gypsum burial with a changing evaporite depositional area ($b_{evap}$) derived from Bluth and Kump (1991), but this yielded readily falsifiable results so we do not include it here.

## 2.3. Variables

Changes to the model functions that are incorporated in the new baseline model are summarised in Table 4, and further alternative functions explored in the hypothesis testing are described in this section. Changes to the model non-flux parameters are summarised in Table 5 (changes to flux parameters are in Table 2). In the following we use a prime to indicate a normalised variable.

### 2.3.1. Atmospheric $CO_2$

Whereas the original model had a constant atmospheric fraction of the total ocean-atmosphere $CO_2$ reservoir, here atmospheric $CO_2$ (in PAL, i.e. normalised) is made proportional to the square of the total amount of carbon in the ocean and atmosphere (normalised variable $\boldsymbol{a}$) following Kump and Arthur (1999):

$$CO_2 = \boldsymbol{a}^2 \quad (1)$$

This makes minimal difference to steady state $CO_2$ predictions, but variations in the total ocean-atmosphere carbon reservoir ($\boldsymbol{A}$) are much reduced, allowing greater transient variations in $CO_2$ in studies of short-term events, including e.g. the early rise of plants. Present atmospheric $CO_2$ (1 PAL) is taken to correspond to a pre-industrial $pCO_2$ = 280 ppm, i.e. $pCO_2 = 280 \cdot CO_2$ (ppm).

### 2.3.2. Global temperature

In the interests of simplicity, model comparability, and ability to explore variations in climate sensitivity, we switch from the original global surface temperature ($T$) function of Caldeira and Kasting (1992) to the GEOCARB III temperature function (Berner and Kothavala, 2001) (which has a slightly different implicit variation in solar luminosity with time):

$$\Delta T = k_c \cdot \ln CO_2 - k_l \cdot t/570 \quad (2)$$

Where $k_c$ = 4.328°C corresponds to a climate sensitivity of 3°C for a doubling of $CO_2$ and $k_l$ = 7.4°C represents the sensitivity to changing solar luminosity, for time, $t$, in Myr ago. Present global temperature is taken to be 15°C hence $T = 15 + \Delta T$ (°C).

### 2.3.3. Net primary productivity

The dependence of global vegetation net primary productivity, $V_{npp}$, on temperature, $T$ (°C), $pCO_2$ (ppm) and $O_2$ (PAL) retains the original 'OCT' formulation:

$$V_{npp} = k_{npp} \cdot E \cdot (1.5 - 0.5 \cdot \boldsymbol{o}) \cdot \left(1 - \left(\frac{T-25}{25}\right)^2\right) \cdot \left(\frac{pCO_2 - P_{min}}{P_{1/2} + pCO_2 - P_{min}}\right) \quad (3)$$

Where $P_{min}$ = 10 ppm, $P_{1/2}$ = 183.6 ppm, and $k_{npp}$ = 2 is a normalising constant for present $T$ = 15°C and $pCO_2$ = 280 ppm. This represents a slightly weaker $CO_2$ fertilisation effect than the GEOCARB choices of $k_{CO2}$=2, $P_{min}$ = 0 ppm, $P_{1/2}$ = 280 ppm (but this has little effect on the results).

### 2.3.4. Fire effects on vegetation

We adjust the fire function following Lenton (2013) to be based on a fit to experimental results for fuel of 10% moisture content (rather than 20% moisture content in the original model):

$$ignit = min(max(48 \cdot mO_2 - 9.08, 0), 5) \quad (4)$$

where $mO_2$ (0.21 at present) is the volumetric mixing ratio of $O_2$ (mol/mol) assuming a constant remainder of the atmosphere dominated by $N_2$:

$$mO_2 = \frac{\boldsymbol{o}}{\boldsymbol{o}+k_{16}} \quad (5)$$

with $k_{16}$ = 3.762 (as before). The resulting equation for vegetation biomass is as before:

$$V = V_{npp} \cdot \frac{k_{fire}}{k_{fire} - 1 + ignit} \quad (6)$$

but we adopt $k_{fire}$ = 3 following Bond et al. (2005) and Lenton (2013), which equates to a 50% suppression of vegetation biomass by fires at present (relative to the case with no fires; $mO_2$ <0.19). Together this results in a fire feedback that lies intermediate in strength between the original weak (default) and strong formulations for increases in $O_2$, and provides stronger feedback against decreases in $O_2$ as fires have a limiting effect on vegetation down to $mO_2$ ~0.19, consistent with combustion experiments and spatial modelling of fire propagation (Belcher et al., 2010).

### 2.3.5. Degassing of carbon and sulphur

Carbonate degassing (*ccdeg*) and organic carbon degassing (*ocdeg*) retain their original functional forms (but the default fluxes are adjusted; see below):

$$ccdeg = k_{12} \cdot D \cdot B \cdot \boldsymbol{c} \quad (7)$$

$$ocdeg = k_{13} \cdot D \cdot \boldsymbol{g} \quad (8)$$

The revised model allows for the possibility of degassing fluxes of gypsum and pyrite:

$$gypdeg = k_{gypdeg} \cdot D \cdot \boldsymbol{gyp} \quad (9)$$

$$pyrdeg = k_{pyrdeg} \cdot D \cdot \boldsymbol{pyr} \quad (10)$$

Initially the sulphur degassing fluxes ($k_{gypdeg}$, $k_{pyrdeg}$) are set to zero consistent with the original model.

### 2.3.6. Seafloor weathering

The revised model includes a seafloor weathering sink of $CO_2$ which is assumed to scale with degassing (i.e. the rate of oceanic crust production). However, rather than have it depend on $CO_2$ (Mills et al., 2014a), a direct kinetic temperature dependence is applied:

$$sfw = k_{sfw} \cdot D \cdot e^{k_T^{sfw} \cdot \Delta T} \quad (11)$$

This assumes deep ocean temperature changes in proportion to global average temperature on long timescales. $k_T^{sfw}$ = 0.0608 corresponds to an activation energy (42 kJ mol$^{-1}$) appropriate for terrestrial basalt weathering, which we take as a default. However recent work suggest a much higher apparent activation energy for seafloor weathering 92±7 kJ mol$^{-1}$ ($k_T^{sfw}$ = 0.1332) implying stronger negative feedback (Coogan and Dosso, 2015), which we explore as an option below. (Seafloor basalt oxidation is also a sink of $O_2$ ~1x10$^{12}$ mol$O_2$ yr$^{-1}$ (Sleep, 2005) but this term in the oxygen balance is neglected here because it is assumed to scale with *D* in a similar way to organic carbon degassing.)

### 2.3.7. Plant effects on terrestrial weathering

The effects of plants on weathering are simplified from the original model, which multiplicatively applied the effect of plants on weathering term $V \cdot W$ leading to a mixing of abiotic and biotic responses. This could erroneously exceed (by up to ~56%) either end-member for intermediate values of $V \cdot W$ between 0 (abiotic) and 1 (biotic), making the effects of intermediate plant cover excessively strong. The original function also multiplied a Michaelis-Menten function of $CO_2$ for plant

productivity within *V* by another Michaelis-Menten function of $CO_2$ ($f_{plant}$) from GEOCARB, which was also originally intended to capture the $CO_2$ fertilisation effect on plant productivity. Here we include just one Michaelis-Menten $CO_2$ dependence within the variable *V*, which also encapsulates the plant evolution forcing factor *E*. Our simplified effect of biota (or lack of it) on weathering is:

$$f_{biota} = \left[(1 - \min(V \cdot W, 1)) \cdot k_{15} \cdot {CO_2}^{0.5} + V \cdot W\right] \quad (12)$$

Where the first term dependent on ${CO_2}^{0.5}$ represents abiotic weathering (following GEOCARB) and the second term represents biotic weathering, which is assumed to scale directly with vegetation biomass (*V*). We retain the original model assumption of $k_{15}$ = 0.15 (i.e. a roughly 7-fold acceleration of weathering by plants) as a baseline. As options later we explore the use of $k_{15}$ = 0.25 (4-fold amplification of weathering by plants) as in GEOCARB III, and $k_{15}$ = 0.1 (10-fold amplification). We also consider the possibility that weathering is controlled by vegetation NPP rather than biomass (using $V_{npp}$ in place of *V* in the above), which removes any effect of fires on weathering.

### 2.3.8. Temperature effects on weathering

The effects of temperature on weathering rates (directly and via runoff) are separate from the effect of plants. The general form for the direct kinetic effect of temperature on weathering is:

$$f_T^i = e^{k_T^i \Delta T} \quad (13)$$

The original model used an activation energy of 62 kJ $mol^{-1}$ for silicate weathering ($k_T$ = 0.09). Here following Mills et al. (2014a) we use activation energies of 50 kJ $mol^{-1}$ for 'granite' ($k_T^{gran}$ = 0.0724) and 42 kJ $mol^{-1}$ for 'basalt' ($k_T^{bas}$ = 0.0608).

We retain the original dependencies of silicate (*f*) and carbonate (*g*) weathering on runoff:

$$f_{runoff} = [1 + 0.038\Delta T]^{0.65} \quad (14)$$

$$g_{runoff} = 1 + 0.087\Delta T \quad (15)$$

### 2.3.9. Silicate weathering

The total silicate weathering flux at present ($k_{silw}$) is divided into a volcanic rock ('basalt') fraction ($k_{basfrac}$) and a non-volcanic rock ('granite') fraction (1-$k_{basfrac}$):

$$k_{granw} = \left(1 - k_{basfrac}\right) \cdot k_{silw}, \qquad k_{basw} = k_{basfrac} \cdot k_{silw} \tag{16}$$

The equations for 'granite' (non-volcanic) weathering (*granw*) and 'basalt' (volcanic) weathering (*basw*) include additional forcing factors capturing changes in exposed areas ($a_{gran}$, $a_{bas}$) and paleogeographic effects on runoff (*PG*). In the original model all silicate weathering depended on tectonic uplift, but here whilst weathering of ancient granitic cratons is assumed to depend on uplift by default, the more rapid weathering of relative young volcanic rocks is assumed independent of uplift following Mills et al. (2014a):

$$granw = k_{granw} \cdot U \cdot PG \cdot a_{gran} \cdot f_{Tgran} \cdot f_{runoff} \cdot f_{biota} \tag{17}$$

$$basw = k_{basw} \cdot PG \cdot a_{bas} \cdot f_{Tbas} \cdot f_{runoff} \cdot f_{biota} \tag{18}$$

$$silw = granw + basw \tag{19}$$

Of course mantle plumes themselves may generate some uplift and volcanic islands are often steep and rapidly eroding terrains, but these effects are distinct from uplift of continental crust driven by plate collisions and are assumed to be enfolded in $k_{basfrac}$, which captures the disproportionate contribution of the relatively small area of volcanic rocks to the total silicate weathering flux. As an option we consider introducing an uplift dependence of basalt weathering, to help recover the original model structure. Supply limitation of silicate weathering is not considered here for the Phanerozoic, although it may have been an important factor in the aftermath of Neoproterozoic glaciations (Mills et al., 2011).

### 2.3.10. Carbonate weathering

Carbonate weathering now includes additional dependencies on crustal carbonate reservoir size and paleogeographic forcing (*PG*):

$$carbw = k_{14} \cdot \boldsymbol{C} \cdot U \cdot PG \cdot g_{runoff} \cdot f_{biota} \quad (20)$$

The dependence on the crustal carbonate reservoir size has minimal effect on the results, because it varies very little, but we include it for consistency with the other weathering fluxes.

### 2.3.11. Gypsum weathering

Gypsum weathering was originally assumed proportional to carbonate weathering and to the normalised size of the gypsum sedimentary reservoir (***gyp***). Here we make the functional dependencies explicit:

$$gypw = k_{22} \cdot \boldsymbol{gyp} \cdot U \cdot PG \cdot g_{runoff} \cdot f_{biota} \quad (21)$$

### 2.3.12. Oxidative weathering (kerogen)

Despite critique (Berner, 2006a), the revised baseline model retains the assumption that oxidative weathering of organic carbon (kerogen) has some sensitivity to variations in atmospheric $O_2$ at the present high $O_2$ concentrations. This is defended based on abundant evidence for incomplete oxidation of ancient organic carbon in rapidly uplifting/eroding terrains (Galy et al., 2015). Furthermore, the results of more detailed modelling of oxidative weathering across the observed range of erosion rates (Daines et al., 2017) show a dependence on $O_2$ that is reasonably approximated by the original square root dependence used in COPSE:

$$oxidw = k_{17} \cdot U \cdot \boldsymbol{g} \cdot \boldsymbol{o}^{0.5} \quad (22)$$

Later we test the effects of removing the $O_2$ dependence following Berner (2006a).

### 2.3.13. Pyrite weathering

Pyrite oxidation has much faster kinetics than kerogen oxidation hence it goes to completion at present high $O_2$ concentrations. Indeed detrital pyrite preservation essentially stopped after the Great Oxidation Event at ~2.4 Ga (Johnson et al., 2014). Hence we agree with the critique of (Berner, 2006a) and remove any dependence on $O_2$ in the revised model:

$$pyrw = k_{21} \cdot U \cdot \boldsymbol{pyr} \quad (23)$$

### 2.3.14. Phosphorus weathering

The revised model allows the apportioning of the phosphorus weathering flux between different rock types ($k_{Psilw}$, $k_{Pcarbw}$, $k_{Poxidw}$) to be varied and introduces an additional forcing factor ($F$) representing selective P weathering by plants:

$$phosw = k_{10} \cdot F \cdot (k_{Psilw} \cdot silw/k_{silw} + k_{Pcarbw} \cdot carbw/k_{14} + k_{Poxidw} \cdot oxidw/k_{17}) \quad (24)$$

The phosphorus weathering flux from silicates is therefore subdivided into contributions from 'granite' (non-volcanic) and 'basalt' (volcanic) rocks, following equations (17)-(19). We considered making apatite dissolution activation energy distinct from the host rock, but found it did not greatly alter the results. We also considered whether the P content relative to bulk cations (Ca + Mg, associated with the alkalinity flux) should differ between volcanic and non-volcanic silicate rocks, but decided against this as this ratio is highly variable within these rock categories, and because no such adjustment is broadly consistent with a detailed breakdown of phosphorus weathering (Hartmann et al., 2014).

### 2.3.15. Phosphorus distribution and terrestrial organic matter burial

The fraction of the weathered phosphorus flux that is ultimately buried with land plant derived organic matter (either on land or in the ocean) retains its original linear dependence on terrestrial vegetation biomass ($V$). The burial flux of terrestrially-derived organic phosphorus and associated carbon is taken to encompass both burial on land in peatlands (resulting in e.g. coal deposits) and

595 burial after erosion and transport in aquatic settings, including freshwaters, estuaries, coastal deltas,
596 and marine sediments (Burdige, 2005; Regnier et al., 2013). Here we distinguish these two burial
597 pathways and explore as options: (i) forcing the fraction of terrestrially-derived organic matter that
598 is buried in peatlands by the changing area of coal basin depositional settings ($b_{coal}$); (ii) a
599 dependence of aquatic burial of terrestrially-derived material on uplift ($U$), to capture the
600 observation that increased erosion transfers more terrestrially-derived organic matter to the ocean,
601 where in general it is more efficiently preserved than on land (Blair and Aller, 2012). These
602 alternations are captured by altering the burial flux of P with land plant matter (*pland*) in order to
603 maintain conservation of phosphorus:

604 $$pland = k_{11} \cdot V \cdot phosw \cdot \left(k_{aq} \cdot f_P(U) + \left(1 - k_{aq}\right) \cdot b_{coal}\right) \quad (25)$$

605 We set $f_P(U) = 1$ but allow $b_{coal}$ to vary as the default (Table 4). Here $k_{aq}$ is the fraction of terrestrial
606 organic matter burial occurring in aquatic settings today, which we estimate at $k_{aq} = 0.8$ (and is
607 potentially higher than this) (Burdige, 2005), consistent with only a small component of burial due to
608 coals at present. The original function for *pland* is recovered by setting $k_{aq} = 1$ and $f_P(U) = 1$.

609 The corresponding burial of terrestrially-derived organic carbon also depends on its C/P burial ratio,
610 which is a normalised forcing factor ($CP_{land}$) as in the original model:

611 $$locb = \left(\frac{C}{P}\right)_{land} \cdot pland = k_5 \cdot CP_{land} \cdot pland' \quad (26)$$

612 The transfer of the remaining available reactive phosphorus to the ocean where it can fuel marine
613 productivity is simply given by:

614 $$psea = phosw - pland \quad (27)$$

615 ### 2.3.16. Marine new production

616 New production is controlled by the proximate limiting nutrient as before:

$$newp = r_{C:P} \cdot min\left(30.9 \cdot \frac{\boldsymbol{n}}{r_{N:P}}, 2.2 \cdot \boldsymbol{p}\right) = newp0 \cdot newp' \quad (28)$$

Where the values 30.9 and 2.2 are the present average concentrations of nitrate and phosphate in the ocean (in μmol $kg^{-1}$), $r_{C:P}$=117 and $r_{N:P}$=16 are the Redfield ratios, and therefore N is proximately limiting at present giving $newp_0$ = 225.96 as a normalising constant.

### 2.3.17. Anoxia

COPSE followed earlier work (Lenton and Watson, 2000a; Van Cappellen and Ingall, 1994; Van Cappellen and Ingall, 1996) in assigning an anoxic fraction of the ocean (*anox*) that depended on the ratio of oxygen supply and demand, with a present value of 0.14 (broadly intended to represent the fractional surface area of ocean below which there is anoxia at some depth). Anoxic fraction decreased linearly with oxygen from 1 at $O_2$ = 0 to 0 at $O_2$ = 1.16 PAL (for present nutrients), and increased in a saturating way with new production (for present $O_2$) from 0 at *newp'* = 0.86 toward 1. On reflection this is a poor quantitative representation of ocean anoxia, and given growing interest in past intervals of ocean anoxia and their relationship to $O_2$ and nutrient levels, we redefine the anoxia function here. First we note that only 0.2-0.3% of the seafloor is overlain by anoxic bottom waters (Helly and Levin, 2004). Given the importance of anoxic bottom waters for P cycling (and also several redox sensitive trace metals) we redefine *anox* as the anoxic fraction of the seafloor, and assume that this scales with the volume of anoxic waters.

Oxygen levels in deeper waters separated from the ocean surface by e.g. thermal stratification are controlled by the balance of oxygen supply – via transport of surface waters equilibrated with the atmosphere – and oxygen demand – governed by upwelling transport of deep ocean limiting nutrient concentration and its uptake efficiency, creating a sinking flux of organic matter. COPSE does not consider changes in ocean transport hence the oxygenation state of the deeper ocean depends on the balance of atmospheric oxygen and deep ocean nutrient concentrations. However, some adjustment is required for the incomplete utilisation of nutrients in the high-latitude upwelling regions which play a key role in governing the deep ocean oxygenation state today. Based on the

results of multi-box models (Canfield, 1998), 1-D box-diffusion models (Ozaki and Tajika, 2013; Ozaki et al., 2011), and 3-D ocean models (Lenton and Daines, 2017; Monteiro et al., 2012) we define the control variable for deep ocean anoxia as:

$$k_u \cdot newp' - \boldsymbol{o} \quad (29)$$

Where $k_u < 1$ captures the (in)efficiency of nutrient uptake in the (high-latitude) surface waters ventilating the deep ocean, and also (implicitly) the Redfield ratio of remineralisation -$O_2$:C~170:117. In today's ocean $k_u$~0.5, given the values discussed by Canfield (1998), implying a considerable global excess of oxygen supply over demand, and further implying that a halving of atmospheric $O_2$ or a doubling of ocean nutrients would put the deep ocean on the edge of anoxia. This agrees reasonably with 3D model results where a ratio of normalised $O_2$:limiting nutrient ~0.4 (rather than 0.5) makes half of the ocean volume anoxic (Lenton and Daines, 2017), or under Cretaceous boundary conditions an approximate doubling of limiting nutrient tips anoxia (Monteiro et al., 2012). Similarly 1-D box-diffusion model results suggest a halving of $O_2$ tips anoxia (Ozaki and Tajika, 2013) (their figure 5 with fixed nutrient). Clearly some waters are anoxic today and some will remain oxygenated even when the deep ocean is tipped anoxic. To account for such spatial redox heterogeneity we use a logistic functional form:

$$anox = \frac{1}{1+e^{-k_{anox}(k_u \cdot newp' - \boldsymbol{o})}} \quad (30)$$

where $k_{anox}$ controls the sharpness of the transition between oxia and anoxia and (together with $k_u$) sets the extent of anoxia at present. For $k_u$ = 0.5, $k_{anox}$ = 12 gives *anox* = 0.0025 today, consistent with 0.2-0.3% of the seafloor being overlain by anoxic bottom waters (Helly and Levin, 2004) and giving a fairly sharp transition of *anox* from 0.23 to 0.77 as $\boldsymbol{o}$ (normalised $O_2$) drops from 0.6 to 0.4 PAL (for fixed nutrient), consistent with other models (Lenton and Daines, 2017; Ozaki and Tajika, 2013). The oxic fraction of the ocean $k_1$ = 0.997527 is redefined accordingly.

### 2.3.18. Nitrogen cycling

The redefining of anoxia and the oxic fraction of the ocean means there is huge potential for water-column denitrification to increase as anoxia increases. To prevent denitrification completely draining the ocean of nitrate we introduce a default dependence on nitrate concentration (which was anyway used as an optional 'crash preventer' in the original code at low $\boldsymbol{n} \leq 0.1$):

$$denit = k_4 \left(1 + \frac{anox}{1-k_1}\right) \cdot \boldsymbol{n} \quad (31)$$

Here half of the initial denitrification is assumed to occur under anoxic conditions at depth in sediments and therefore be insensitive to water column and sediment surface redox state.

The function for nitrogen fixation (with $r_{N:P}$=16) is unaltered:

$$nfix = k_3 \left(\frac{\boldsymbol{P} - \boldsymbol{N}/r_{N:P}}{P_0 - N_0/r_{N:P}}\right)^2 \text{ for } \frac{\boldsymbol{N}}{r_{N:P}} < \boldsymbol{P}, \text{ else } 0 \quad (32)$$

where $P_0$ and $N_0$ are the present day reservoir sizes (Table 1).

Marine organic nitrogen burial is a small term dependent on marine organic carbon burial and a fixed C:N burial ratio = 37.5:

$$monb = mocb/CN_{sea} \quad (33)$$

### 2.3.19. Marine organic carbon burial

To address a previous critique (Berner, 2006a) we include the option to have erosional (uplift) control of marine organic carbon burial, and we also include an optional dependence on $O_2$:

$$mocb = k_2 \cdot f(U) \cdot (newp')^2 \cdot f(O_2) \quad (34)$$

We set $f(U)$=1, $f(O_2)$=1 as the default (as in the original model). For the optional oxygen dependence we follow Betts and Holland (1991) as explored by Lenton and Watson (2000b):

$$f(O_2) = 2.1276 \cdot e^{-0.755 \cdot \boldsymbol{o}} \quad (35)$$

686 although we recognise that seafloor [$O_2$] can be decoupled from the atmosphere.

687 ### 2.3.20. Phosphorus burial

688 Organic phosphorus burial is calculated from marine organic carbon burial and the $(C/P)_{organic}$ burial
689 ratio ($CP_{sea}$):

690 $$mopb = mocb/CP_{sea} \quad (36)$$

691 We retain a fixed burial ratio ($CP_{sea}$ = 250) as the default (as in the original model). However, we also
692 explore the option to make this burial ratio dependent on anoxia, following Van Cappellen and Ingall
693 (1994, 1996):

694 $$CP_{sea} = \frac{k_{oxic} \cdot k_{anoxic}}{(1-anox) \cdot k_{anoxic} + anox \cdot k_{oxic}} \quad (37)$$

695 Given the update to the *anox* function we adopt $k_{oxic}$ = 250 and $k_{anoxic}$ = 4000, as originally suggested
696 (Van Cappellen and Ingall, 1994; Van Cappellen and Ingall, 1996), although subsequent work has
697 used as an upper limit $k_{anoxic}$ ~1000 (Slomp and Van Cappellen, 2007).

698 Iron-sorbed phosphorus (Fe-P) burial retains an inverse dependence on anoxia by default. The
699 redefining of anoxia means there is little scope for Fe-P burial to increase above the present level.
700 We introduce a dependence on phosphate concentration (which was also used as an optional 'crash
701 preventer' in the original code at low $\boldsymbol{p} \leq 0.1$):

702 $$fepb = \frac{k_6}{k_1} \cdot (1 - anox) \cdot \boldsymbol{p} \quad (38)$$

703 Predominantly authigenic calcium-bound phosphorus (Ca-P) burial retains a dependence on the
704 supply of organic carbon to the sediments and we also include an optional dependence on anoxia:

705 $$capb = k_7 \cdot newp'^2 \cdot f(anox) \quad (39)$$

706 We set *f*(*anox*)=1 as the default (Table 4). For the option to have seafloor anoxia suppress the
707 retention of Ca-P in sediments we follow (Slomp and Van Cappellen, 2007):

$$f(anox) = 0.5 + 0.5\frac{(1-anox)}{k_1} \quad (40)$$

### 2.3.21. Pyrite burial

Pyrite burial is taken to depend on sulphate concentration and inversely on oxygen concentration. Its dependence on marine organic carbon burial means that it includes an optional dependence on erosion (uplift) as suggested by (Berner, 2006a):

$$mpsb = k_{mpsb} \cdot \frac{\boldsymbol{s}}{\boldsymbol{o}} \cdot mocb' \quad (41)$$

We considered an anoxia rather than $O_2$ dependence, which would amount to considering anoxic water-column precipitation and preservation of pyrite, but we reason that sedimentary formation of pyrite has been the dominant mechanism over the Phanerozoic.

### 2.3.22. Gypsum burial

Gypsum burial was originally dependent on ocean sulphate concentration and variable calcium concentration. The calcium variable is replaced here with a forcing factor ($c_{cal}$):

$$mgsb = k_{mgsb} \cdot \boldsymbol{s} \cdot c_{cal} \quad (42)$$

### 2.3.23. Carbonate burial

Oceanic carbonate is assumed to be in steady state with marine carbonate carbon burial balancing carbonate input from silicate and carbonate weathering (as in the original model):

$$mccb = silw + carbw \quad (43)$$

We also experimented with a more complex formulation where marine carbonate burial is assumed to maintain an alkalinity balance of the ocean that is affected by the sulphur cycle (Mills et al., 2014a; Torres et al., 2014), with pyrite burial a source of alkalinity, and pyrite weathering, pyrite degassing and gypsum degassing all sinks of alkalinity (sources of sulphuric acid). To maintain a present day steady state this requires upward adjustment of the silicate weathering flux constant

($k_{silw}$) such that it balances total volcanic acid input, i.e. both sulphur and carbon degassing. With that adjustment, the effect on the results is small, so for simplicity we leave it out.

### 2.3.24. Carbon and sulphur isotope systems

COPSE tracks the isotopic composition of all the carbon and sulphur reservoirs. The functional dependencies of carbon and sulphur isotope fractionation are kept the same as in the original model (Bergman et al., 2004). This includes temperature-dependent atmosphere-ocean fractionation of carbon, temperature-dependent fractionation of marine carbonate deposition (assuming calcite throughout), marine organic carbon fractionation (relative to carbonate) dependent on $CO_2$ and $O_2$, land organic carbon fractionation (relative to atmosphere) dependent on $O_2$, and a fixed sulphur fractionation of pyrite burial relative to gypsum burial – as an $O_2$-dependence was previously found to considerably degrade the $\delta^{34}S$ predictions (Bergman et al., 2004).

### 2.3.25. Strontium tracer cycle

A strontium cycle and its isotopes are implemented following Francois and Walker (1992) and Vollstaedt et al. (2014) with some improvements to the formulation described in Mills et al. (2014a). A full description is given in Appendix A. Ocean and sedimentary (carbonate) reservoirs of strontium are considered. Ocean Sr sources are the weathering of old igneous rocks (granites), new igneous rocks (basalts), sedimentary carbonates, and mantle input. Ocean Sr sinks are the incorporation of strontium in (carbonate) sediments and seafloor weathering. The sedimentary Sr pool has input from carbonate burial, and outputs from carbonate weathering and metamorphism. The $^{87}Sr/^{86}Sr$ values of mantle input and continental silicates have prescribed present day values (mantle 0.703, 'basalts' 0.705, 'granites' 0.715) but are assumed to have increased over time due to Rb decay. The $^{87}Sr/^{86}Sr$ of sedimentary carbonates varies depending on inputs/outputs and is initialised at 0.708 (a reasonable value for the Late Neoproterozoic). The overall approach is not expected to precisely reproduce the ocean $^{87}Sr/^{86}Sr$ record, because of heterogeneity in the ages of rocks being weathered, but it may be possible to capture large-scale features of the record.

## 2.4. Baseline fluxes

The C, O, P, S and N cycles are assumed to have been in approximate steady-state in pre-industrial time (referred to as the 'present') at least for the purpose of assigning a set of balanced baseline fluxes in the model. The slow variables in the model do not necessarily reach this steady state at present. The original model baseline fluxes are listed in Table 2, along with the changes made by Mills et al. (2014a), and some alternative proposals discussed here and tested in the Results section.

### 2.4.1. Sulphur cycle

The original COPSE and the updated version of Mills et al. (2014a) have no pyrite or gypsum degassing, pyrite weathering/burial of $0.53 \times 10^{12}$ molS $yr^{-1}$ and gypsum weathering/burial of $1.0 \times 10^{12}$ molS $yr^{-1}$. We retain these fluxes initially and refer to them as 'low S' fluxes. Then in exploring a new set of baseline fluxes we introduce pyrite degassing ($0.25 \times 10^{12}$ molS $yr^{-1}$) and gypsum degassing ($0.5 \times 10^{12}$ molS $yr^{-1}$) and adjust pyrite weathering to $0.45 \times 10^{12}$ molS $yr^{-1}$ and gypsum weathering to $2.0 \times 10^{12}$ molS $yr^{-1}$, to give the GEOCARBSULF set of fluxes (Royer et al., 2014), which we refer to as 'high S' fluxes. Burial of pyrite or gypsum is assumed to match the total of degassing and weathering in this case. Recent constraints on the pyrite burial fraction of total sulphur burial suggest it is 20-35% today (Tostevin et al., 2014), and our low and high sets of S fluxes sit at the upper and lower ends of this range respectively. Other work reconstructing sulphate evaporite burial fluxes on Laurentia has argued for a much larger pyrite burial fraction and associated pyrite oxidative weathering over much of Phanerozoic time (Halevy et al., 2012). However, this is at odds with sulphur isotope constraints, which suggest that pyrite burial only dominated in the early Paleozoic (Canfield, 2013).

### 2.4.2. Inorganic carbon cycle

Seafloor weathering was previously included at $1.75 \times 10^{12}$ molC $yr^{-1}$ (Mills et al., 2014a; Mills et al., 2014b) based on the midpoint of Cenozoic-Cretaceous estimates ~$0.5\text{-}3 \times 10^{12}$ molC $yr^{-1}$ from deep sea drilling cores and estimated crust production rates. However, depending on assumptions about

780 the incorporation of sedimentary carbonates, seafloor weathering might range up to 4.1-5.7x$10^{12}$
781 molC $yr^{-1}$ (Alt and Teagle, 1999; Gillis and Coogan, 2011; Staudigel et al., 1989). Seafloor weathering
782 was previously assumed (Mills et al., 2014a) to imply a reduction in terrestrial silicate weathering to
783 4.9x$10^{12}$ molC $yr^{-1}$ (from a baseline carbonate degassing of 6.65x$10^{12}$ molC $yr^{-1}$ from GEOCARB).
784 However, the silicate weathering flux was already low compared to recent estimates, whereas the
785 carbonate weathering flux (13.35x$10^{12}$ molC $yr^{-1}$ from GEOCARB) is high. The estimated total global
786 $CO_2$ consumption flux by carbonate plus silicate weathering is ~20x$10^{12}$ molC $yr^{-1}$ (Amiotte-Suchet et
787 al., 2003; Gaillardet et al., 1999; Hartmann et al., 2009; Munhoven, 2002) in good agreement with
788 COPSE, but the apportioning is very different with ~60% silicate weathering (~12x$10^{12}$ molC $yr^{-1}$) and
789 ~40% carbonate weathering (~8x$10^{12}$ molC $yr^{-1}$) (Hartmann et al., 2009). Furthermore, the
790 contribution of volcanic rocks to silicate weathering is estimated to be ~17-25% (i.e. 2-3x$10^{12}$ molC
791 $yr^{-1}$) (Hartmann et al., 2009), significantly less than the ~30-35% or ~4.1x$10^{12}$ molC $yr^{-1}$ estimated
792 previously (Dessert et al., 2003), with 35% (of 4.9x$10^{12}$ molC $yr^{-1}$, i.e. 1.715x$10^{12}$ molC $yr^{-1}$) having
793 been used in the interim version of COPSE (Mills et al., 2014a). The implication that non-volcanic
794 rocks contribute ~9-10x$10^{12}$ molC $yr^{-1}$ to silicate weathering is at the upper end of another recent
795 estimate carefully accounting for uncertainties ~7.85 (5.78-9.93)x$10^{12}$ molC $yr^{-1}$ (Moon et al., 2014).

796 Given these considerations we view the inorganic carbon cycle fluxes used by Mills et al. (2014a) as a
797 'low' set of estimates. As a new set of 'high' inorganic C cycle fluxes we take 9x$10^{12}$ molC $yr^{-1}$ for non-
798 volcanic weathering, 3x$10^{12}$ molC $yr^{-1}$ for volcanic weathering (i.e. 25% of silicate weathering; $k_{basfrac}$
799 = 0.25), 8x$10^{12}$ molC $yr^{-1}$ for carbonate weathering, and 3x$10^{12}$ molC $yr^{-1}$ for seafloor weathering,
800 which we add to silicate weathering to give a total carbonate degassing 15x$10^{12}$ molC $yr^{-1}$ (more than
801 a doubling of carbonate degassing relative to the original model).

802 ### 2.4.3. Organic carbon cycle

803 The total organic carbon burial flux in the original COPSE of 9x$10^{12}$ molC $yr^{-1}$, comprising marine-
804 derived 4.5x$10^{12}$ molC $yr^{-1}$ and terrestrially-derived 4.5x$10^{12}$ molC $yr^{-1}$ components, is considerably

larger than in GEOCARB (~$5x10^{12}$ molC $yr^{-1}$) and in an earlier model based on organic carbon content of sediments (~$5x10^{12}$ molC $yr^{-1}$) (Berner and Canfield, 1989). However, it is comparable to other models (Slomp and Van Cappellen, 2007) and less than some estimates ≥$1x10^{13}$ molC $yr^{-1}$ (Hedges and Keil, 1995; Holland, 1978). Total organic carbon burial is counterbalanced by oxidative weathering of organic carbon ($7.75x10^{12}$ molC $yr^{-1}$) and organic carbon degassing ($1.25x10^{12}$ molC $yr^{-1}$). A potential problem with high estimates of organic carbon burial is that the corresponding oxidative weathering flux is right at the upper limit ($7.78x10^{12}$ molC $yr^{-1}$) of estimates for the supply of organic carbon to weathering environments based on erosional rock flux and 0.4-0.6 wt% content of sediments (Daines et al., 2017), allowing no scope for incomplete oxidative weathering (which is widely recognised to occur and is assumed in COPSE). The discrepancy might be explained by a larger metamorphic flux of organic carbon degassing and/or by relatively rapid recycling of sedimentary organic carbon as thermogenic methane (Daines et al., 2017).

Terrestrial organic carbon burial is large in COPSE, but within the range of estimates for the terrestrial contribution to organic carbon burial in marine (mostly deltaic) settings today of ~$3.8±1.1x10^{12}$ molC $yr^{-1}$, which we base on ~80% (Galy et al., 2015) of ~$4.8±1.4 x10^{12}$ molC $yr^{-1}$ (Burdige, 2005) being recent plant matter (the remaining ~20% being recycled ancient organic matter, i.e. kerogen). With the revision to the pyrite burial flux suggested above, the C/S ratio by mass of marine shales would be ~2.4 (assuming no terrestrial matter contributing), which is in the range of Cenozoic-Quaternary values (Raiswell and Berner 1986), but this would be higher assuming a (low S) terrestrial contribution to marine shales.

Given these considerations we view the original organic carbon burial and oxidative weathering fluxes in COPSE as a 'high' set of estimates. As an alternative 'low' set of fluxes we follow Daines et al. (2017) and consider $5x10^{12}$ molC $yr^{-1}$ total organic carbon burial, split $2.5x10^{12}$ molC $yr^{-1}$ marine and $2.5x10^{12}$ molC $yr^{-1}$ terrestrially-derived, retaining $1.25x10^{12}$ molC $yr^{-1}$ organic carbon degassing and therefore $3.75x10^{12}$ molC $yr^{-1}$ oxidative weathering.

(Note that when the marine and/or terrestrially-derived organic carbon burial fluxes are adjusted the corresponding baseline marine organic phosphorus burial and/or phosphorus burial with terrestrial matter, and phosphorus weathering fluxes are adjusted to retain steady state. Also the baseline nitrogen fixation flux is adjusted to counterbalance any change in organic nitrogen burial.)

### 2.4.4. Phosphorus cycle

The total phosphorus weathering flux in the original COPSE of $43.5 \times 10^9$ molP $yr^{-1}$ (of which $39 \times 10^9$ molP $yr^{-1}$ went in reactive form to the ocean and $4.5 \times 10^9$ molP $yr^{-1}$ was buried with terrestrial matter) is in the range of estimates for reactive P flux to the ocean of $23\text{-}155 \times 10^9$ molP $yr^{-1}$ (Compton et al., 2000) and in good agreement with a recent estimate of P weathering of $37 \times 10^9$ molP $yr^{-1}$ ($1144 \times 10^9$ gP $yr^{-1}$) (Hartmann et al., 2014). That estimate may be low given it assumes stoichiometric release of P with $SiO_2$ and cations, whereas there is evidence for preferential release of P by biotic weathering (Lenton et al., 2012; Quirk et al., 2015).

The apportioning of the phosphorus weathering flux in the original model of $k_{Psilw}$ = 2/12, $k_{Pcarbw}$ = 5/12, $k_{Poxidw}$ = 5/12 was based on an association with the relative size of Fe-P, Ca-P and Org-P burial fluxes. On reflection, this overestimates the contributions of carbonate and especially oxidative weathering and underestimates the contribution of silicate weathering, which inputs P from the mantle (via volcanic rocks) and from the crust (via non-volcanic silicates). Recent detailed estimates suggest P weathering input comes 29% from volcanic rocks, 16% from plutonic and metamorphic rocks, 14% from carbonates, and 41% from non-carbonate sediments (which also contribute ~50% to total silicate weathering) (Hartmann et al., 2014). An upper limit on the contribution of oxidative weathering to reactive P flux to the ocean based on shale stoichiometry and complete P release is ~8-13% (Compton et al., 2000), however analysis of weathered shale sequences suggests sedimentary organic P is more resistant to release than organic C (Kolowith and Berner, 2002), meaning this percentage should be lower. Given these considerations we suggest $k_{Psilw}$ = 0.8, $k_{Pcarbw}$ = 0.14, $k_{Poxidw}$ = 0.06 as an improved apportioning. Applying $k_{basfrac}$ = 0.35 or 0.25 then gives a volcanic

855 weathering contribution of 28% or 20% to the P weathering flux, in reasonable agreement with the
856 29% inferred by (Hartmann et al., 2014).

857 The phosphorus burial fluxes in original COPSE of $18x10^9$ molP $yr^{-1}$ as organic P (Org-P), $6x10^9$ molP
858 $yr^{-1}$ as Fe-adsorbed P (Fe-P), and $15x10^9$ molP $yr^{-1}$ as calcium-bound P (Ca-P) (i.e. a 46%:15%:39%
859 split of $39x10^9$ molP $yr^{-1}$), are relatively low compared to more recent estimates and models (Slomp
860 and Van Cappellen, 2007), and the apportioning of P between sinks is questionable. More recent
861 modelling suggests Org-P $20x10^9$ molP $yr^{-1}$, Fe-P $20x10^9$ molP $yr^{-1}$, and Ca-P $40x10^9$ molP $yr^{-1}$, i.e. a
862 25%:25%:50% split of $80x10^9$ molP $yr^{-1}$ (Slomp and Van Cappellen, 2007). However, this represents a
863 considerable increase in P weathering flux relative to current estimates (Hartmann et al., 2014). A
864 smaller fraction of total P burial in organic form can help reconcile a larger total P burial flux with
865 measured $(C:P)_{org}$ burial ratios ~200-250, which for Org-P ~$20x10^9$ molP $yr^{-1}$ imply marine organic C
866 burial ~$4\text{-}5x10^{12}$ molC $yr^{-1}$. However, a marine organic C burial flux of ~$2.5x10^{12}$ molC $yr^{-1}$ (noting the
867 discussion above) is hard to reconcile with an organic P burial flux of ~$20x10^9$ molP $yr^{-1}$ as this implies
868 a burial ratio $(C:P)_{org}$ of ~125 close to the Redfield ratio. Given these considerations we view the
869 original P burial fluxes in COPSE as a plausible set of estimates. As an alternative apportioning of P
870 burial fluxes we consider: Org-P $10x10^9$ molP $yr^{-1}$ (for Org-C $2.5x10^{12}$ molC $yr^{-1}$), Fe-P $10x10^9$ molP $yr^{-1}$, and Ca-P $20x10^9$ molP $yr^{-1}$, with a corresponding adjustment of the P weathering flux.

## 872 2.5. Model implementation, initialisation and integration

873 The model is now coded in Matlab and the 'stiff' system of coupled ODEs is efficiently computed
874 using a variable order ODE solver (Shampine and Reichelt, 1997). The model is initialised with the
875 reservoir sizes in Table 1 but spun up from 1000 Ma to 550 Ma to give the sedimentary reservoir
876 sizes time to adjust to the initial boundary conditions, in particular the differing Earth surface redox
877 balance prior to plants. In the original study only a 50 Myr spin-up was used, meaning that the
878 sedimentary (and to some degree sulphate) reservoirs were still adjusting during the early Paleozoic.
879 For the original model configuration, by 550 Ma, the longer spin-up leads to a ~$0.9x10^{20}$ mol S or

880 ~1.8x10$^{20}$ mol $O_2$ eq. (~50%) increase in the pyrite reservoir (***PYR***), and a ~2x10$^{20}$ mol C (~16%)
881 decrease in the organic carbon reservoir (***G***), with a ~0.5x10$^{20}$ mol S (~25%) or ~1x10$^{20}$ mol $O_2$ eq.
882 decrease in the gypsum (***GYP***) reservoir and ~1.6x10$^{20}$ mol C (~3%) growth in the carbonate carbon
883 reservoir (***C***). Thus the pyrite reservoir is predicted to have been roughly twice the size of the
884 gypsum reservoir at the onset of the Phanerozoic, which seems reasonable given predominantly
885 anoxic Precambrian oceans dominated by pyrite deposition, but some intervals of gypsum
886 deposition in the Paleoproterozoic and Neoproterozoic (Lenton and Daines, 2017).

## 887 2.6. Comparison to data

888 We compare the predictions of the various model versions to six proxy data compilation targets for:
889 $CO_2$, $O_2$, $SO_4$, $\delta^{13}C$, $\delta^{34}S$, and $^{87}Sr/^{86}Sr$, summarised in Table 6. The $CO_2$ proxy compilation (Royer,
890 2014) is derived from at least six different sources and although disagreement amongst the different
891 methods has been reduced in recent studies, there are still some notable discrepancies, only
892 partially captured by the +/- 1 s.d. uncertainty range used here. There is also a lack of proxy data
893 prior to 420 Ma. The atmospheric $O_2$ mixing ratio reconstruction is based on the charcoal content of
894 coals (Glasspool and Scott, 2010) scaled by the assumption of a lower limit on $O_2$ consistent with
895 combustion of 15% and an uncertain upper limit consistent with continuous forests of 25-35%. Here
896 we extend the 15% lower limit back to 420 Ma based on the presence of earlier charcoal reviewed in
897 Lenton et al. (2016). Other studies would put the lower limit for self-sustaining combustion a little
898 higher at 16-17% (Belcher and McElwain, 2008). More fundamentally, the underlying assumption of
899 the method that more oxygen leads to more charcoal can be questioned, because charcoal is the
900 product of pyrolysis, hence more oxygen fuelling combustion could conceivably reduce charcoal
901 production. The other proxy data targets are more established. For $SO_4$ we consider only fluid
902 inclusion data (avoiding reconstructions based on sulphur isotopes). The carbonate $\delta^{13}C$ compilation
903 spans different organisms and depths which may generate some shifts in the record that do not
904 reflect a truly global signature (Saltzman and Thomas, 2012). For $\delta^{34}S$ we only consider carbonate

associated sulphate (CAS). The $^{87}Sr/^{86}Sr$ record is from conodont apatite, extending LOWESS V5 (McArthur et al., 2012) prior to 503 Ma with data from Cox et al. (2016).

# 3. Results and Discussion

The above considerations represent a potentially bewildering set of multiple changes to the COPSE model. To clarify the effects of different changes we consider a series of cumulative changes to the model. First we revisit the original model predictions in the light of new proxy compilations. Then we look at the effect of updating the original forcing factors with the original model structure. Then we consider the effects of changing the structure and some key functions of the model (that we consider to be clear mechanistic improvements). Next we examine the effects of changing the baseline fluxes. Then we explore the effect of optional additional forcing factors. From this we arrive at an improved model with which we test some further mechanistic hypotheses for changes in the model functions.

## 3.1. Original model results in the light of new proxy compilations

First we revisit the original model predictions (black dashed line in Fig. 5) in the light of updated proxy records. Proxies for $pCO_2$ have generally been adjusted downwards since the original COPSE study hence the original model predictions of $pCO_2$ now appear too high for much of the mid-late Paleozoic (420-300 Ma), they are generally in the range of proxy uncertainty in the Mesozoic-Cenozoic, but miss a Triassic peak around 240-200 Ma. The original model predictions of $O_2$ are too low in the mid-Paleozoic (420-330 Ma), given the charcoal record at this time, reasonable from then until 60 Ma, but too high for the rest of the Cenozoic (50-0 Ma including at present). The original model predictions of $SO_4$ are reasonable for the Paleozoic but miss the Mesozoic-Cenozoic dip, because the interactive partial calcium cycle misses a Mesozoic-Cenozoic [Ca] peak. Predicted $\delta^{13}C$ captures the early Paleozoic mean ~0 ‰ (although none of its extreme variability), but it misses the persistent rise to ~+2 ‰ that occurs in the Late Ordovician, and the (imposed) peak ~350-280 Ma

929 does not match the observed structure well, although from ~200 Ma onwards the fit to the record is
930 better. Predicted $\delta^{34}S$ fits the data reasonably well, indicating that this proxy does not constrain $SO_4$
931 well. We do not expect the original model to capture $^{87}Sr/^{86}Sr$ variability, because e.g. it has no
932 distinction in the functional responses of volcanic and non-volcanic silicate rocks. It shows an overall
933 rise in $^{87}Sr/^{86}Sr$ driven by Rb decay, and captures some of the structure of variability e.g. at ~350 Ma,
934 because the original uplift forcing is derived from $^{87}Sr/^{86}Sr$ (but otherwise surprisingly little of it).
935 Major deficiencies are a failure to capture the high early Paleozoic $^{87}Sr/^{86}Sr$ and the Mesozoic low
936 followed by Cenozoic rise of $^{87}Sr/^{86}Sr$.

937 ## 3.2. Updating the original forcing factors

938 Next we consider how the predictions of the original model are affected by updates to the original
939 forcing factors (Fig. 3) with the results in Figure 5. This mirrors the approach of some of the
940 intervening studies with COPSE (Lenton et al., 2012, 2016).

941 We show the combined effects of updating the degassing (*D*) and carbonate burial (*B*) forcing (blue
942 in Fig. 5), because they both operate on degassing. The updated degassing (*D*) is responsible for
943 increased $CO_2$ and $O_2$ 250-130 Ma accompanied by slight increases in $SO_4$ and $\delta^{13}C$. The fit to $CO_2$
944 proxies 230-200 Ma and $O_2$ proxies 220-200 Ma is improved, but $CO_2$ is too high 160-140 Ma. The
945 updated carbonate burial (*B*) forcing tends to counteract the updated degassing forcing (*D*) during
946 150-0 Ma. Together they slightly lower $CO_2$ and $O_2$ during 120-90 Ma and 60-30 Ma somewhat
947 improving the fit to proxies. The updated uplift (*U*) forcing (red in Fig. 5) smooths out some of the
948 variability in model predictions and leads to higher Mesozoic-early Cenozoic $CO_2$ and $O_2$ predictions.
949 This generally improves the fit to $CO_2$ and $O_2$ proxies until ~130 Ma but degrades it ~120-50 Ma.

950 Combining the updated evolution (*E*), weathering (*W*) and $CP_{land}$ forcing (green in Fig. 5) leads to an
951 earlier drawdown of $CO_2$ and earlier rise of $O_2$, with a corresponding increase in $\delta^{13}C$ and $SO_4$ and
952 decrease in $\delta^{34}S$. The Late Ordovician drawdown of $CO_2$ to ~8.5 PAL is close to the threshold for
953 triggering Late Ordovician glaciations (Lenton et al., 2012; Pohl et al., 2014) and the fit to $CO_2$ proxies

410-370 Ma is much improved. The fit to $O_2$ proxies prior to 330 Ma is much improved, although $O_2$ ~12% in the Silurian is still too low to explain the first charcoal 420-400 Ma. The corresponding increase in $\delta^{13}C$ to ~1 ‰ is less than the observed rise to ~2 ‰, which also requires some selective enhancement of P weathering by early plants (Lenton et al., 2016), explored below. The corresponding decline in $\delta^{34}S$ is at the lower end of the data range.

Combining all the preceding forcing updates (black in Fig. 5) retains the improvement in mid Paleozoic $CO_2$ and $O_2$ predictions associated with the rise of plants. It increases predicted $CO_2$ 310-270 Ma and 250-60 Ma and predicted $O_2$ prior to 50 Ma. Increased $CO_2$ 310-270 Ma degrades the predictions, they are improved 240-200 Ma, but are too high again 180-140 Ma and 100-60 Ma. Increased $O_2$ is too high 90-60 Ma and at scattered times beforehand e.g. at 300 Ma.

In the following we take forward these updates to the *D*, *U*, *E*, *W*, *B* and $CP_{land}$ forcings. Later we return to reconsider the $CP_{land}$ forcing alongside the coal depositional area forcing, as well as adding a selective P weathering forcing (*F*).

## 3.3. Changing the baseline model structure

In developing the model we isolated which structural changes to the model have the most significant effects on $CO_2$, $O_2$ and the other predicted variables. Here we summarise the key controls.

### 3.3.1. Key controls on $CO_2$

The effect of changes to the controls on weathering, which primarily affect $CO_2$, are summarised in Figure 6 (contrast the results to the black dashed line). The inclusion of seafloor weathering (blue) makes a large contribution to drawing down $CO_2$, consistent with it varying in line with degassing (which is generally elevated above present). Making basalt weathering independent of uplift (red) also tends to significantly lower $CO_2$ when uplift is below present through most of the Phanerozoic (except the early Paleozoic). Distinguishing different activation energies for granite and basalt weathering (cyan) tends to increase $CO_2$ consistent with a lower overall activation energy and

978 therefore weaker negative feedback on $CO_2$ especially in the early-mid Paleozoic when both uplift
979 and degassing are relatively high and therefore weathering flux is high. The new vegetation
980 dependence of weathering (green) generates markedly higher $CO_2$ from the origin of plants
981 onwards, consistent with the original function overestimating plant effects when *EW*<1. The new
982 temperature function (magenta) noticeably lowers $CO_2$ in the mid-late Paleozoic and early Mesozoic.
983 Combining all these changes to the weathering response in the model (black) generally leads to
984 markedly lower $CO_2$ except ~400-350 Ma during the early rise of plants.

985 Changes to the model that alter $CO_2$ generally tend to alter $O_2$ in the same direction regardless of
986 whether they have direct effects on the redox balance, because of the link between weathering and
987 P input, and the link between $CO_2$, productivity and terrestrial organic carbon burial. The exception is
988 the new temperature function (magenta), which has minimal effect on $O_2$ and other variables
989 because it simply achieves the same weathering flux at a different $CO_2$ and temperature. Including
990 seafloor weathering (blue) has the largest individual effect on $O_2$, lowering it throughout because it
991 does not supply P whereas terrestrial weathering does (Mills et al., 2014b), and lowering it indirectly
992 because lower $CO_2$ suppresses terrestrial productivity. This makes early-mid Paleozoic $O_2$ too low but
993 fits the $O_2$ proxy better thereafter. Making basalt weathering independent of uplift (red) markedly
994 lowers $O_2$ from the late Paleozoic onwards, because lower $CO_2$ suppresses vegetation productivity,
995 and this improves the fit to the $O_2$ proxy. Distinguishing different activation energies for basalt and
996 granite weathering and thus lowering overall activation energy (cyan) increases $O_2$ when it increases
997 $CO_2$ (in the early Paleozoic and late Mesozoic-Cenozoic), degrading the fit to the $O_2$ proxy. The new
998 vegetation dependence of weathering (green) has small effects on $O_2$ despite consistently increasing
999 $CO_2$, because it has a counteracting direct effect of suppressing P weathering. Combining these
1000 changes (black) leads to markedly lower $O_2$ throughout, which is too low ~420-380 Ma.

1001 Effects on $SO_4$, $\delta^{13}C$ and $\delta^{34}S$ are modest and do not help to distinguish between mechanisms,
1002 although it is worth noting that including seafloor weathering (blue) lowers $SO_4$ throughout because

terrestrial weathering fluxes, including gypsum weathering, are reduced, and making basalt weathering independent of uplift (red) lowers $SO_4$ later in the Phanerozoic because $CO_2$ is reduced and with it gypsum weathering. Effects on $^{87}Sr/^{86}Sr$ help evaluate these two mechanistic changes. Including seafloor weathering (blue) lowers $^{87}Sr/^{86}Sr$, improving the Mesozoic-Cenozoic fit to the data but degrading the Paleozoic fit. Making basalt weathering independent of uplift (red), leads to lower $^{87}Sr/^{86}Sr$ in the late Paleozoic, Mesozoic and Cenozoic, improving the overall fit to the data. Other changes have minor effects on $^{87}Sr/^{86}Sr$. Combining the changes (black) yields a reasonable fit to the $^{87}Sr/^{86}Sr$ record from ~160 Ma onwards but $^{87}Sr/^{86}Sr$ is too low through almost all of the Paleozoic and at present, consistent with a high initial choice of 0.35 for the volcanic rock fraction of silicate weathering (Table 2), following Mills et al. (2014a).

### 3.3.2. Key controls on redox balance, $O_2$, $SO_4$

Changes that primarily affect the model redox balance, $O_2$, $SO_4$ and only secondarily impact $CO_2$ are included in Figure 7 (again contrast the results to the black dashed line). Replacing the interactive Ca cycle with a prescribed ocean [Ca] (blue) (to broadly match sparse fluid inclusion data) yields a better fit to $SO_4$ data (as would be expected) and the Mesozoic-Cenozoic dip in $SO_4$ generates a corresponding small reduction in $O_2$. The new fire dependence of vegetation (red) has the greatest effect on $O_2$ increasing it during the early rise of plants and decreasing it once $O_2$ exceeds PAL, consistent with a stronger overall negative feedback on $O_2$ than in the original model. Removing the $O_2$ dependence of pyrite weathering (cyan) slightly lowers early Paleozoic $O_2$ and slightly increases $O_2$ after 350 Ma, consistent with the removal of a (weak) negative feedback. The secondary effects of these changes on $CO_2$ are generally very small, with the exception that revising the fire dependence of vegetation (red) increases the drawdown of $CO_2$ associated with the rise of early land plants, because the effect of removing fires on vegetation biomass is assumed greater. Effects on other predicted variables are modest. The new fire dependence of vegetation amplifies the initial rise in $\delta^{13}C$ with early plants but damps down changes in $\delta^{13}C$ once $O_2$ exceeds PAL, consistent with stronger negative feedback on organic carbon burial. It also has modest effects on $SO_4$ and $\delta^{34}S$.

1029 Removing the $O_2$ dependence of pyrite weathering (cyan) modestly increases $SO_4$ and lowers $\delta^{34}S$ in
1030 the early Paleozoic.

1031 ### 3.3.3. Combined effects

1032 Combining the changes that affect the redox balance leads to similar results (not shown) to just
1033 updating the fire dependence of vegetation (red). Combining the changes affecting the redox
1034 balance with those affecting $CO_2$ (green in Fig. 7) shows that altering the weathering functions has
1035 the greatest effects. Other changes to the baseline model (Table 4) include the quadratic
1036 dependence of the atmospheric fraction of $CO_2$, the new anoxia, denitrification and Fe-P burial
1037 functions. These have minimal individual effects on our key data targets (not shown). When these
1038 additional changes are combined with all of those discussed above, we arrive at the new baseline
1039 model structure (black in Fig. 7) which can be compared to the original model structure (black
1040 dashed).

1041 Overall, the changes in model structure lead to lower predictions of $CO_2$ and $O_2$ throughout the
1042 Phanerozoic, with a similar pattern of variation (governed largely by the unchanged forcing factors).
1043 With the rise of the earliest plants, $CO_2$ drops closer to the first proxies at 420 Ma, and is in the range
1044 of the proxies 410-340 Ma, but remains too high 330-300 Ma. $CO_2$ is in the proxy range 290-240 Ma,
1045 but is at the lower end of the range or below it 230-100 Ma, when before it was generally too high.
1046 From 100-0 Ma the fit to the $CO_2$ proxies is somewhat improved. Early $O_2$ is too low, failing to rise to
1047 levels supporting combustion until ~380 Ma and not intersecting the proxy estimates until 330 Ma.
1048 Peak $O_2$ ~290 Ma is markedly reduced, but 280-240 Ma $O_2$ is too low. From 230-0 Ma the proxies are
1049 quite variable but predicted $O_2$ is broadly in the middle of the range with a much less pronounced
1050 Late Cretaceous peak, which previously was above the proxies. The Cenozoic $O_2$ decline reaches the
1051 present day value whereas previously it ended at 23% (~1.1 PAL). $SO_4$ predictions are improved by
1052 forcing with reconstructed [Ca] variations, but are a little below proxies 300-250 Ma, consistent with
1053 $O_2$ being too low at this time. $\delta^{13}C$ is lowered somewhat throughout, particularly after the rise of

land plants. $\delta^{34}S$ is relatively insensitive. The fit to the $^{87}Sr/^{86}Sr$ record is considerably improved in the Mesozoic-Cenozoic but degraded in the Paleozoic.

## 3.4. Changing the baseline fluxes

Here we apply alternative sets of model fluxes (Table 2) to the new baseline model (just described, including the updated *D*, *U*, *E*, *W*, *B* and $CP_{land}$ forcing, and shown as the black dashed line), with the results shown in Figure 8.

Introducing the 'high' set of sulphur fluxes including pyrite and gypsum degassing (blue) decreases atmospheric $CO_2$ throughout and decreases atmospheric $O_2$ from the rise of plants onwards. $SO_4$ is increased from the latest Paleozoic onwards, improving the fit to late Paleozoic data but missing low $SO_4$ in fluid inclusions at ~100 Ma. $\delta^{34}S$ is not greatly altered consistent with its insensitivity to $SO_4$. $\delta^{13}C$ is lowered in the early-mid Paleozoic and increased from ~380 Ma onwards. $^{87}Sr/^{86}Sr$ is lowered slightly throughout. The effects on $O_2$ and $CO_2$ are predominantly due to the introduction of pyrite degassing, which always tends to decrease $O_2$ (the introduction of gypsum degassing tends to increase $O_2$ in the early Paleozoic but otherwise has little effect on $CO_2$ or $O_2$).

Adopting the 'high' set of inorganic carbon fluxes (red) increases atmospheric $CO_2$ and $O_2$ throughout the Phanerozoic. Atmospheric $CO_2$ is increased because seafloor weathering now makes up a smaller fraction of total terrestrial plus seafloor silicate weathering, and $CO_2$ has to adjust more for terrestrial silicate weathering to balance the carbon cycle (recalling that changes in degassing directly cause counterbalancing changes in seafloor weathering as well as there being a temperature-mediated negative feedback on seafloor weathering). Atmospheric $O_2$ is increased because the shift from seafloor to terrestrial weathering increases P input. Effects on $SO_4$, $\delta^{13}C$ and $\delta^{34}S$ are modest. There is a striking overall increase in $^{87}Sr/^{86}Sr$ due largely to a decrease in the volcanic rock fraction of silicate weathering from 0.35 to 0.25 (Table 2), which improves the fit to the data, particularly in the Paleozoic and at present.

Adopting the 'low' set of organic carbon fluxes (green) produces lower $O_2$ throughout. $\delta^{13}C$ is generally lowered consistent with a smaller organic fraction of total carbon burial, but from ~280 Ma onwards is notably below the long-term mean of +2 ‰. The lower $O_2$ allows plants to be more productive and amplify silicate weathering more, thus lowering $CO_2$ from ~380 Ma onwards. $SO_4$ is lowered in the early-mid Paleozoic and $\delta^{34}S$ increased. $^{87}Sr/^{86}Sr$ is increased slightly throughout.

Changing the split of P weathering (cyan) leads to higher $O_2$ almost all the time except ~350-310 Ma. This reflects the majority of P weathering now being linked to silicate weathering which is generally above present due to elevated degassing. Hence the biggest increases in $O_2$ are generally when degassing is highest in the early Paleozoic and Mesozoic. $\delta^{13}C$ is correspondingly increased at these times, improving fit to the Mesozoic data. $CO_2$ is increased from ~270 Ma onwards, because the higher $O_2$ tends to suppress vegetation and its effect on silicate weathering and this arguably improves fit to the proxy data. Effects on $SO_4$ and $\delta^{34}S$ are small. Changing the apportioning of P burial fluxes has tiny effects (not shown).

Relative to the new baseline (black dashed), a combined update of the fluxes (black) comprising high S fluxes, high inorganic carbon fluxes, low organic carbon fluxes, revised split of P weathering and revised split of P burial fluxes, yields increased atmospheric $CO_2$ in the early-mid Paleozoic and particularly the Mesozoic-Cenozoic, the latter improving fit to the proxies 230-110 Ma (but degrading it 100-60 Ma). It yields an increase in early Paleozoic $O_2$, improving fit to the constraints, similar values ~350-300 Ma, and somewhat higher $O_2$ ~250-0 Ma. $SO_4$ is somewhat higher throughout and $\delta^{34}S$ variations are reduced. $\delta^{13}C$ is higher in the early Paleozoic and Mesozoic improving fit to the long-term mean. $^{87}Sr/^{86}Sr$ is increased markedly throughout, considerably improving the (still poor) fit to data.

## 3.5. Introducing new forcing factors

We now take forward the new baseline model with this updated set of fluxes and the updated *D*, *U*, *E*, *W*, *B* and $CP_{land}$ forcing (black dashed line), and consider the effect of additional forcing factors, with the results shown in Figure 9.

Basalt area forcing (blue), which is relatively low in the early-mid Paleozoic, tends to increase $CO_2$ until the East European craton event at ~380 Ma temporarily lowers it. $CO_2$ remains somewhat increased until the ~250 Ma Siberian traps emplacement, and then is decreased from the emplacement of the Central Atlantic Magmatic Province (CAMP) at ~200 Ma onwards, which creates greater than present volcanic rock area. The corresponding effect on $^{87}Sr/^{86}Sr$ is to increase it in the Paleozoic and decrease it in the Mesozoic-Cenozoic, which improves the overall fit to the data, including capturing the Phanerozoic minimum of $^{87}Sr/^{86}Sr$ in the Jurassic. Effects on $O_2$, $SO_4$, $\delta^{13}C$ and $\delta^{34}S$ are minimal.

Granite forcing (red), which is relatively high throughout the Paleozoic and early Mesozoic, tends to markedly decrease $CO_2$ until ~150 Ma, generally improving fit to proxy $CO_2$ except in the Triassic. $^{87}Sr/^{86}Sr$ is increased until ~100 Ma considerably improving the fit to data in the Paleozoic. $O_2$ is slightly lowered 400-200 Ma degrading the fit to constraints. $SO_4$ is somewhat lowered prior to ~150 Ma improving the fit to this proxy. Effects on $\delta^{13}C$ and $\delta^{34}S$ are small.

Paleogeography forcing (cyan) has marked effects of increasing $CO_2$ at two particular times of reduced runoff and dry continental interiors; in the early Paleozoic when there is a lack of proxy constraints, and in the Permian-Triassic-Jurassic (~300-150 Ma). The pronounced Triassic $CO_2$ peak better fits proxy data. Increased $CO_2$ represents a readjustment of climate to achieve the same weathering flux. Hence effects on $O_2$, $SO_4$, $\delta^{13}C$, $\delta^{34}S$ are minor, with only a slight dip in $^{87}Sr/^{86}Sr$, meaning these tracers do not provide a further test of the forcing.

Coal depositional area forcing combined with a ramping down of the $CP_{land}$ forcing over 345-300 Ma (green) generates an increase in $O_2$ over 320-240 Ma with a Carboniferous-Permian $O_2$ peak centred on ~300 Ma that improves the fit to the charcoal-based proxy. $\delta^{13}C$ is increased 330-230 Ma reflecting increased organic carbon burial. A corresponding peak in $CO_2$ is generated which is above proxies. Effects on $SO_4$, $\delta^{13}C$ and $\delta^{34}S$ are minimal.

Including an interval of elevated selective weathering of P over 465-400 Ma (together with a combination of all the other new forcing factors; black), generates a 'hump' in atmospheric $O_2$ and $\delta^{13}C$, improving consistency with the earliest charcoal record ~420 Ma onwards, and producing the observed $\delta^{13}C$ +2 ‰, as well as oxygenating the ocean (Lenton et al., 2016). $SO_4$ is also somewhat increased and $\delta^{34}S$ somewhat decreased at this time.

The combination of all the new forcing factors (black), relative to the model without them (black dashed), yields markedly lower early Paleozoic $CO_2$ and higher Permian-Triassic $CO_2$. The overall fit to the $^{87}Sr/^{86}Sr$ record is markedly improved although it is still too low in the earliest Paleozoic and misses a pronounced dip in the Permian. Atmospheric $O_2$ and $\delta^{13}C$ are noticeably improved in parts of the Paleozoic.

With all the various updates to the baseline model, the sedimentary reservoirs behave somewhat differently, with slightly greater growth of the organic carbon reservoir and notably greater shrinkage of the pyrite sulphur reservoir over Phanerozoic time, leading to normalised reservoir sizes of ***g***=1.075, ***c***=0.98, ***pyr***=0.75, ***gyp***=1.25 at present. Much of the deviation from assumed present day reservoir sizes is due to the introduction of pyrite and gypsum degassing fluxes, and a Mesozoic interval of elevated sulphur degassing in which the gypsum reservoir grows at the expense of the pyrite reservoir. However, as the present day sedimentary reservoirs are not that well known and the predictions of surface redox reservoirs of oxygen and sulphate are relatively insensitive to changing the sedimentary reservoir initialisation, we conclude that this mismatch is not a major concern.

## 3.6. Testing hypotheses

Taking the revised baseline model subject to both the updated original forcing factors and the new forcing factors (black dashed line in Figs. 10-12) we now consider some key uncertainties regarding controls on $CO_2$ and alternative hypotheses for controls on $O_2$.

### 3.6.1. Controls on weathering and $CO_2$

We start with key controls on terrestrial and seafloor weathering and hence $CO_2$ (Fig. 10).

In GEOCARB III, Berner switched from the use of $k_{15}$ = 0.15 (~7-fold amplification of weathering by plants) to $k_{15}$ = 0.25 (4-fold amplification by vascular plants relative to moss/lichen cover) based mostly on a field study in Iceland (Moulton et al., 2000). He also explored $k_{15}$ = 0.1 (10-fold amplification). In COPSE, $k_{15}$ = 0.25 (blue) predictably leads to lower early Paleozoic $CO_2$ ~6-7 PAL (and lower temperatures ~16 °C, as opposed to ~18 °C with $k_{15}$ = 0.15). After the rise of the first plants $CO_2$ drops to ~5 PAL which is just below proxies at 420 Ma. Using $k_{15}$ = 0.1 (red) gives higher early Paleozoic $CO_2$ ~14-18 PAL (and higher temperatures ~20 °C). The rise of the first plants draws $CO_2$ down to ~7 PAL, which is consistent with Late Ordovician glaciations (Lenton et al., 2012) and whilst high at 420 Ma is within the 410-390 Ma proxy range. The $CO_2$ predictions for $k_{15}$ = 0.1 are considerably lower than in GEOCARB III for the same parameter setting presumably because COPSE includes a second negative feedback on $CO_2$ from seafloor weathering, which plays a more significant role when abiotic weathering ($k_{15}$) is lower. This can help explain why decreasing $k_{15}$ and increasing $CO_2$ gives slightly lower Paleozoic $O_2$, because now seafloor weathering makes up a larger fraction of the $CO_2$ removal flux but is not a source of P. It also explains why early Paleozoic $^{87}Sr/^{86}Sr$ is somewhat lowered. Conversely increasing $k_{15}$ and lowering $CO_2$ gives slightly higher Paleozoic $O_2$, because continental weathering is now a larger fraction of the $CO_2$ removal flux with a correspondingly increased source of P, and $^{87}Sr/^{86}Sr$ is somewhat increased. Early Paleozoic $SO_4$ shows a small change in the same direction as $O_2$ but there is no significant effect on $\delta^{34}S$ or $\delta^{13}C$. Thus the best chance to evaluate the strength of the biotic weathering effect is from comparison to

1173 $CO_2$ proxies, which are most consistent with the default ~7-fold amplification of weathering ($k_{15}$ =
1174 0.15).

1175 Making weathering dependent on vegetation NPP rather than biomass (green) removes any effect of
1176 fires suppressing weathering by suppressing biomass. This leads to a somewhat slower drawdown of
1177 $CO_2$ with the early rise of plants (because the beneficial effect of fewer fires on vegetation now does
1178 not affect weathering). There are markedly smaller $CO_2$ variations after the rise of plants, and
1179 correspondingly a more stable temperature, reflecting a more effective negative feedback on $CO_2$
1180 and climate when it is not affected by $O_2$ variations. Effects on $O_2$ are tiny, whereas there are small
1181 but noticeable effects on $\delta^{13}C$ because carbon isotope fractionation is assumed to be sensitive to
1182 $CO_2$ level. There are no significant effects on $^{87}Sr/^{86}Sr$, $SO_4$, or $\delta^{34}S$. Hence the best evaluation is
1183 against $CO_2$ proxies, which are better fitted in the latest Paleozoic, but the model predictions appear
1184 rather low in parts of the Jurassic-Cretaceous.

1185 Giving seafloor weathering stronger temperature sensitivity (cyan) generally lowers $CO_2$, $O_2$ and
1186 $^{87}Sr/^{86}Sr$ except in the late Paleozoic. It is unclear whether overall this improves the fit to data.
1187 Removing the temperature sensitivity of seafloor weathering (magenta) markedly increases $CO_2$ and
1188 $O_2$ and somewhat increases $^{87}Sr/^{86}Sr$. This creates Permian-Triassic $CO_2$ levels above the proxies and
1189 increases late Cretaceous-early Ceonozoic $CO_2$ above proxies.

1190 Varying climate sensitivity (Fig. 11) predominantly affects $CO_2$ predictions. $O_2$, $\delta^{13}C$ and $SO_4$ change in
1191 the same direction as $CO_2$ but by relatively small amounts. Prior to the rise of plants, temperature
1192 changes in the opposite direction to $CO_2$, because they are jointly determining the abiotic
1193 weathering flux (e.g., a decrease in climate sensitivity lowers the temperature requiring an increase
1194 in $CO_2$ and temperature to attain the same weathering flux, but because both $CO_2$ and temperature
1195 increase the weathering flux, the temperature does not have to increase to its original value). After
1196 the rise of plants, temperature predictions are little altered, because the biotic weathering flux is
1197 controlled by temperature and insensitive to $CO_2$ (as the Michaelis-Menten response of plants tends

1198 to be saturated) hence variations in climate sensitivity alter $CO_2$ to achieve roughly the same
1199 temperature. Halving the climate sensitivity to 1.5°C (blue) demands much larger increases in $CO_2$
1200 throughout to maintain balance in the carbon cycle, putting predicted $CO_2$ well above proxies most
1201 of the time, and can be ruled out on these grounds. Early Paleozoic temperature is also decreased
1202 from ~18°C to ~15°C (not shown), although early Paleozoic $^{87}Sr/^{86}Sr$ is increased, slightly improving
1203 the fit to data. A more modest decrease in climate sensitivity to 2.25°C (green) is more consistent
1204 with the $CO_2$ proxies, indicating that they help provide a lower bound on climate sensitivity (Royer et
1205 al., 2007). Doubling the climate sensitivity to 6°C (red) lowers $CO_2$ throughout, putting it below
1206 proxies in the early Devonian and mid Triassic, although the fit is improved at some other times.
1207 Early Paleozoic temperature is increased from ~18°C to ~22°C (not shown), but early Paleozoic
1208 $^{87}Sr/^{86}Sr$ is decreased, further degrading the already poor fit to data. A more modest increase in
1209 climate sensitivity to 4.5°C (cyan) is more consistent with the wider literature (IPCC, 2013) and
1210 provides a somewhat better fit to $CO_2$ proxies than with a 6°C climate sensitivity. Hence we consider
1211 2.25-4.5°C as a reasonable uncertainty range on climate sensitivity.

1212 ### 3.6.2. Controls on $O_2$

1213 Turning to controls on $O_2$ we first tried removing the dependence of oxidative weathering of organic
1214 carbon on $O_2$ as suggested by Berner (2006a). However, this causes $O_2$ levels to drop to zero (not
1215 shown), with the long model spin-up (and this also happens in the original model 'run 3' of Bergman
1216 et al., 2004, when using our longer spin-up). The reason is a simple lack of negative feedback on $O_2$,
1217 and given evidence for an $O_2$ sensitivity of oxidative weathering we retain it in the model.

1218 The results of testing other hypotheses for controls on $O_2$ are summarised in Figure 12.

1219 Next we tested the effects of Berner's (2006a) proposal that organic carbon burial is predominantly
1220 controlled by erosion. Forcing terrestrial-derived organic carbon (and phosphorus) burial with
1221 uplift/erosion (blue) leads to lower predicted $O_2$ when uplift is below present, especially in the
1222 Triassic-Jurassic, although $O_2$ is still sufficient to sustain combustion at this time. $CO_2$ is also lowered

1223 from 330 Ma onwards degrading the fit to proxies in the Mesozoic. $\delta^{13}C$ is lowered when uplift is
1224 below present because the reduction in terrestrial-derived organic carbon burial causes a
1225 corresponding reduction in total organic carbon burial. Forcing marine organic carbon burial with
1226 uplift/erosion (red) leads to almost identical effects on $O_2$. Effects on $CO_2$ are also comparable.
1227 However, there is little effect on $\delta^{13}C$ because the reduction in $O_2$ levels leads to a compensatory
1228 increase in terrestrial productivity and terrestrially-derived organic carbon burial. Forcing both
1229 marine and terrestrial-derived organic carbon burial with uplift/erosion (green) (leaving only burial
1230 of terrestrial material in coal basins independent of uplift) leads to markedly lower $O_2$ especially in
1231 the later Triassic-Jurassic when it is insufficient to sustain combustion and therefore inconsistent
1232 with the charcoal record. $CO_2$ is also lowered from 330 Ma onwards, because there is less
1233 suppression of vegetation by fire and therefore faster weathering, and is well below proxies through
1234 much of the Mesozoic. $\delta^{13}C$ is markedly lowered and clearly below the proxy record in the Triassic.
1235 Given these deficiencies we rule out this model version.

1236 Finally we considered alternative marine-based feedbacks on atmospheric oxygen. Including a direct
1237 feedback of $O_2$ on marine organic carbon burial (cyan) leads to smaller $O_2$ variations overall,
1238 including an early Paleozoic increase and slight lowering of later peaks, consistent with an additional
1239 negative feedback (some small $CO_2$ effects go along with this). However, early Paleozoic $\delta^{13}C$ is
1240 increased and $\delta^{34}S$ decreased away from the proxy data. Including Van Cappellen and Ingall's (1996)
1241 feedback of anoxia on $(C/P)_{organic}$ burial ratio (magenta) increases early Paleozoic $O_2$, but has no
1242 effect after the rise of plants because anoxia never significantly returns to the ocean. It also
1243 increases early Paleozoic $\delta^{13}C$ and decreases early Paleozoic $\delta^{34}S$ away from the proxy data. Including
1244 anoxia-sensitive Ca-P burial has almost identical effects on $O_2$ and the other variables as the Van
1245 Cappellen and Ingall (1996) feedback (hence is not shown).

## 3.7. Robust features and remaining uncertainties

We present the new baseline model run and a summary of the preceding uncertainty analysis (Section 3.6) as a grey shaded area around it in Figure 13; adding the variables of global temperature, anoxic fraction, ocean nitrate and ocean phosphate concentration, to $pCO_2$ (PAL) and plotting $pO_2$ (PAL) rather than mixing ratio (%). The greatest uncertainty for most of these variables is, appropriately, in the early Paleozoic. This summary figure and the full set of earlier model results allow us to establish which model predictions withstand testing against proxy data and are robust to current uncertainties, and which critical uncertainties remain that could be targeted by future work. We arrange this chronologically into phases in the development of the Phanerozoic Earth system.

Phase 1 is the early Paleozoic, specifically the Cambrian and the early Ordovician prior to the rise of land plants (~550-465 Ma). Atmospheric $CO_2$ levels at this time are particularly uncertain due to a lack of proxies and because COPSE cannot reproduce the unusually high $^{87}Sr/^{86}Sr$. This suggests that despite the assumed much greater non-volcanic silicate rock area and much smaller volcanic rock area relative to the present, we are still missing a yet more radical change in lithology (e.g. ongoing effects of the pan-African orogeny; Goddéris et al., 2017) or a marked reduction in hydrothermal input of Sr (which might imply lower degassing than assumed). Global temperature predictions from such a simple model should be viewed as 'zeroth-order' given that many climatic factors are not included. Nevertheless relatively warm predicted temperatures of 16-21°C are broadly consistent with no ice at the poles in the Cambrian-early Ordovician.

The model robustly predicts low atmospheric $O_2$ ~0.2 (0.1-0.4) PAL or ~5 (3-10) % mixing ratio and widespread ocean anoxia in the early Paleozoic, supported by low $\delta^{13}C$ and high $\delta^{34}S$ (as well as several independent redox proxies). In the model, the principal $O_2$ regulator around ~0.2 PAL is the oxygen sensitivity of oxidative weathering, as postulated for much of the Proterozoic as well as the earliest Phanerozoic (Daines et al., 2017). The upper part of the $O_2$ uncertainty range includes additional marine-based negative feedbacks on $O_2$, but we consider these $O_2$ values and the

corresponding feedbacks less plausible because they tend to increase predicted $\delta^{13}C$ and decrease predicted $\delta^{34}S$ away from the data. Such low $O_2$ ~0.2 PAL is still consistent with the estimated metabolic needs of the Cambrian fauna (Sperling et al., 2015a). The high predicted anoxic fraction should be viewed semi-quantitatively given the schematic nature of the function. Nevertheless complex models show that the deeper ocean would be mostly anoxic for $O_2$ ~0.2 PAL and limiting nutrient concentration near present levels, assuming a biological carbon pump (Lenton and Daines, 2017). The large increase in anoxia relative to today qualitatively alters the predicted nutrient balance of the early Paleozoic ocean, supporting a much larger increase in water-column denitrification and a corresponding increase in phosphate relative to the Redfield ratio, such that nitrogen fixation can balance denitrification. The prediction of high ocean [$PO_4$] is consistent with evidence from iron formations combined with the inference of high ocean [Si] (Planavsky et al., 2010). It does not, however, equate to higher new production or organic carbon burial in COPSE, because available nitrogen (the limiting nutrient) is at comparable levels to today. The early Paleozoic ocean is predicted to be 'non-Redfieldian' with N/P ~5-6 (rather than today's N/P ~14), consistent with the response of nitrogen cycling to anoxic oceans in the GENIE model (Lenton and Daines, 2017).

Phase 2 is the mid Paleozoic rise of land plants, spanning the Late Ordovician-Silurian-Devonian-early Carboniferous (~465-350 Ma). Assuming early Paleozoic $CO_2$ and temperature were relatively high, a two-phase drawdown of atmospheric $CO_2$ and temperature – in the Late Ordovician and Devonian-early Carboniferous – best fits available proxy data. The model associates the first drawdown phase with the rise of the earliest non-vascular plants and the second with the rise of rooted vascular plants (including trees). It also supports a large amplification of weathering rates by vegetation, likely greater than the factor of 4 used in GEOCARBSULF and potentially up to a factor of 10. Predicted Late Ordovician $CO_2$ levels are sufficiently low to explain glaciation at this time, which thanks to the unusual paleogeography could have been abruptly triggered at relatively high global temperature (Pohl et al., 2014; Pohl et al., 2016). COPSE predicts the second phase of $CO_2$ drawdown

associated with the rise of vascular plants 400-350 Ma caused greater global cooling (partly a simple consequence of the natural logarithmic dependence of temperature on $CO_2$). This produces the lowest predicted global temperatures of the Phanerozoic, consistent with the longest-lived interval of glaciations stretching to the lowest latitudes being during the Carboniferous-Permian.

A 'mid-Paleozoic oxygenation event' is robustly predicted, i.e. a major rise in atmospheric $O_2$ and associated oxygenation of the ocean due to the rise of land plants. This represents a change in the oxygen regulation regime, from the predominant negative feedback being on the sink of oxygen (oxidative weathering) to being on the source (organic carbon burial). This requires a substantial secular increase in organic carbon burial, which is here associated with the earliest, non-vascular land plants (Lenton et al., 2016) (unlike in the original COPSE model where it is associated with the later evolution of trees). Others argue that earliest plant productivity and/or effects on weathering could not have been large enough to affect such a change (Edwards et al., 2015; Quirk et al., 2015), but we have yet to find any other way of reproducing the secular changes observed in the multi-proxy record, including the appearance of fossil charcoal by ~420 Ma. The predicted rise of oxygen and oxygenation of the oceans continues with the rise of rooted, vascular plants, but as the oxygen regulation regime has already shifted it proves harder for them to cause changes in atmospheric $O_2$. The predicted dip in $O_2$ and reassertion of ocean anoxia at ~395 Ma is a consequence of the imposed phosphorus weathering forcing designed to reproduce a transient drop in $\delta^{13}C$ at this time, but $O_2$ goes too low given that there is charcoal through this interval (Lenton et al., 2016). It serves to illustrate that the Earth surface redox state could have been particularly sensitive during this oxygenation transition, although the real Earth system had anoxic events later in the Devonian (Algeo and Scheckler, 1998).

With plants established, the model Earth system thereafter is in a regime where atmospheric $CO_2$ tends to be regulated most strongly against decreases (i.e. regulation against a lower limit) and $O_2$ against increases (i.e. regulation against an upper limit). There are subsequent variations in both $CO_2$

and $O_2$ but they are smaller than the mid-Paleozoic transition, and tend to be reversible rather than one-way changes (albeit very long-lived). Consequently, we treat the rest of the Phanerozoic as 'Phase 3', but we divide it into two parts based on two modelled $CO_2$ and $O_2$ positive excursions.

Phase 3a is the late Paleozoic-early Mesozoic, spanning the Carboniferous-Permian-Triassic (~350-200 Ma) and including the finale of supercontinent (Pangea) formation. There is a broad predicted peak of $CO_2$ in this interval, rising through the later Carboniferous and Permian to a Triassic peak. However, predicted atmospheric $CO_2$ is particularly uncertain because the model cannot reproduce the marked Permian drop in $^{87}Sr/^{86}Sr$, which may indicate uncaptured changes in degassing or lithology. Paleogeography forcing (a particularly dry supercontinent interior) can help explain the Triassic peak seen in $CO_2$ proxies, as would a decoupling of seafloor weathering from surface temperature changes, or a reduction in climate sensitivity. Subsequently the model predicts a $CO_2$ minimum at ~200 Ma around the Triassic-Jurassic boundary which is not seen in proxies. The $CO_2$ drop is due to a mix of LIP emplacement (CAMP), a dip in reconstructed degassing, and a rapid recovery of wetter continental weathering conditions. Part of the problem with the model here is that the CAMP is assumed to weather too rapidly as there is an excessively rapid negative shift in $^{87}Sr/^{86}Sr$.

The model predicts a peak in $O_2$ ~1.35 (1.3-1.4) PAL or ~26.5 (25.5-27) % mixing ratio, centred on ~290 Ma and associated with the Carboniferous-Permian interval of coal deposition. This is comparable to the $O_2$ peak predicted in the original COPSE (Bergman et al., 2004), but below the ~35% (Berner and Canfield, 1989) or ~30% (Berner, 2006a) peak levels predicted with other models. $O_2$ drops to a predicted minimum ~1 (0.85-1.05) PAL or ~21 (18-22) % mixing ratio centred on ~200-190 Ma, which is associated with low organic carbon burial rates including a hiatus in coal deposition during the Triassic. This is consistent with the charcoal record which shows that $O_2$ was sufficient to sustain combustion at this time, and in the model this requires that no more than about half of total organic carbon burial can be controlled by erosion. The maximum and minimum in $O_2$ are linked to a

corresponding predicted maximum and broad minimum in $\delta^{13}C$. The predicted $\delta^{13}C$ fluctuations are comparable in size to those seen in the data compilation, but COPSE does not reproduce the timing and higher frequency of those $\delta^{13}C$ fluctuations well, hence the real $O_2$ record may have exhibited more fluctuations of different timing, albeit within similar bounds. A rise in $SO_4$ to a Permian peak is also predicted, which is due partly to rising $O_2$ but mostly to an assumed decline in ocean [Ca], which then reverses in the Late Permian.

Phase 3b is the mid-late Mesozoic and Cenozoic, spanning the Jurassic-Cretaceous-Paleogene-Neogene (~200-0 Ma), and including the rise of calcareous phytoplankton and the break-up of the supercontinent (Pangea) – with increasing uplift and a peak then decline in degassing. The model captures an overall peak then decline of $CO_2$ driven by the peak in degassing (and to some degree the rise of uplift), but it does not capture the finer scale structure suggested by the proxy compilation. The Phanerozoic minimum and then major rise in $^{87}Sr/^{86}Sr$ is reasonably well captured and attributable to both a decline in degassing causing a decline in hydrothermal Sr input (and shift from seafloor to terrestrial weathering) and a decoupling of volcanic weathering from uplift such that as uplift increases there is a marked shift from weathering of volcanic rocks to ancient cratons (Mills et al., 2014a). The broad global temperature peak in the Late Cretaceous is consistent with paleoclimate reconstructions. The subsequent Paleocene-Eocene peak in temperature is missing, because the model fails to predict a peak in $CO_2$ at this time, and it also fails to capture corresponding stable values of $^{87}Sr/^{86}Sr$ (followed by an accelerated rise). Together these deficiencies may indicate an unresolved Paleocene-Eocene peak in degassing and hydrothermal Sr input. The model does predict a cooling at ~35 Ma (near the Eocene-Oligocene boundary) due to LIP emplacement (the 'Afar' event) driving a $CO_2$ decline.

A broad Late Cretaceous (~90-70 Ma) peak of $O_2$ ~1.3 (1.15-1.5) PAL or ~26 (23.5-28.5) % mixing ratio is robustly predicted, albeit at lower $O_2$ levels than in the original model. It is driven by a peak in degassing and consistent with abundant Cretaceous charcoal. The predicted Cenozoic decline in

1372 $O_2$ is robust. A corresponding predicted decline in $\delta^{13}C$ is consistent with proxies but due more to
1373 changing isotope fractionation than to a decline in organic carbon burial.

## 1374 4. Conclusion: forward look

1375 The process of revising the COPSE model and comparing its predictions to proxy data reveals a mixed
1376 picture with regard to constraining the forcing factors and mechanisms at play in controlling
1377 Phanerozoic $CO_2$ and $O_2$ variations. Trying to reproduce the long timescale structure of $^{87}Sr/^{86}Sr$ does
1378 help constrain key processes of seafloor weathering and the decoupling of volcanic weathering from
1379 uplift that control both $CO_2$ and $O_2$ levels. Trying to reproduce the $\delta^{13}C$ record helps constrain past
1380 $O_2$ variations. However, predicting $\delta^{34}S$ offers little constraint on $O_2$ or even $SO_4$, and whilst
1381 predicting $SO_4$ offers some weak constraint on $O_2$ it is more sensitive to (prescribed) ocean [Ca].
1382 Hence in future there is a need to explore a wider range of proxy data targets to see if they can help
1383 constrain model mechanisms and forcing factors. This in turn may invite a more spatially-resolved
1384 modelling approach for those proxies (e.g. of ocean redox state) that are clearly influenced by both
1385 local and global processes and which hence it is difficult to treat in a globally-averaged way.

1386 Clearly a simplified box model such as COPSE is not expected to capture all features of the proxy
1387 record. More spatially elaborate models are already being used to examine past changes in
1388 weathering (Donnadieu et al., 2006; Goddéris et al., 2014) and in ocean composition (Lenton and
1389 Daines, 2017). In principle a simple model can be calibrated on the results of more realistic complex
1390 models, as is done e.g. for the global temperature function from GEOCARBSULF used here. Equally
1391 new forcing factors can be introduced to represent things not resolved by a simple model, for
1392 example the paleogeography forcing developed for GEOCARBSULF and applied here. However
1393 adding such forcing factors detracts from the transparency of a simplified approach and it runs the
1394 risk of over-fitting it to available data. If one can almost as easily run a more realistic, spatially-

resolved model then that may be a better way to go. Indeed we are developing a framework whereby more elaborate box models can be coupled together and applied to deep time questions.

We have also begun to extend the application of COPSE further back in time to simulate changes in the Proterozoic Earth system (Daines et al., 2017; Mills et al., 2014b). Further work is needed to capture Precambrian forcing, including a more generic approach to the effects of the super-continent cycle on degassing, uplift and LIPs, and the effects of the Earth's decaying internal heat source on degassing. Equally the nature of redox and nutrient cycling in a more anoxic ocean needs elaboration. In principle the model could be extended even further back in time through the Great Oxidation, but this would require some representation of the contribution of methane (and potentially other greenhouse gases) to global temperature.

The results of the present study suggest that there was a major, potentially two-phase, drawdown of atmospheric $CO_2$ with the rise of land plants and associated cooling in the Late Ordovician and Devonian-early Carboniferous. Thereafter atmospheric $CO_2$ was well regulated, particularly against decreases, but there were peaks in the Triassic and mid-Cretaceous. Not all of the structure in the $CO_2$ proxy record is captured, which given its strong dependence on forcing factors suggests that reconstructions of degassing, uplift and changing lithology could be significantly improved.

A mid-Paleozoic oxygenation event is robustly predicted, i.e. a major rise in atmospheric $O_2$ and associated oxygenation of the ocean due to the rise of land plants. Atmospheric $O_2$ is effectively regulated thereafter with remaining fluctuations being a Carboniferous-Permian $O_2$ peak (~26%) linked to burial of terrestrial organic matter in coal swamps, a Triassic-Jurassic $O_2$ minimum (~21%) linked to low uplift, a Cretaceous $O_2$ peak (~26%) linked to high overall degassing and weathering fluxes, and a Cenozoic $O_2$ decline. Two of these robust features are qualitatively at odds with other models. First, COPSE predicts much lower $O_2$ in the early Paleozoic than GEOCARBSULF or MAGic, consistent with marine redox proxies (Lenton et al., 2016; Sperling et al., 2015b), whilst still being consistent with the metabolic $O_2$ requirements of early animals (Sperling et al., 2015a). Second,

COPSE predicts a Mesozoic peak then Cenozoic decline of $O_2$ rather than a monotonic Mesozoic-Cenozoic rise of $O_2$ as seen in some versions of GEOCARBSULF (Berner et al., 2007; Falkowski et al., 2005). The latter prediction is made by inverting the $\delta^{13}C$ record, but it has been shown that this technique can also produce high Mesozoic $O_2$ followed by a Cenozoic $O_2$ decline (Mills et al., 2016), consistent with COPSE.

## Acknowledgements

We thank Josh Williams for assistance with the basalt area forcing, Noam Bergman for developing the original COPSE model, Andy Watson for input to COPSE over the years, the late Bob Berner for pioneering the field of Phanerozoic biogeochemical modelling, and Dana Royer and an anonymous referee for constructive reviews.

The revised COPSE model code, written in Matlab and under Github version control, is available at https://github.com/sjdaines/COPSE/releases. The code is also available from the lead author on request.

Funding: This work was supported by the Natural Environment Research Council [grant numbers NE/P013651/1, NE/N018508/1] (to T.M.L. and S.J.D.); a Royal Society Wolfson Research Merit Award (to T.M.L.); and a University of Leeds academic fellowship (to B.J.W.M.).

# Figures and captions

(a)

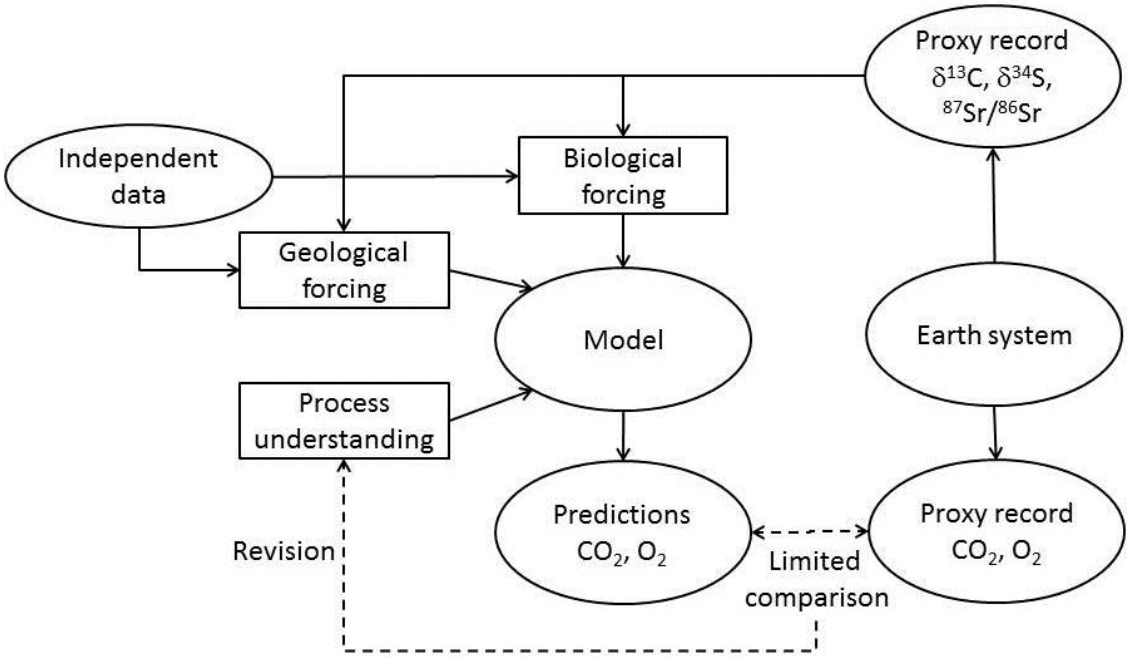


(b)

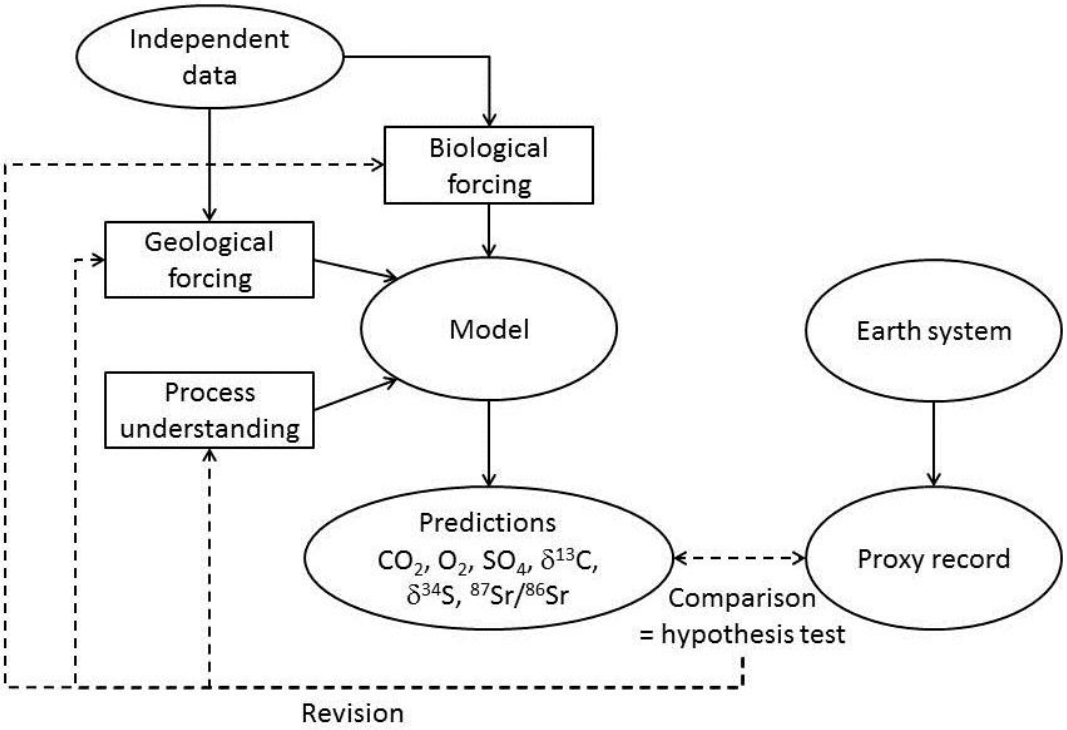


**Figure 1. Different approaches to modelling Phanerozoic biogeochemical cycling:** (a) inverse modelling approach (b) forwards modelling approach (pursued herein).

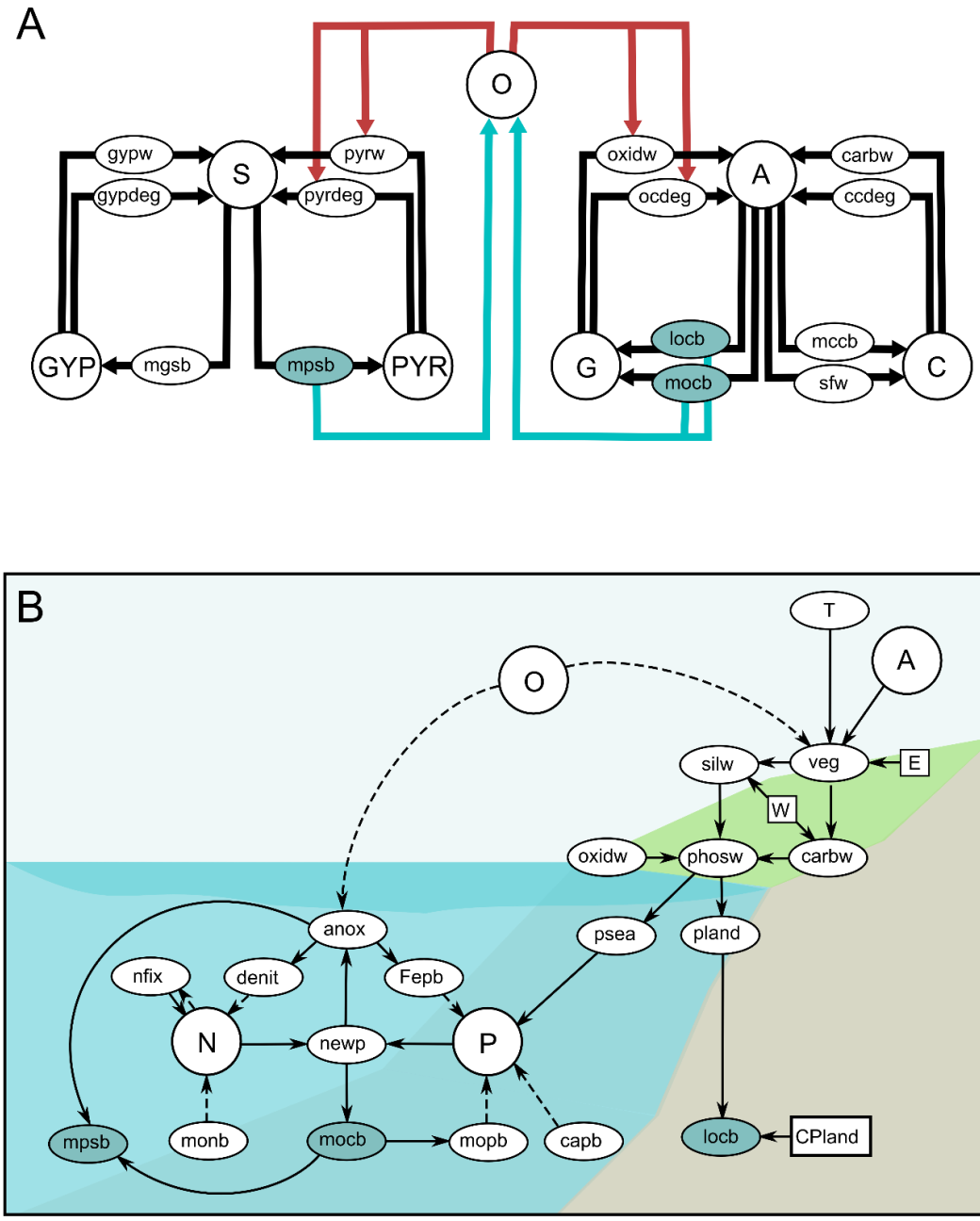


1444

1445 **Figure 2. COPSE model schematic:** (A) Carbon, Sulphur and Oxygen cycle fluxes. Here arrows show

1446 mass fluxes, blue arrows show oxygen sources and red arrows show oxygen sinks. (B) Dynamic

1447 nutrient and biosphere system. Here arrows show positive/direct (solid) or negative/inverse

1448 (dashed) relationships between model parameters. All terms are defined in Tables 1 and 2 and

1449 described in the text. In both diagrams blue ovals show burial fluxes of organic carbon and pyrite

1450 sulphur, which are the long term sources of free oxygen.

1451 *[Print version should be in colour.]*

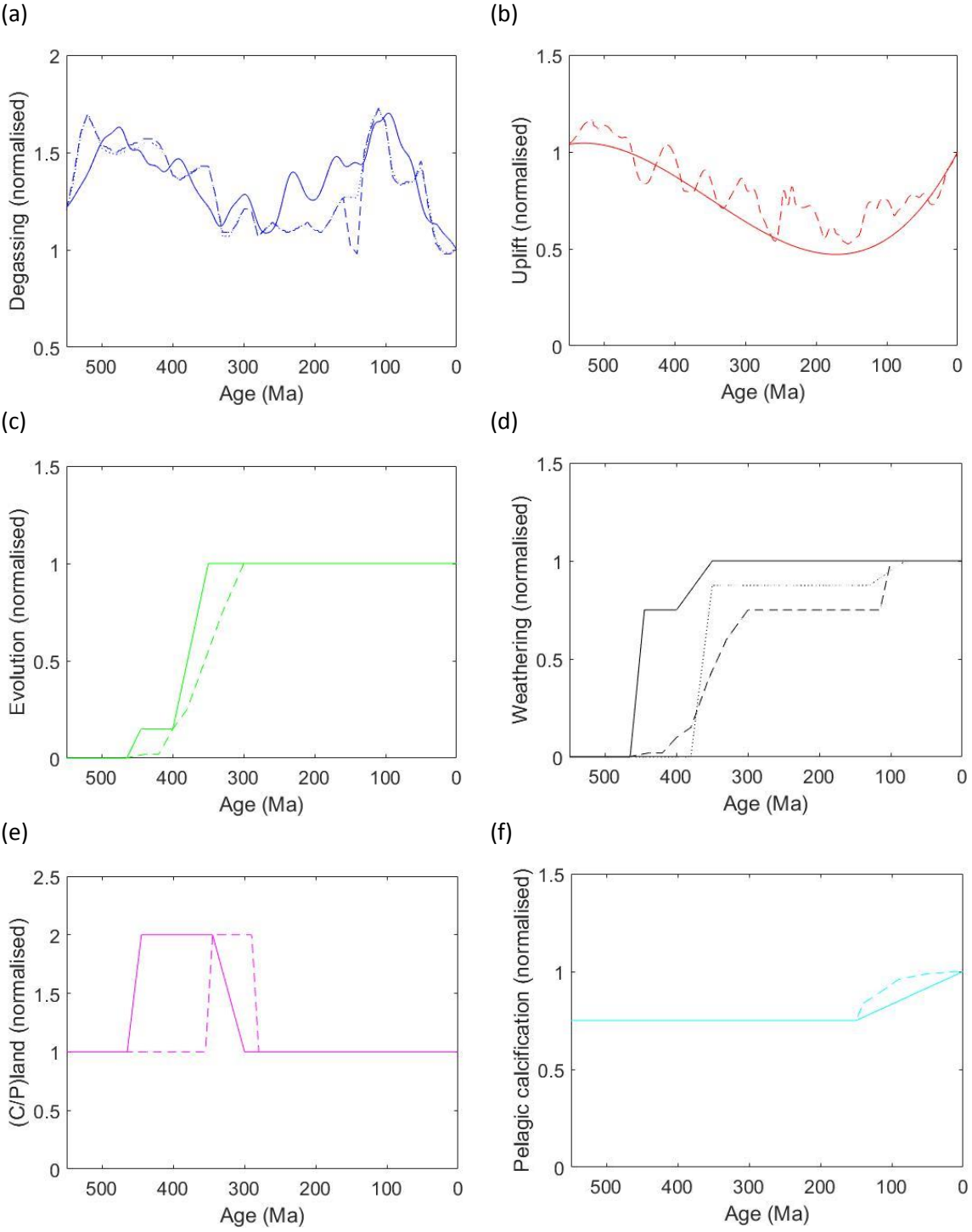


**Figure 3. Updating the original forcing factors:** (a) degassing, *D* (blue), (b) uplift, *U* (red), (c) plant evolution, *E* (green), (d) plant effects on weathering, *W* (black), (e) plant stoichiometry, $CP_{land}$ (magenta), (f) pelagic calcification, *B* (cyan). Original COPSE (dashed), revised COPSE (solid), GEOCARBSULF (dotted).

*[Print version should be in colour.]*

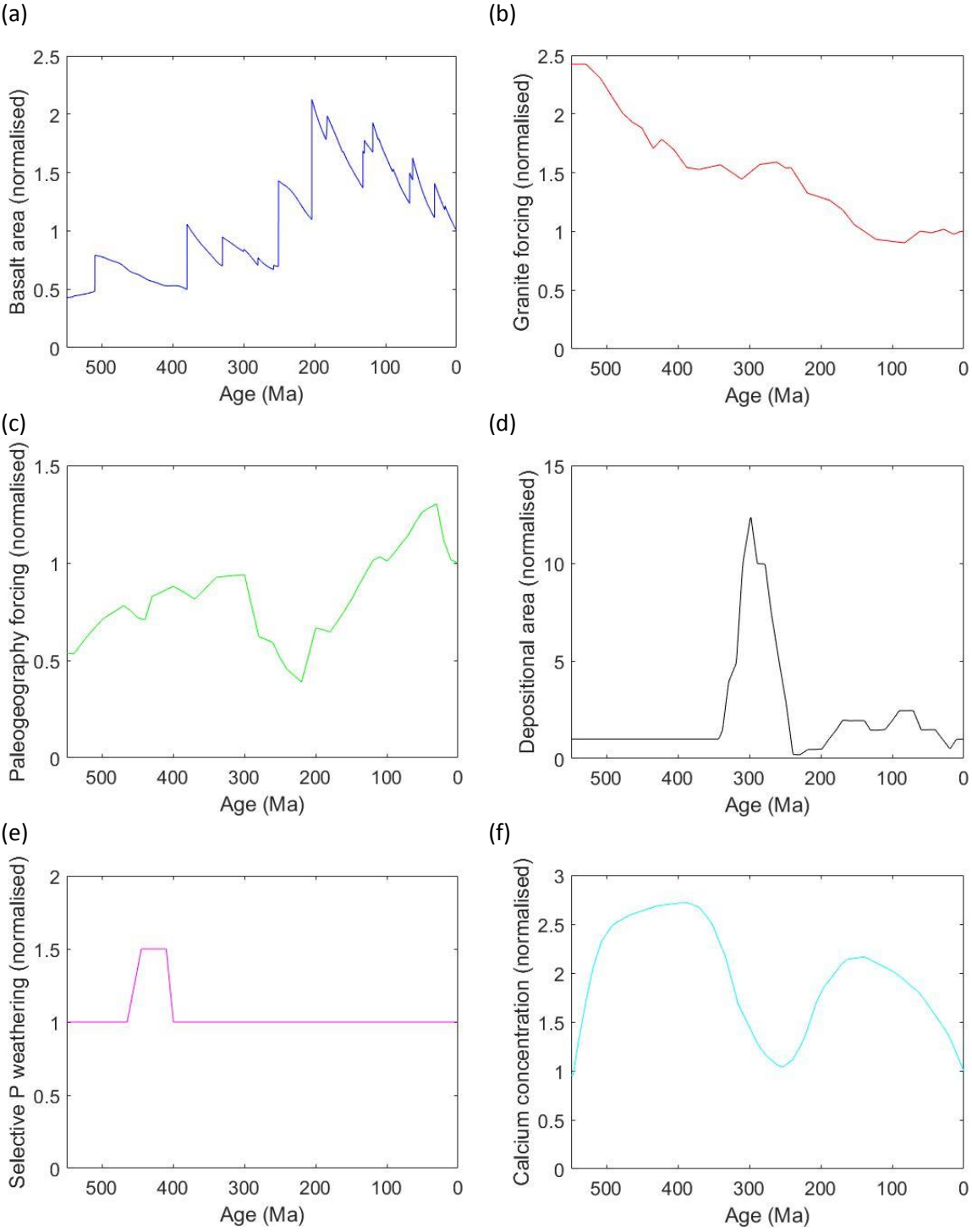


**Figure 4. Additional forcing factors:** (a) 'basalt' (volcanic silicate rock) area, $a_{bas}$ (blue), (b) 'granite' (non-volcanic silicate rock) kinetically-weighted area, $a_{gran}$ (red), (c) paleogeography forcing of runoff, *PG* (green), (d) coal basins depositional area, $b_{coal}$ (black) , (e) selective weathering of phosphorus, *F* (magenta), (f) calcium concentration, $c_{cal}$ (cyan).

*[Print version should be in colour.]*

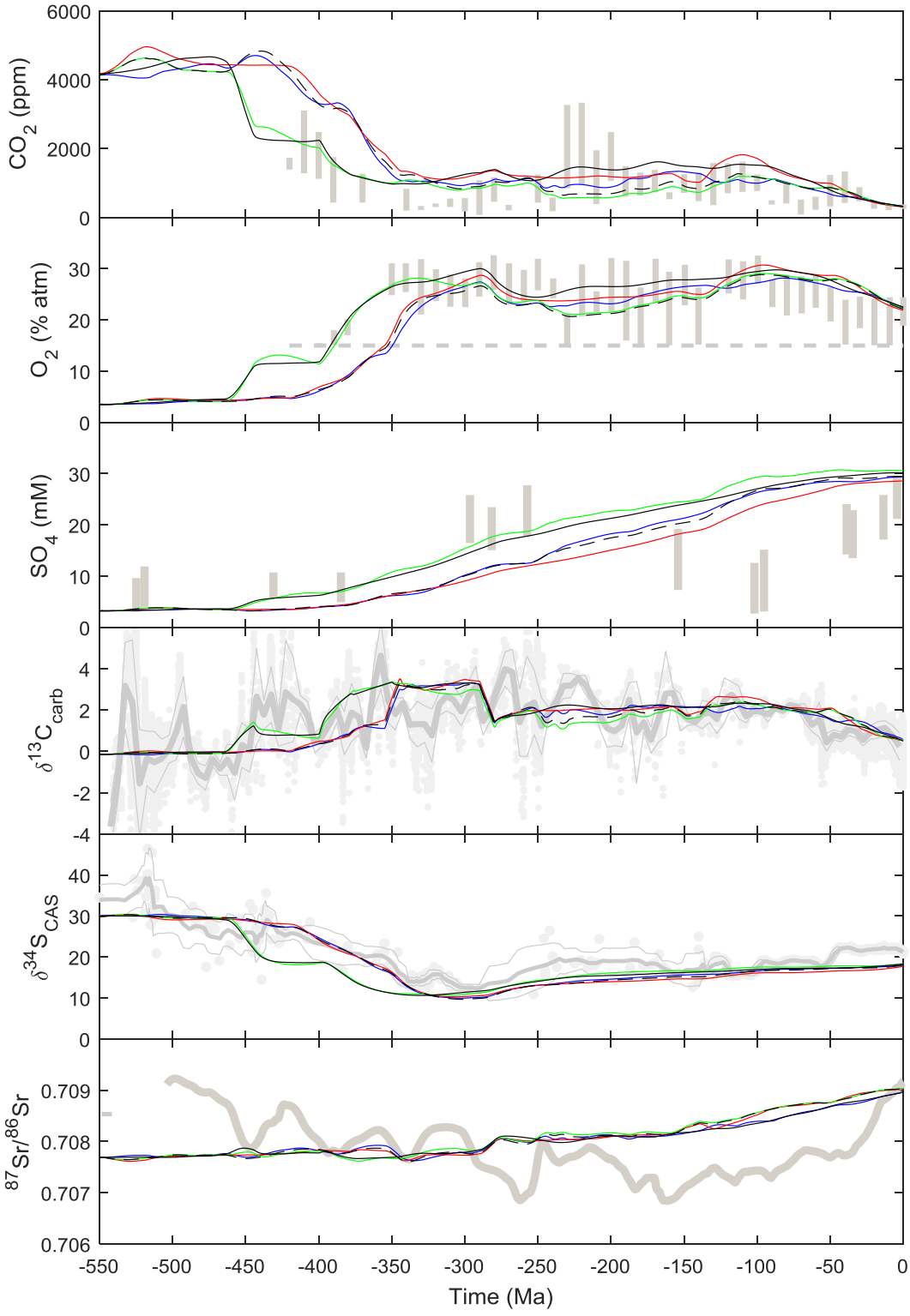


**Figure 5: Effect of updating the original forcing factors on predictions of $CO_2$, $O_2$, $SO_4$, $\delta^{13}C$, $\delta^{34}S$, $^{87}Sr/^{86}Sr$.** Original model (black dashed) with updates to forcing factors: *D* and *B* (blue), *U* (red), *E*, *W* and $CP_{land}$ (green), and all combined (black). Predictions are compared to proxy data in grey (detailed in Table 6); vertical bars for $CO_2$, $O_2$, $SO_4$ are binned data with uncertainty ranges, grey dashed line for $O_2$ is lower limit consistent with charcoal evidence of combustion, dots for $\delta^{13}C_{carb}$ and $\delta^{34}S_{CAS}$ are original data, with running mean (bold line) +/- 1 s.d. (thin lines). *[Print version should be in colour.]*

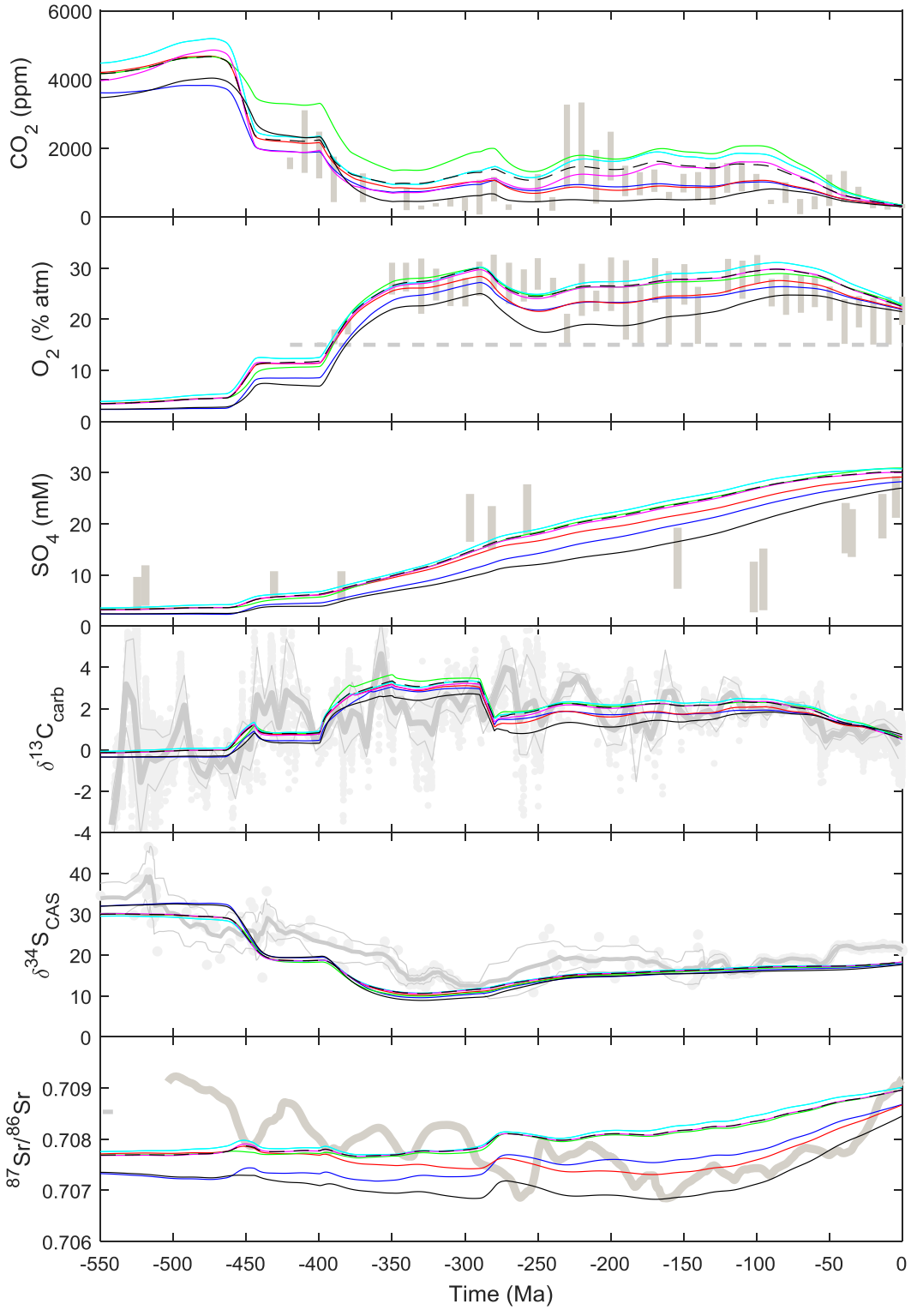


**Figure 6: Effects of updating weathering controls on predictions of $CO_2$, $O_2$, $SO_4$, $\delta^{13}C$, $\delta^{34}S$, $^{87}Sr/^{86}Sr$.** Starting from the original model with updated forcing of *D*, *U*, *E*, *W*, *B*, $CP_{land}$ (black dashed), with individual additions of: seafloor weathering (blue), making basalt weathering independent of uplift (red), distinguishing different activation energies for basalt and granite weathering (cyan), new vegetation dependence of weathering (green), new temperature function (magenta), and combining all these changes (black). *[Print version should be in colour.]*

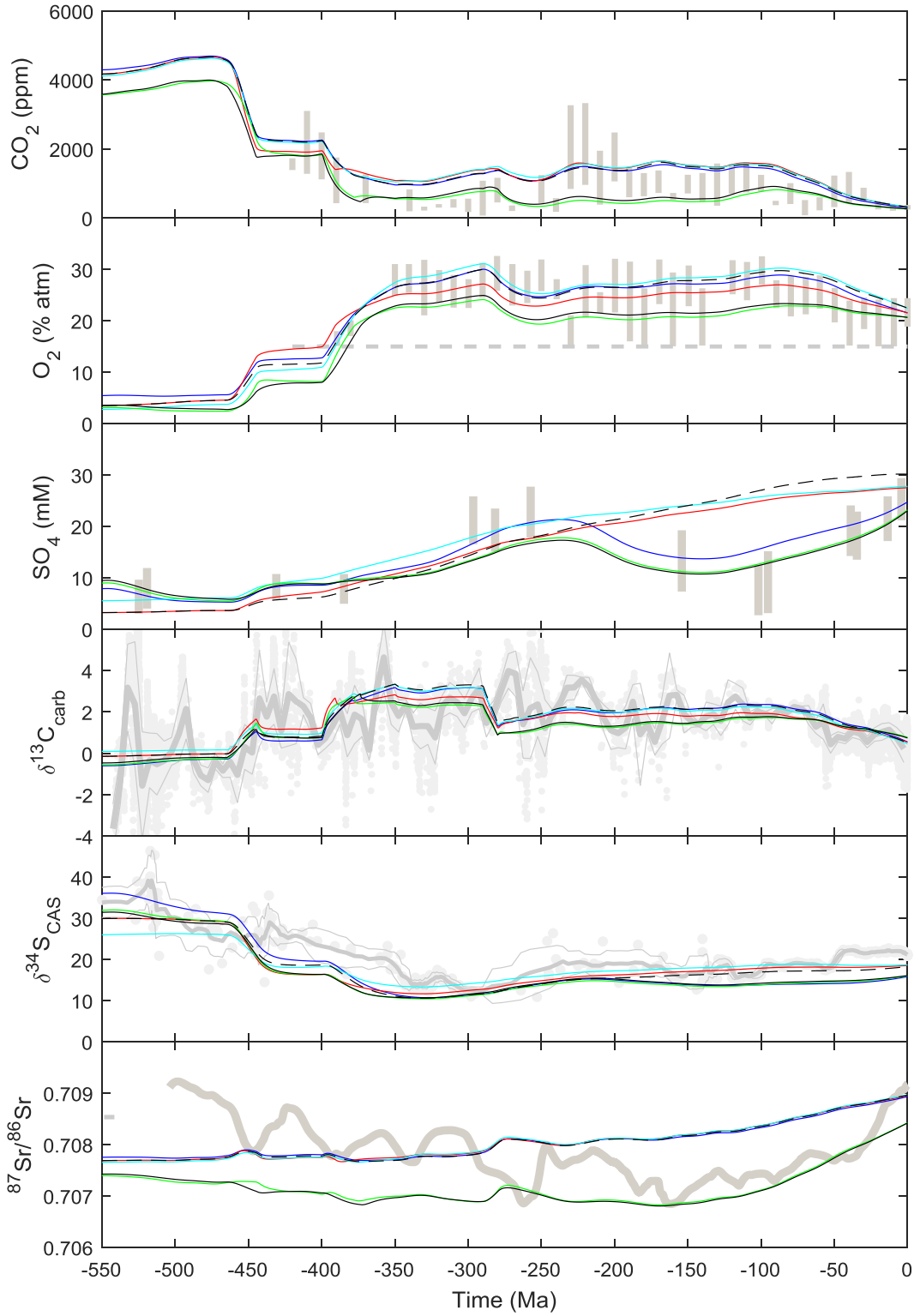


1488

1489 **Figure 7: Effects of updating redox controls and combining changes to the baseline model on**
1490 **predictions of $CO_2$, $O_2$, $SO_4$, $\delta^{13}C$, $\delta^{34}S$, $^{87}Sr/^{86}Sr$.** Starting from the original model with updated
1491 forcing of *D*, *U*, *E*, *W*, *B*, $CP_{land}$ (black dashed), with individual additions of: replacing the interactive
1492 Ca cycle with prescribed [Ca], $c_{cal}$ (blue), new fire feedback on vegetation (red), removing the $O_2$
1493 dependence of pyrite weathering (cyan), combining all these changes with weathering function
1494 updates (green), additionally including all other changes to the baseline model (black). *[Print version*
1495 *should be in colour.]*

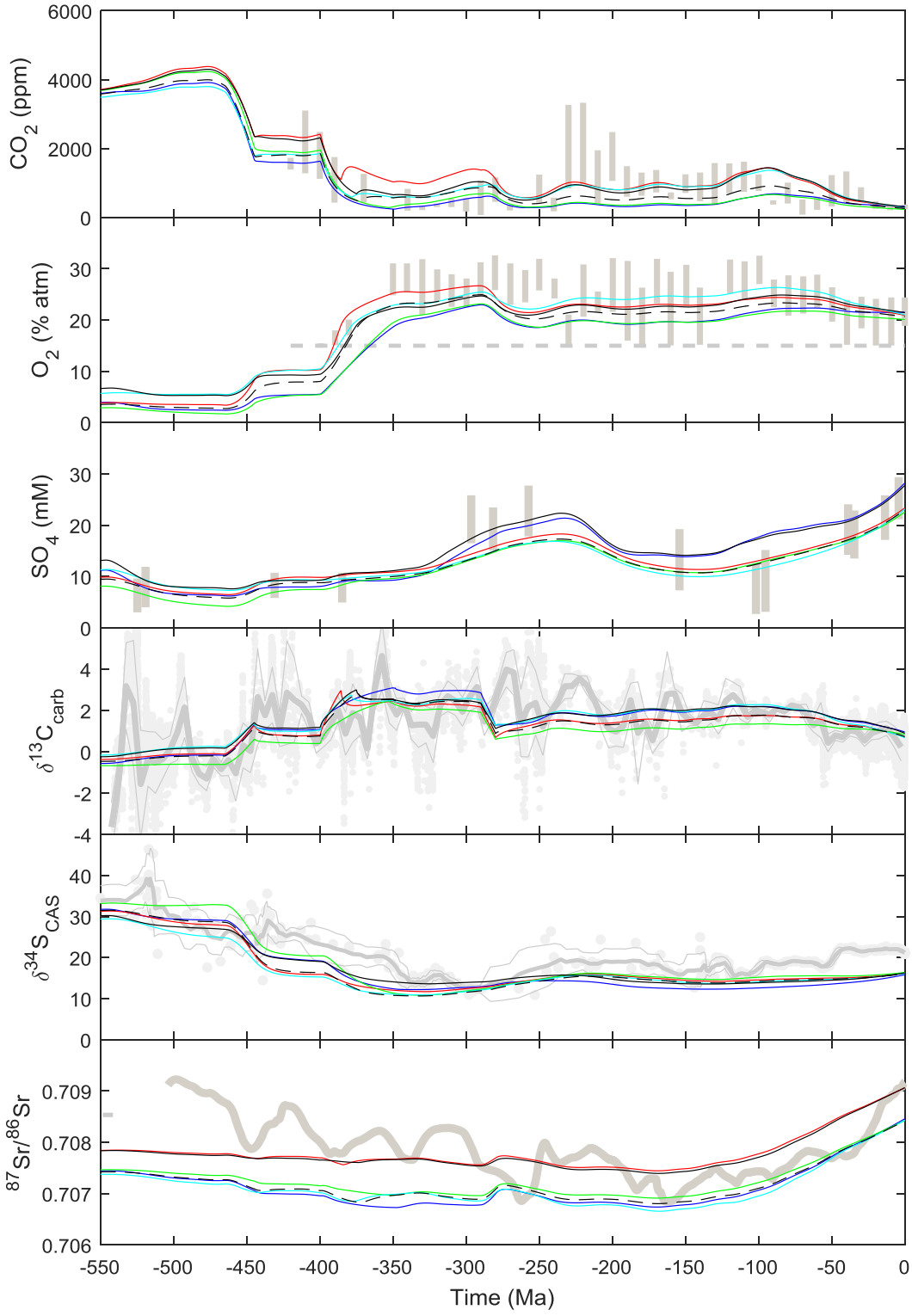


1496

1497 **Figure 8: Effects of updating the baseline fluxes on predictions of $CO_2$, $O_2$, $SO_4$, $\delta^{13}C$, $\delta^{34}S$, $^{87}Sr/^{86}Sr$.**
1498 Starting from the new baseline model with updated forcing of *D*, *U*, *E*, *W*, *B*, $CP_{land}$ (black dashed),
1499 with individual variants from it: high S fluxes (blue), high C inorganic fluxes (red), low C organic fluxes
1500 (green), revised split of P weathering (cyan), and combination of all these flux updates with revised
1501 split of P burial fluxes (black). *[Print version should be in colour.]*

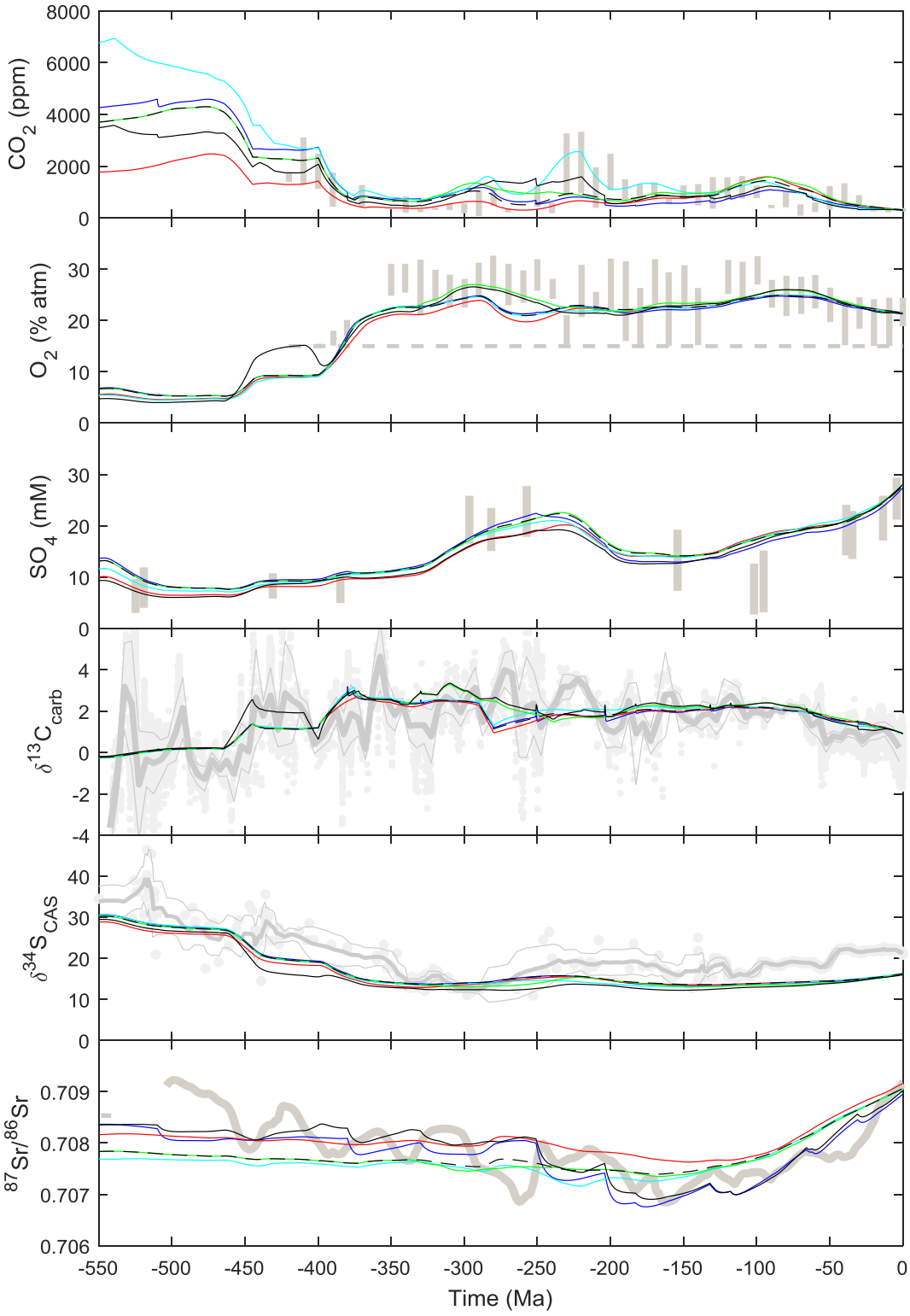


1502

1503 **Figure 9: Effects of new forcing factors on predictions of $CO_2$, $O_2$, $SO_4$, $\delta^{13}C$, $\delta^{34}S$, $^{87}Sr/^{86}Sr$.** Starting
1504 from the new baseline model with updated forcing of *D*, *U*, *E*, *W*, *B*, $CP_{land}$ and updated fluxes (black
1505 dashed), with individual forcing factors: basalt area, $a_{bas}$ (blue), granite area, $a_{gran}$ (red),
1506 paleogeography, *PG* (cyan), coal basin depositional area, $b_{coal}$, with adjustment of $CP_{land}$ (green), all of
1507 the preceding combined with selective weathering of phosphorus, *F* (black). *[Print version should be*
1508 *in colour.]*

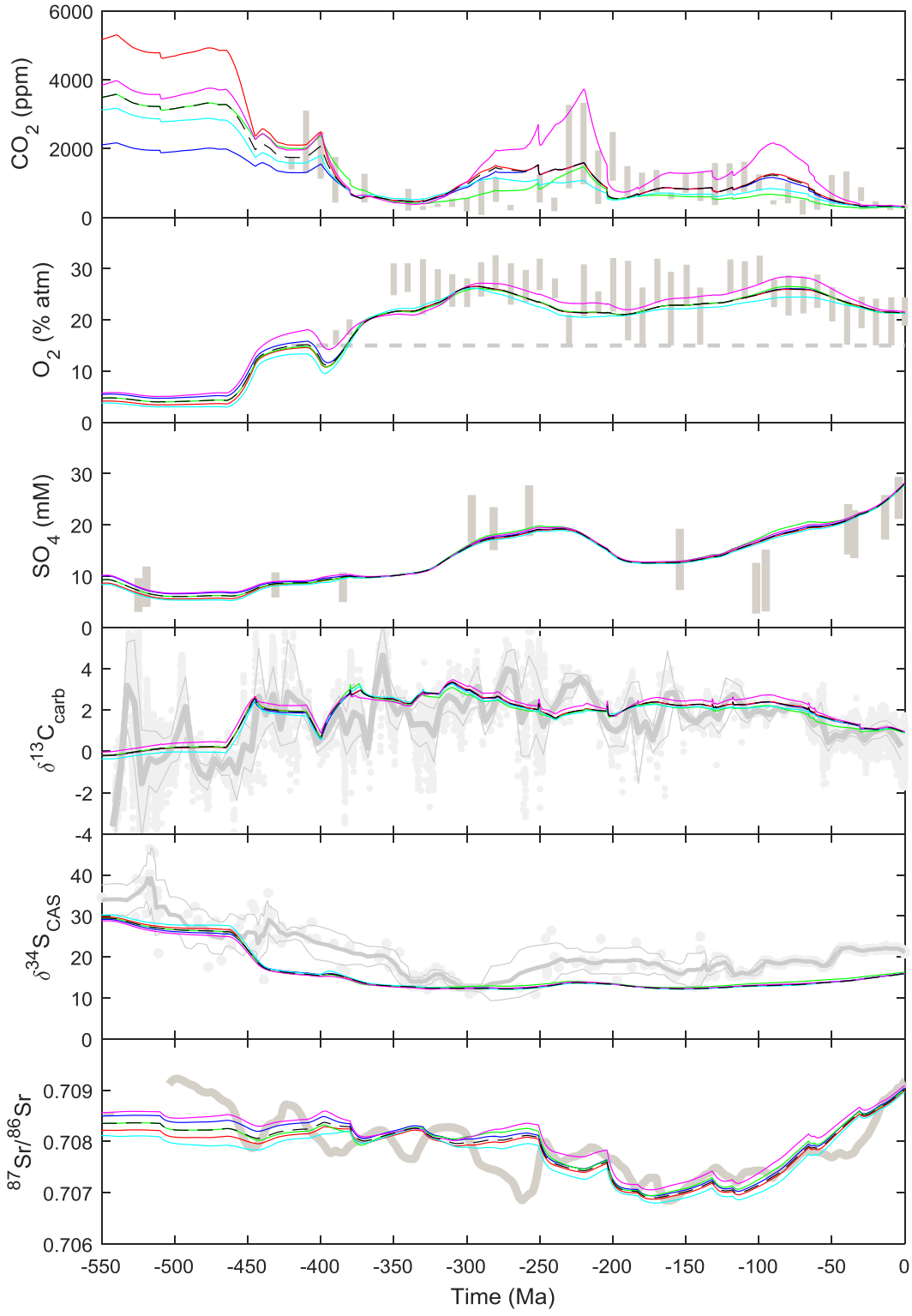


1509

1510 **Figure 10: Testing hypotheses for controls on weathering.** Starting from the new baseline model
1511 with updated original forcing factors, updated fluxes, and new forcing factors (black dashed), with:
1512 4-fold amplification of weathering by plants ($k_{15}$ = 0.25) (blue), 10-fold amplification of weathering
1513 by plants ($k_{15}$ = 0.1) (red), weathering dependent on vegetation NPP (rather than biomass) (green),
1514 stronger temperature sensitivity of seafloor weathering (cyan), no temperature sensitivity of
1515 seafloor weathering (magenta). *[Print version should be in colour.]*

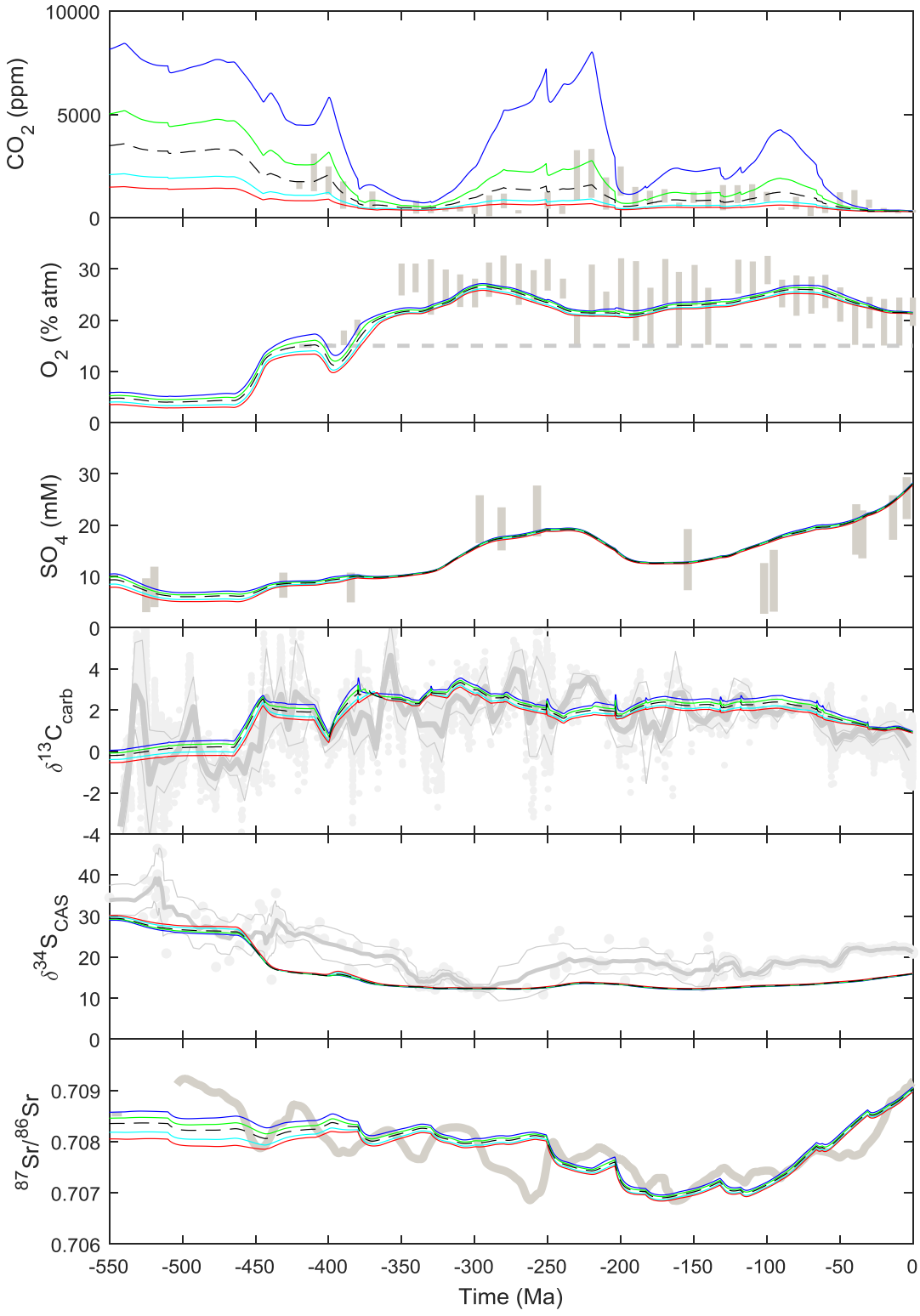


**Figure 11. The effect of varying climate sensitivity.** Starting from the new baseline model with updated original forcing factors, updated fluxes, and new forcing factors, and varying the climate sensitivity from the default 3°C (black dashed) to: 1.5°C (blue), 2.25°C (green), 4.5°C (cyan), 6°C (red). *[Print version should be in colour.]*

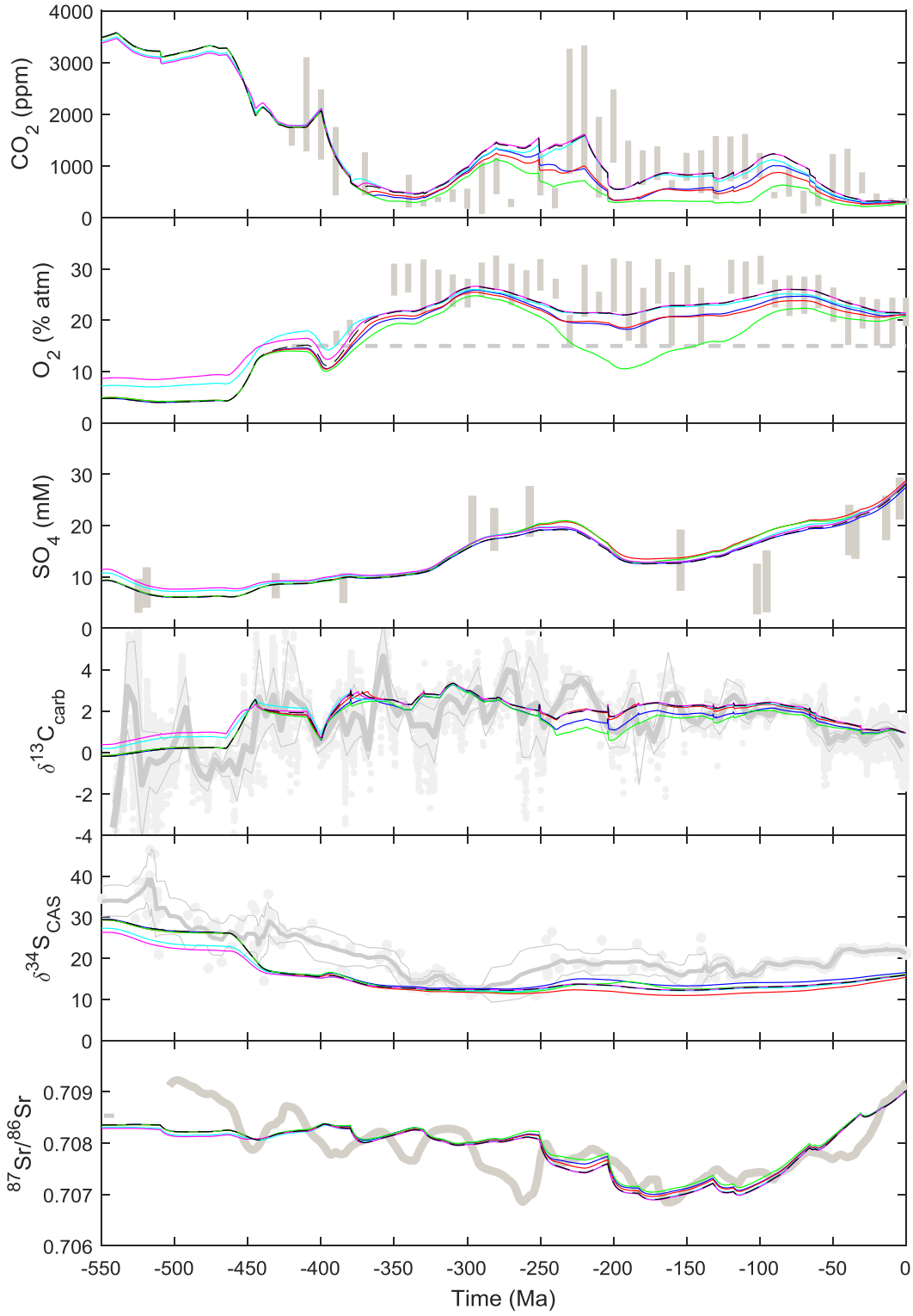


**Figure 12: Testing hypotheses for controls on $O_2$.** Starting from the new baseline model with updated original forcing factors, updated fluxes, and new forcing factors (black dashed), with: land-derived organic carbon burial dependent on uplift (blue), marine organic carbon burial dependent on uplift (red), land-derived and marine organic carbon burial dependent on uplift (green), marine organic carbon burial dependent on $O_2$ (cyan), marine $(C/P)_{organic}$ increasing with anoxia (magenta). *[Print version should be in colour.]*

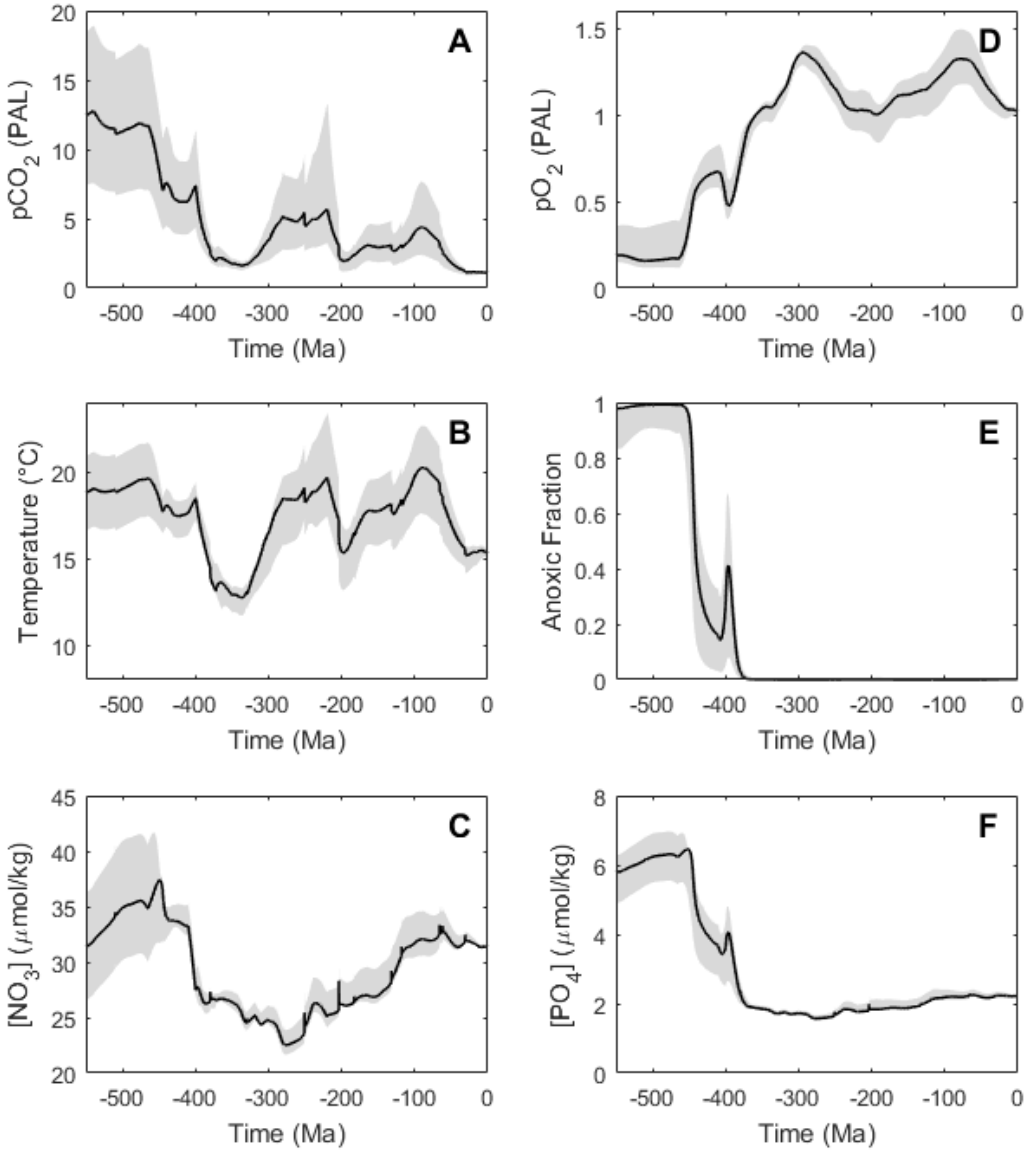


1529

1530 **Figure 13. New best guess model and uncertainty range from testing alternative hypotheses.** The
1531 uncertainty range (in grey) spans all of the hypothesis tests in Section 3.6 and Figures 10-12, with the
1532 exception of climate sensitivities of 1.5°C and 6°C, and the combined uplift forcing of marine and
1533 terrestrial organic carbon burial – because we consider these cases falsified by that analysis: (A)
1534 atmospheric $pCO_2$, (B) global temperature, (C) ocean nitrate concentration, (D) atmospheric $pO_2$, (E)
1535 anoxic fraction of the ocean, (F) ocean phosphate concentration.

# Tables

**Table 1. Core COPSE model reservoirs and differential equations.**

| Reservoir | Label | Differential equation | Initial size (mol) |
|---|---|---|---|
| Ocean (reactive) nitrogen | ***N*** | $\frac{d\boldsymbol{N}}{dt} = nfix - denit - monb$ | $4.35 \times 10^{16}$ |
| Ocean (phosphate) phosphorus | ***P*** | $\frac{d\boldsymbol{P}}{dt} = psea - mopb - fepb - capb$ | $3.1 \times 10^{15}$ |
| Atmosphere-ocean $O_2$ | ***O*** | $\frac{d\boldsymbol{O}}{dt} = locb + mocb - oxidw - ocdeg + 2 \cdot mpsb - 2 \cdot pyrw - 2 \cdot pyrdeg$ | $3.7 \times 10^{19}$ |
| Atmosphere-ocean $CO_2$ | ***A*** | $\frac{d\boldsymbol{A}}{dt} = oxidw + ocdeg + carbw + ccdeg - locb - mocb - mccb - sfw$ | $3.193 \times 10^{18}$ |
| Sedimentary organic (reduced) carbon | ***G*** | $\frac{d\boldsymbol{G}}{dt} = locb + mocb - oxidw - ocdeg$ | $1.25 \times 10^{21}$ |
| Sedimentary carbonate (oxidised) carbon | ***C*** | $\frac{d\boldsymbol{C}}{dt} = mccb + sfw - carbw - ccdeg$ | $5.0 \times 10^{21}$ |
| Ocean (sulphate) sulphur | ***S*** | $\frac{d\boldsymbol{S}}{dt} = gypw + pyrw + gypdeg + pyrdeg - mgsb - mpsb$ | $4.0 \times 10^{19}$ |
| Sedimentary pyrite (reduced) sulphur | ***PYR*** | $\frac{d\boldsymbol{PYR}}{dt} = mpsb - pyrw - pyrdeg$ | $1.8 \times 10^{20}$ |
| Sedimentary gypsum (oxidised) sulphur | ***GYP*** | $\frac{d\boldsymbol{GYP}}{dt} = mgsb - gypw - gypdeg$ | $2.0 \times 10^{20}$ |

1539 **Table 2. Core COPSE model fluxes and baseline values.** ('Original' = Bergman et al., 2004, '$G^3$' = Mills et al., 2014a, 'New' = new baseline arrived at here.)

| Process | Label | Constant | Original | $G^3$ | lowS | highS | low$C_{in}$ | high$C_{in}$ | low$C_{org}$ | high$C_{org}$ | New | Notes |
|---|---|---|---|---|---|---|---|---|---|---|---|---|
| ***Nitrogen cycle*** | | | **$10^{12}$ molN $yr^{-1}$** | | | | | | | | | |
| Nitrogen fixation | *nfix* | $k_3$ | 8.72 | | | | | | (8.67) | | 8.67 | |
| Denitrification | *denit* | $2k_4$ | 8.6 | | | | | | | | 8.6 | |
| Marine organic N burial | *monb* | $k_2/CN_{sea}$ | 0.12 | | | | | | (0.07) | | 0.07 | $CN_{sea}$=37.5 |
| ***Phosphorus cycle*** | | | **$10^{9}$ molP $yr^{-1}$** | | | | | | | | | |
| Reactive P weathering | *phosw* | $k_{10}$ | 43.5 | | | | | | (33.5) | | 42.5 | |
| Terrestrial organic P burial | *pland* | $k_{11}k_{10}$ | 4.5 | | | | | | (2.5) | | 2.5 | $CP_{land}$=1000 |
| Reactive P to ocean | *psea* | $(1-k_{11})k_{10}$ | 39 | | | | | | (31) | | 40 | |
| Marine organic P burial | *mopb* | $k_2/CP_{sea}$ | 18 | | | | | | (10) | | 10 | $CP_{sea}$=250 |
| Iron-sorbed (Fe-P) burial | *fepb* | $k_6$ | 6 | | | | | | | | 10 | |
| Ca-bound (Ca-P) burial | *capb* | $k_7$ | 15 | | | | | | | | 20 | |
| ***Carbon cycle (inorganic)*** | | | **$10^{12}$ molC $yr^{-1}$** | | | | | | | | | |
| Carbonate C degassing | *ccdeg* | $k_{12}$ | 6.65 | 6.65 | | | 6.65 | 15 | | | 15 | |
| Carbonate weathering | *carbw* | $k_{14}$ | 13.35 | 13.35 | | | 13.35 | 8 | | | 8 | |
| Silicate weathering | *silw* | $k_{silw}$ | 6.65 | 4.9 | | | 4.9 | 12 | | | 12 | |
| Granite weathering | *granw* | $k_{granw}$ | | 3.185 | | | 3.185 | 9 | | | 9 | |
| Basalt weathering | *basw* | $k_{basw}$ | | 1.715 | | | 1.715 | 3 | | | 3 | |
| Seafloor weathering | *sfw* | $k_{sfw}$ | 0 | 1.75 | | | 1.75 | 3 | | | 3 | |
| Carbonate burial | *mccb* | $k_{14}+k_{silw}$ | 20 | 18.25 | | | 18.25 | 20 | | | 20 | |
| ***Carbon cycle (organic)*** | | | **$10^{12}$ molC $yr^{-1}$** | | | | | | | | | |
| Organic C degassing | *ocdeg* | $k_{13}$ | 1.25 | | | | | | 1.25 | 1.25 | 1.25 | |
| Oxidative C weathering | *oxidw* | $k_{17}$ | 7.75 | | | | | | 3.75 | 7.75 | 3.75 | |
| Marine organic C burial | *mocb* | $k_2$ | 4.5 | | | | | | 2.5 | 4.5 | 2.5 | |
| Terrestrial organic C burial | *locb* | $k_5$ | 4.5 | | | | | | 2.5 | 4.5 | 2.5 | |
| ***Sulphur cycle*** | | | **$10^{12}$ molS $yr^{-1}$** | | | | | | | | | |
| Gypsum degassing | *gypdeg* | $k_{gypdeg}$ | 0 | | 0 | 0.5 | | | | | 0.5 | |
| Pyrite degassing | *pyrdeg* | $k_{pyrdeg}$ | 0 | | 0 | 0.25 | | | | | 0.25 | |
| Gypsum weathering | *gypw* | $k_{22}$ | 1.0 | | 1.0 | 2.0 | | | | | 2.0 | |
| Pyrite weathering | *pyrw* | $k_{21}$ | 0.53 | | 0.53 | 0.45 | | | | | 0.45 | |
| Gypsum burial | *mgsb* | $k_{mgsb}$ | 1.0 | | 1.0 | 2.5 | | | | | 2.5 | |
| Pyrite burial | *mpsb* | $k_{mpsb}$ | 0.53 | | 0.53 | 0.7 | | | | | 0.7 | |

1540 **Table 3. Model forcing factors.** (All normalised to 1 at present with the exception of insolation.)

| Forcing | Description | Basis | Source(s) |
|---|---|---|---|
| *Original model forcing factors* | | | |
| $I$ | Insolation (solar luminosity) | Stellar physics | (Caldeira and Kasting, 1992) |
| $D$ | Metamorphic and volcanic degassing | Inversion of sea-level curve | (Mills et al., 2017) |
| $U$ | Tectonic uplift | Sediment accumulation rates | (Berner, 2006b; Ronov, 1993) |
| $E$ | Plant evolution and land colonisation | Fossil record and model estimates of global net primary productivity | (Lenton et al., 2016), updated here |
| $W$ | Plant enhancement of weathering | Experimental and field study results | (Lenton et al., 2012), updated here |
| $CP_{land}$ | C/P burial ratio of terrestrial plant material | Attempt to capture Paleozoic coal deposition | (Lenton et al., 2016), updated here |
| $B$ | Apportioning of carbonate burial between shallow and deep seas | Fossil record of evolution of planktonic calicifiers | (Berner, 1994) |
| *Additional forcing factors included herein* | | | |
| $a_{bas}$ | Exposed area of volcanic silicate rocks | Reconstructed area of large igneous provinces (LIPs) and volcanic islands | (Ernst, 2014; Mills et al., 2014a) |
| $a_{gran}$ | Kinetically-weighted area of non-volcanic silicate rocks | Reconstructed lithology of shield, shale, coal, evaporite | (Bluth and Kump, 1991) |
| $PG$ | Paleogeography effect on runoff/weathering | Climate model simulations | (Royer et al., 2014) |
| $b_{coal}$ | Depositional area of coal basins | Coal abundance data | (Bartdorff et al., 2008) |
| $F$ | Selective biotic weathering of P relative to host rocks | Experimental results | (Lenton et al., 2012, 2016) |
| $c_{cal}$ | Ocean calcium concentration | Best fit to fluid inclusion data | (Horita et al., 2002) |
| *Further forcing factors experimented with but not included here* | | | |
| $D_{\mathrm{LIP}}$ | Degassing associated with LIP emplacement | Volume of emplaced LIPs | (Ernst, 2014; Mills et al., 2014a) |
| $a_{carb}$ | Exposed carbonate area | Reconstructed lithology | (Bluth and Kump, 1991) |
| $a_{shale}$ | Exposed shale area | Reconstructed lithology | (Bluth and Kump, 1991) |
| $a_{org}$ | Exposed organic (shale + coal) area | Reconstructed lithology | (Bluth and Kump, 1991) |
| $a_{evap}$ | Exposed evaporite area | Reconstructed lithology | (Bluth and Kump, 1991) |
| $b_{evap}$ | Depositional area of evaporites | Reconstructed lithology | (Bluth and Kump, 1991) |

1541

1542 **Table 4. Changes to the baseline COPSE model functional forms**

| Functional form used in the new baseline model | Original functional form |
|---|---|
| $CO_2 = \boldsymbol{a}^2$ | $CO_2 = \boldsymbol{a}$ |
| $\Delta T = k_c \cdot \ln CO_2 - k_l \cdot t/570$ | Complex function from Caldeira and Kasting (1992) |
| $ignit = min(max(48 \cdot mO_2 - 9.08, 0), 5)$ | $ignit = max(586.2 \cdot mO_2 - 122.102, 0)$ |
| $gypdeg = k_{gypdeg} \cdot D \cdot \boldsymbol{gyp}$ | - |
| $pyrdeg = k_{pyrdeg} \cdot D \cdot \boldsymbol{pyr}$ | - |
| $sfw = k_{sfw} \cdot D \cdot e^{k_T^{sfw} \Delta T}$ | - |
| $f_{biota} = \left[(1 - \min(V \cdot W, 1)) \cdot k_{15} \cdot {CO_2}^{0.5} + V \cdot W\right]$ | $f_{biota} = \left[{CO_2}^{0.5} \cdot (1 - \min(V \cdot W, 1)) + \min(V \cdot W, 1) \cdot \left(\frac{2\boldsymbol{a}}{1+\boldsymbol{a}}\right)^{0.4}\right] \cdot [k_{15} + (1 - k_{15}) \cdot V \cdot W]$ |
| $granw = k_{granw} \cdot U \cdot PG \cdot a_{gran} \cdot f_{Tgran} \cdot f_{runoff} \cdot f_{biota}$ | - |
| $basw = k_{basw} \cdot PG \cdot a_{bas} \cdot f_{Tbas} \cdot f_{runoff} \cdot f_{biota}$ | - |
| $silw = granw + basw$ | $silw = k_{12} \cdot U \cdot f_T \cdot f_{runoff} \cdot f_{biota}$ |
| $carbw = k_{14} \cdot \boldsymbol{C} \cdot U \cdot PG \cdot g_{runoff} \cdot f_{biota}$ | $carbw = k_{14} \cdot U \cdot g_{runoff} \cdot f_{biota}$ |
| $gypw = k_{22} \cdot \boldsymbol{gyp} \cdot U \cdot PG \cdot g_{runoff} \cdot f_{biota}$ | $gypw = k_{22} \cdot \boldsymbol{gyp} \cdot U \cdot g_{runoff} \cdot f_{biota}$ |
| $pyrw = k_{21} \cdot U \cdot \boldsymbol{pyr}$ | $pyrw = k_{21} \cdot U \cdot \boldsymbol{pyr} \cdot \boldsymbol{o}^{0.5}$ |
| $phosw = k_{10} \cdot F \cdot \left(k_{Psilw} \cdot \frac{silw}{k_{silw}} + k_{Pcarbw} \cdot \frac{carbw}{k_{14}} + k_{Poxidw} \cdot \frac{oxidw}{k_{17}}\right)$ | $phosw = k_{10} \cdot \left(k_{Psilw} \cdot \frac{silw}{k_{12}} + k_{Pcarbw} \cdot \frac{carbw}{k_{14}} + k_{Poxidw} \cdot \frac{oxidw}{k_{17}}\right)$ |
| $pland = k_{11} \cdot V \cdot phosw \cdot \left(k_{aq} + \left(1 - k_{aq}\right) \cdot b_{coal}\right)$ | $pland = k_{11} \cdot V \cdot phosw$ |
| $anox = \frac{1}{1 + e^{-k_{anox}(k_u \cdot newp' - \boldsymbol{o})}}$ | $anox = max\left(1 - k_1 \cdot \frac{\boldsymbol{o}}{newp'}, 0\right)$ |
| $denit = k_4 \left(1 + \frac{anox}{1 - k_1}\right) \cdot \boldsymbol{n}$ | $denit = k_4 \left(1 + \frac{anox}{1 - k_1}\right)$ |
| $fepb = \frac{k_6}{k_1} \cdot (1 - anox) \cdot \boldsymbol{p}$ | $fepb = \frac{k_6}{k_1} \cdot (1 - anox)$ |
| $mgsb = k_{mgsb} \cdot \boldsymbol{s} \cdot c_{cal}$ | $mgsb = k_{mgsb} \cdot \boldsymbol{s} \cdot \boldsymbol{cal}$ |

1543

1544 **Table 5. Changes to the COPSE model non-flux parameters explored herein.** (Flux parameters are in

1545 Table 2. References and justification for chosen values are given in the text.)

| Label | Meaning | Original model | New default value | Options explored |
|---|---|---|---|---|
| $k_1$ | Present oxic fraction | 0.86 | 0.997527 | - |
| $k_{15}$ | Pre-plant weathering | 0.15 | 0.15 | 0.1, 0.25 |
| $k_{fire}$ | Fire frequency control | 100 | 3 | - |
| $k_c$ | Climate sensitivity control | N/A | 4.328°C | 2.164°C, 3.246°C, 6.492°C, 8.656°C |
| $k_l$ | Luminosity sensitivity control | N/A | 7.4°C | - |
| $k_T^{sfw}$ | Temperature sensitivity of seafloor weathering | N/A | 0.0608 | 0.1332 |
| $k_T^{gran}$ | Temperature sensitivity of granite weathering | 0.09 | 0.0724 | - |
| $k_T^{bas}$ | Temperature sensitivity of basalt weathering | 0.09 | 0.0608 | - |
| $k_{Psilw}$ | Silicates fraction of P weathering | 2/12 | 0.8 | - |
| $k_{Pcarbw}$ | Carbonates fraction of P weathering | 5/12 | 0.14 | - |
| $k_{Poxidw}$ | Oxidative fraction of P weathering | 5/12 | 0.06 | - |
| $k_{aq}$ | Terrestrial organic matter burial fraction in aquatic settings | N/A | 0.8 | - |
| $k_u$ | Nutrient utilisation efficiency | N/A | 0.5 | - |
| $k_{anox}$ | Sharpness of oxic-anoxic transition | N/A | 12 | - |

1546

1547

1548 **Table 6. Proxy data targets to which the model predictions are compared.**

| Variable | Proxy source(s) | Data aggregation | Data sources |
|---|---|---|---|
| $CO_2$ | Stomatal index, phytoplankton alkenones, liverwort $\delta^{13}C$, paleosol $\delta^{13}C$, boron $\delta^{11}B$, nahcolite | 10 Myr bins, +/-1 s.d. | (Royer, 2014) |
| $O_2$ | Charcoal content of coals, scaled between assumed limits of 15% and 25-35% | 10 Myr bins, uncertainty range from uncertain upper limit | (Glasspool and Scott, 2010) lower limit extended to 420 Ma based on (Lenton et al., 2016) |
| $SO_4$ | Fluid inclusion data only | - | (Algeo et al., 2015; Brennan et al., 2004; Horita et al., 2002; Lowenstein et al., 2005) |
| $\delta^{13}C$ | Carbonates from a range of organisms and depths | 5 Myr bins, mean +/-1 s.d. | (Saltzman and Thomas, 2012) |
| $\delta^{34}S$ | Carbonate associated sulphate (CAS) | 9 point moving mean +/-1 s.d. | (Algeo et al., 2015; Kampschulte and Strauss, 2004; Paytan et al., 1998) |
| $^{87}Sr/^{86}Sr$ | Conodont apatite | LOWESS V5, plus one bin for data 543-548 Ma | (McArthur et al., 2012), plus 543-548 Ma data from (Cox et al., 2016) |

1549

# Appendix A: Strontium cycle and its isotopes

A strontium cycle and its isotopes are implemented following Francois and Walker (1992) and Vollstaedt et al. (2014) with some improvements to the formulation described in Mills et al. (2014a). Ocean (*OSr*) and sedimentary carbonate (*SSr*) reservoirs of strontium are considered. The strontium reservoir calculations are summarised in Table A.1, with the fluxes defined and present day baseline values given in Table A.2, and other constants defined in Table A.3. Fluxes of strontium are tied, where possible, to existing model variables via first-order scaling relationships.

The ocean reservoir of strontium (*OSr*) has inputs from the mantle, weathering of old igneous rocks (granites), new igneous rocks (basalts), and sedimentary carbonates, and outputs from incorporation of strontium in (carbonate) sediments and seafloor weathering. Input of strontium to the ocean from the mantle ($Sr_{mantle}$) is assumed to be proportional to degassing ($D$):

$$Sr_{mantle} = k_{Srmantle} \cdot D \tag{A.1}$$

Inputs of strontium to the ocean from weathering of basalts ($Sr_{basw}$) and granites ($Sr_{granw}$) follows the same apportioning as the corresponding carbon fluxes:

$$Sr_{basw} = k_{Srbasw} \cdot \frac{basw}{k_{basw}} \tag{A.2}$$

$$Sr_{granw} = k_{Srgranw} \cdot \frac{granw}{k_{granw}} \tag{A.3}$$

Input of strontium from carbonate sediments ($Sr_{sedw}$) is assumed to scale with carbonate weathering and with the concentration of strontium in the sedimentary carbonate reservoir (the latter differs from Mills et al., 2014a):

$$Sr_{sedw} = k_{Srsedw} \cdot \frac{carbw}{k_{carbw}} \cdot \frac{SSr}{SSr_0} \tag{A.4}$$

Removal of strontium through burial in (carbonate) sediments is assumed proportional to the rate of carbonate sediment deposition and the concentration of strontium in the ocean:

$$Sr_{sedb} = k_{Srsedb} \cdot \frac{mccb}{k_{mccb}} \cdot \frac{OSr}{OSr_0} \quad \text{(A.5)}$$

The rate of strontium removal in seafloor weathering is assumed to depend on the seafloor weathering rate and the strontium concentration in the ocean (the latter differs from Mills et al., 2014a):

$$Sr_{sfw} = k_{Srsfw} \cdot \frac{sfw}{k_{sfw}} \cdot \frac{OSr}{OSr_0} \quad \text{(A.6)}$$

The relative proportions of the burial and seafloor weathering removal fluxes of strontium are assumed to follow the same proportions as the corresponding fluxes in the carbon system, with the total flux dictated by assuming present day steady state for oceanic Sr concentration.

The sedimentary reservoir of strontium (*SSr*) has an input from carbonate burial ($Sr_{sedb}$), and outputs from carbonate weathering ($Sr_{sedw}$) and metamorphic conversion to crustal rocks ($Sr_{metam}$). The output from sediment metamorphism is assumed to be proportional to degassing (*D*) and the concentration of strontium in the sedimentary carbonate reservoir (the latter differs from Mills et al., 2014a):

$$Sr_{metam} = k_{Srmetam} \cdot D \cdot \frac{SSr}{SSr_0} \quad \text{(A.7)}$$

Although there is no fractionation of Sr isotopes associated with the input and output fluxes to the ocean, decay of $^{87}$Rb to $^{87}$Sr influences the $^{87}$Sr/$^{86}$Sr ratio over long timescales (and is responsible for the differing $^{87}$Sr/$^{86}$Sr values between different rock types). The decay process is represented explicitly in the model:

$$^{87}Sr/^{86}Sr_{granite} = {}^{87}Sr/^{86}Sr_0 + {}^{87}Rb/^{86}Sr_{granite}\left(1 - e^{-\lambda t}\right) \quad \text{(A.8)}$$

$$^{87}Sr/^{86}Sr_{basalt} = {}^{87}Sr/^{86}Sr_0 + {}^{87}Rb/^{86}Sr_{basalt}\left(1 - e^{-\lambda t}\right) \quad \text{(A.9)}$$

$$^{87}Sr/^{86}Sr_{mantle} = {}^{87}Sr/^{86}Sr_0 + {}^{87}Rb/^{86}Sr_{mantle}\left(1 - e^{-\lambda t}\right) \quad \text{(A.10)}$$

Where time ($t$) is in years from Earth formation (taken to be 4.5 billion years ago). For each rock type, the present day rubidium-strontium ratio is then calculated (Table A.3) such that the observed present day $^{87}Sr/^{86}Sr$ ratio is achieved for each rock type after 4.5 billion years:

$$^{87}Rb/^{86}Sr = \frac{\left(^{87}Sr/^{86}Sr_{present} - ^{87}Sr/^{86}Sr_0\right)}{\left(1-e^{-\lambda \cdot 4.5\times10^9}\right)} \quad \text{(A.11)}$$

The isotopic composition of the ocean and the sediments are calculated by first creating reservoirs consisting of Sr concentrations multiplied by their isotopic ratios, where $\delta Sr_X$ denotes the $^{87}Sr/^{86}Sr$ ratio of reservoir *X*:

$$\frac{d(OSr\cdot\delta Sr_{ocean})}{dt} = Sr_{granw}\cdot\delta Sr_{granite} + Sr_{basw}\cdot\delta Sr_{basalt} + Sr_{sedw}\cdot\delta Sr_{sediment} + Sr_{mantle}\cdot \delta Sr_{mantle} - Sr_{sedb}\cdot\delta Sr_{ocean} - Sr_{sfw}\cdot\delta Sr_{ocean} \quad \text{(A.12)}$$

$$\frac{d(SSr\cdot\delta Sr_{sediment})}{dt} = Sr_{sedb}\cdot\delta Sr_{ocean} - Sr_{sedw}\cdot\delta Sr_{sediment} - Sr_{metam}\cdot\delta Sr_{sediment} + SSr\cdot\lambda\cdot\left(^{87}Rb/^{86}Sr_{carbonate}\right)\cdot e^{\lambda(4.5\times10^9-t)} \quad \text{(A.13)}$$

The carbonate sediment isotopic reservoir evolution includes a term to account for rubidium decay within the sedimentary reservoir. The present-day rubidium-strontium ratio of sediments $^{87}Rb/^{86}Sr_{carbonate}$, (Table A.3), is calculated to achieve the average crustal $^{87}Sr/^{86}Sr$ of 0.73 (Veizer and Mackenzie, 2003) .

The ocean and sediment $^{87}Sr/^{86}Sr$ ratios are calculated by dividing the new reservoirs by the known concentration or total:

$$\delta Sr_{ocean} = \frac{OSr\cdot\delta Sr_{ocean}}{OSr} \quad \text{(A.14)}$$

$$\delta Sr_{sediment} = \frac{SSr\cdot\delta Sr_{sediment}}{SSr} \quad \text{(A.15)}$$

Present day fluxes are taken from Francois and Walker (1992) with differences being the split of basalt and granite weathering and the split of seafloor weathering and sediment burial. The present

day fluxes are such that although the ocean reservoir is in steady state, the sedimentary pool of strontium is out of steady state and growing. However, over Phanerozoic time the generally greater than present degassing tends to generate shrinkage of the sedimentary reservoir. This shrinkage is buffered considerably by the assumed dependence of metamorphic conversion on the sedimentary strontium reservoir size. Nevertheless the sedimentary reservoir needs to be initialised larger than present (typically $6 \times 10^{18}$ mol) at 600 Ma to approach the present day value.

The choice of present day values for $^{87}Sr/^{86}Sr$ of mantle, basalt and granite together with the corresponding input fluxes determine the present day 'attractor' value ($a$) for the composition of the ocean and sediments, following:

$$a = \left(\frac{k_{Srsilw}}{k_{Srmantle}+k_{Srsilw}}\right) \cdot \left(k_{basfrac} \cdot \delta Sr_{basalt} + \left(1 - k_{basfrac}\right) \cdot \delta Sr_{granite}\right) + \left(\frac{k_{Srmantle}}{k_{Srmantle}+k_{Srsilw}}\right) \cdot \delta Sr_{mantle} \quad \text{(A.16)}$$

Using $k_{basfrac}$=0.25 and the other values from (Francois and Walker, 1992), including $\delta Sr_{granite}$=0.718, gives $a$=0.7105, whereas the ocean is at ~0.709 and sedimentary carbonates at ~0.708, suggesting some internal inconsistency in that set up. Previously we used $\delta Sr_{granite}$=0.715 (Mills et al., 2014a), which gives $a$=0.7091, consistent with the present ocean state, and we adopt that value here.

In our previous work (Mills et al., 2014a) sedimentary carbonate was initialised at $\delta Sr_{sediment}$ = 0.714 in order to recover present day values, but this is hard to justify given that Phanerozoic carbonates have ranged over 0.7065-0.709 and the Neoproterozoic saw a major rise from ~0.706 to ~0.709 (Halverson et al., 2007). The use of a high initial sedimentary $^{87}Sr/^{86}Sr$ tends to drag up the initial ocean $^{87}Sr/^{86}Sr$, but without evidence for such high values here instead we initialise with $\delta Sr_{sediment}$ = 0.708, which is roughly the Phanerozoic average and a reasonable value for the late Neoproterozoic.

1637 **Table A.1. Strontium reservoirs and differential equations.**

| Reservoir | Label | Differential equation | Present size (mol) |
|---|---|---|---|
| Ocean Sr | OSr | $\frac{dOSr}{dt} = Sr_{granw} + Sr_{basw} + Sr_{sedw} + Sr_{mantle} - Sr_{sedb} - Sr_{sfw}$ | $1.2 \times 10^{17}$ |
| Sed. Sr | SSr | $\frac{dSSr}{dt} = Sr_{sedb} - Sr_{sedw} - Sr_{metam}$ | $5 \times 10^{18}$ |

1638

1639 **Table A.2. Strontium fluxes and baseline (present day) values.**

| Process | Label | Constant | Baseline flux (molSr $yr^{-1}$) | Source/Notes |
|---|---|---|---|---|
| (Silicate weathering) | | $k_{Srsilw}$ | $13 \times 10^{9}$ | (Francois and Walker, 1992) |
| Basalt weathering | $Sr_{basw}$ | $k_{basfrac} \cdot k_{Srsilw}$ | | split follows carbon cycle |
| Granite weathering | $Sr_{granw}$ | $(1-k_{basfrac}) \cdot k_{Srsilw}$ | | split follows carbon cycle |
| Sediment weathering | $Sr_{sedw}$ | $k_{Srsedw}$ | $17 \times 10^{9}$ | (Francois and Walker, 1992) |
| Mantle input | $Sr_{mantle}$ | $k_{Srmantle}$ | $7.3 \times 10^{9}$ | (Francois and Walker, 1992) |
| Seafloor weathering | $Sr_{sfw}$ | $k_{Srsfw}$ | | split follows carbon cycle |
| Sediment burial | $Sr_{sedb}$ | $k_{Srsedb}$ | | split follows carbon cycle |
| Sediment metamorphism | $Sr_{metam}$ | $k_{Srmetam}$ | $13 \times 10^{9}$ | (Francois and Walker, 1992) |

1640

1641 **Table A.3. Other constants in the strontium cycle.**

| Constant | Label | Value | Source/Notes |
|---|---|---|---|
| $^{87}$Rb decay rate | $\lambda$ | $1.4 \times 10^{-11}$ $yr^{-1}$ | (Francois and Walker, 1992) |
| Original value | $^{87}Sr/^{86}Sr_0$ | 0.69898 | at formation of the Earth |
| $^{87}$Sr/$^{86}$Sr basalt | $\delta Sr_{basalt}$ | 0.705 | (Francois and Walker, 1992) |
| $^{87}$Sr/$^{86}$Sr granite | $\delta Sr_{granite}$ | 0.715 | reproduces present ocean composition |
| $^{87}$Sr/$^{86}$Sr mantle | $\delta Sr_{mantle}$ | 0.703 | (Francois and Walker, 1992) |
| $^{87}$Rb/$^{86}$Sr mantle | $^{87}Rb/^{86}Sr_{mantle}$ | 0.066 | for correct present day $^{87}$Sr/$^{86}$Sr |
| $^{87}$Rb/$^{86}$Sr basalt | $^{87}Rb/^{86}Sr_{basalt}$ | 0.1 | for correct present day $^{87}$Sr/$^{86}$Sr |
| $^{87}$Rb/$^{86}$Sr granite | $^{87}Rb/^{86}Sr_{granite}$ | 0.26 | for correct present day $^{87}$Sr/$^{86}$Sr |
| $^{87}$Rb/$^{86}$Sr sediments | $^{87}Rb/^{86}Sr_{carbonate}$ | 0.5 | for correct present day $^{87}$Sr/$^{86}$Sr assuming crustal average $^{87}$Sr/$^{86}$Sr of 0.73 |

1642

1643

# References

Algeo, T.J., Luo, G.M., Song, H.Y., Lyons, T.W. and Canfield, D.E., 2015. Reconstruction of secular variation in seawater sulfate concentrations. Biogeosciences, 12(7): 2131-2151.

Algeo, T.J. and Scheckler, S.E., 1998. Terrestrial-marine teleconnections in the Devonian: links between the evolution of land plants, weathering processes, and marine anoxic events. Philosophical Transactions of the Royal Society of London, Series B, 353(1365): 113-130.

Allegre, C.J., Louvat, P., Gaillardet, J., Meynadier, L., Rad, S. and Capmas, F., 2010. The fundamental role of island arc weathering in the oceanic Sr isotope budget. Earth and Planetary Science Letters, 292(1-2): 51-56.

Alt, J.C. and Teagle, D.A.H., 1999. The uptake of carbon during alteration of ocean crust. Geochimica et Cosmochimica Acta, 63(10): 1527-1535.

Amiotte-Suchet, P., Probst, J.-L. and Ludwig, W., 2003. Worldwide distribution of continental rock lithology: Implications for the atmospheric/soil CO2 uptake by continental weathering and alkalinity river transport to the oceans. Global Biogeochemical Cycles, 17(2): 1038.

Andrews, M.Y., Ague, J.J. and Berner, R.A., 2008. Weathering of soil minerals by angiosperm and gymnosperm trees. Mineralogical Magazine, 72(1): 11-14.

Arvidson, R.S., Guidry, M.W. and Mackenzie, F.T., 2011. Dolomite Controls on Phanerozoic Seawater Chemistry. Aquatic Geochemistry, 17(4): 735-747.

Arvidson, R.S., Mackenzie, F.T. and Berner, R.A., 2014. The Sensitivity of the Phanerozoic Inorganic Carbon System to the Onset of Pelagic Sedimentation. Aquatic Geochemistry, 20(2): 343-362.

Arvidson, R.S., Mackenzie, F.T. and Guidry, M., 2006. MAGic: A Phanerozoic Model for the Geochemical Cycling of Major Rock-Forming Components. American Journal of Science, 306(3): 135-190.

Arvidson, R.S., Mackenzie, F.T. and Guidry, M.W., 2013. Geologic history of seawater: A MAGic approach to carbon chemistry and ocean ventilation. Chemical Geology, 362: 287-304.

1670 Bartdorff, O., Wallmann, K., Latif, M. and Semenov, V., 2008. Phanerozoic evolution of atmospheric
1671 methane. Global Biogeochemical Cycles, 22(1): GB1008.
1672 Belcher, C.M. and McElwain, J.C., 2008. Limits for Combustion in Low O2 Redefine Paleoatmospheric
1673 Predictions for the Mesozoic. Science, 321(5893): 1197-1200.
1674 Belcher, C.M., Yearsley, J.M., Hadden, R.M., McElwain, J.C. and Rein, G., 2010. Baseline intrinsic
1675 flammability of Earth's ecosystems estimated from paleoatmospheric oxygen over the past
1676 350 million years. Proceedings of the National Academy of Sciences, 107(52): 22448-22453.
1677 Bergman, N.M., Lenton, T.M. and Watson, A.J., 2004. COPSE: a new model of biogeochemical cycling
1678 over Phanerozoic time. Am. J. Sci., 304: 397-437.
1679 Berner, R.A., 1987. Models for carbon and sulfur cycles and atmospheric oxygen: Application to
1680 Paleozoic geologic history. American Journal of Science, 287: 177-196.
1681 Berner, R.A., 1989. Biogeochemical cycles of carbon and sulfur and their effect on atmospheric
1682 oxygen over Phanerozoic time. Global and Planetary Change, 75: 97-122.
1683 Berner, R.A., 1991. A model for atmospheric CO2 over Phanerozoic time. American Journal of
1684 Science, 291: 339-376.
1685 Berner, R.A., 1994. Geocarb II: A revised model of atmospheric CO2 over Phanerozoic time.
1686 American Journal of Science, 294: 56-91.
1687 Berner, R.A., 2006a. GEOCARBSULF: A combined model for Phanerozoic atmospheric O2 and CO2.
1688 Geochimica et Cosmochimica Acta, 70(23): 5653-5664.
1689 Berner, R.A., 2006b. Inclusion of the Weathering of Volcanic Rocks in the GEOCARBSULF Model.
1690 American Journal of Science, 306(5): 295-302.
1691 Berner, R.A., 2009. Phanerozoic atmospheric oxygen: New results using the GEOCARBSULF model.
1692 Am J Sci, 309(7): 603-606.
1693 Berner, R.A. and Canfield, D.E., 1989. A new model for atmospheric oxygen over Phanerozoic time.
1694 American Journal of Science, 289: 333-361.

1695 Berner, R.A. and Kothavala, Z., 2001. Geocarb III: A revised model of atmospheric CO2 over
1696 Phanerozoic time. American Journal of Science, 301: 182-204.
1697 Berner, R.A., Lasaga, A.C. and Garrels, R.M., 1983. The carbonate-silicate geochemical cycle and its
1698 effect on atmospheric carbon dioxide over the past 100 million years. American Journal of
1699 Science, 283: 641-683.
1700 Berner, R.A., Petsch, S.T., Lake, J.A., Beerling, D.J., Popp, B.N., Lane, R.S., Laws, E.A., Westley, M.B.,
1701 Cassar, N., Woodward, F.I. and Quick, W.P., 2000. Isotope Fractionation and Atmospheric
1702 Oxygen: Implications for Phanerozoic O2 Evolution. Science, 287: 1630-1633.
1703 Berner, R.A., VandenBrooks, J.M. and Ward, P.D., 2007. Oxygen and Evolution. Science, 316(5824):
1704 557-558.
1705 Betts, J.N. and Holland, H.D., 1991. The oxygen content of ocean bottom waters, the burial efficiency
1706 of organic carbon, and the regulation of atmospheric oxygen. Palaeogeography,
1707 Palaeoclimatology, Palaeoecology (Global and Planetary Change Section), 97: 5-18.
1708 Blair, N.E. and Aller, R.C., 2012. The Fate of Terrestrial Organic Carbon in the Marine Environment.
1709 Annual Review of Marine Science, 4(1): 401-423.
1710 Bluth, G.J.S. and Kump, L.R., 1991. Phanerozoic paleogeology. American Journal of Science, 291(3):
1711 284-308.
1712 Bond, W.J., Woodward, F.I. and Midgley, G.F., 2005. The global distribution of ecosystems in a world
1713 without fire. New Phytologist, 165: 525-538.
1714 Brennan, S.T., Lowenstein, T.K. and Horita, J., 2004. Seawater chemistry and the advent of
1715 biocalcification. Geology, 32(6): 473-476.
1716 Burdige, D.J., 2005. Burial of terrestrial organic matter in marine sediments: A re-assessment. Global
1717 Biogeochemical Cycles, 19(4): GB4011.
1718 Caldeira, K. and Kasting, J.F., 1992. The life span of the biosphere revisited. Nature, 360: 721-723.
1719 Canfield, D.E., 1998. A new model for Proterozoic ocean chemistry. Nature, 396: 450-453.

1720 Canfield, D.E., 2013. Sulfur isotopes in coal constrain the evolution of the Phanerozoic sulfur cycle.
1721 Proceedings of the National Academy of Sciences, 110(21): 8443-8446.
1722 Caves, J.K., Jost, A.B., Lau, K.V. and Maher, K., 2016. Cenozoic carbon cycle imbalances and a variable
1723 weathering feedback. Earth and Planetary Science Letters, 450: 152-163.
1724 Cohen, K.M., Finney, S.C., Gibbard, P.L. and Fan, J.-X., 2013; updated. The ICS International
1725 Chronostratigraphic Chart. Episodes, 36: 199-204.
1726 Compton, J., Mallinson, D., Glenn, C.R., Filippelli, G., Follmi, K., Shields, G. and Zanin, Y., 2000.
1727 Variations in the global phosphorus cycle. In: C.R. Glenn, L. Prevot-Lucas and J. Lucas
1728 (Editors), Marine Authigenesis: From Global to Microbial, SEPM Special Publication No. 66.
1729 SEPM (Society for Sedimentary Geology), pp. 21-33.
1730 Coogan, L.A. and Dosso, S.E., 2015. Alteration of ocean crust provides a strong temperature
1731 dependent feedback on the geological carbon cycle and is a primary driver of the Sr-isotopic
1732 composition of seawater. Earth and Planetary Science Letters, 415: 38-46.
1733 Cox, G.M., Halverson, G.P., Stevenson, R.K., Vokaty, M., Poirier, A., Kunzmann, M., Li, Z.-X.,
1734 Denyszyn, S.W., Strauss, J.V. and Macdonald, F.A., 2016. Continental flood basalt weathering
1735 as a trigger for Neoproterozoic Snowball Earth. Earth and Planetary Science Letters, 446: 89-
1736 99.
1737 Daines, S.J., Mills, B. and Lenton, T.M., 2017. Atmospheric oxygen regulation at low Proterozoic
1738 levels by incomplete oxidative weathering of sedimentary organic carbon. Nature
1739 Communications, 8: 14379.
1740 Dessert, C., Dupré, B., Gaillardet, J., François, L.M. and Allègre, C.J., 2003. Basalt weathering laws and
1741 the impact of basalt weathering on the global carbon cycle. Chemical Geology, 202(3-4):
1742 257-273.
1743 Donnadieu, Y., Goddéris, Y., Pierrehumbert, R., Dromart, G., Fluteau, F. and Jacob, R., 2006. A
1744 GEOCLIM simulation of climatic and biogeochemical consequences of Pangea breakup.
1745 Geochemistry, Geophysics, Geosystems, 7(11): Q11019.

1746 Edwards, D., Cherns, L. and Raven, J.A., 2015. Could land-based early photosynthesizing ecosystems
1747 have bioengineered the planet in mid-Palaeozoic times? Palaeontology, 58(5): 803-837.
1748 Engebretson, D.C., Kelley, K.P., Cashman, H.J. and Richards, M.A., 1992. 180 Million Years of
1749 Subduction. GSA Today, 2(5): 93-100.
1750 Ernst, R.E., 2014. Large Igneous Provinces. Cambridge University Press, Cambridge, UK.
1751 Falkowski, P.G., Katz, M.E., Milligan, A.J., Fennel, K., Cramer, B.S., Aubry, M.P., Berner, R.A., Novacek,
1752 M.J. and Zapol, W.M., 2005. The Rise of Oxygen over the Past 205 Million Years and the
1753 Evolution of Large Placental Mammals. Science, 309: 2202-2204.
1754 Francois, L.M. and Walker, J.C.G., 1992. Modelling the Phanerozoic carbon cycle and climate:
1755 Constraints from the $^{87}Sr/^{86}Sr$ isotopic ratio of seawater. American Journal of Science, 292:
1756 81-135.
1757 Gaffin, S., 1987. Ridge volume dependence on seafloor generation rate and inversion using long
1758 term sealevel change. American Journal of Science, 287(6): 596-611.
1759 Gaillardet, J., Dupré, B., Louvat, P. and Allègre, C.J., 1999. Global silicate weathering and CO2
1760 consumption rates deduced from the chemistry of large rivers. Chemical Geology, 159(1–4):
1761 3-30.
1762 Galy, V., Peucker-Ehrenbrink, B. and Eglinton, T., 2015. Global carbon export from the terrestrial
1763 biosphere controlled by erosion. Nature, 521(7551): 204-207.
1764 Garrels, R.M. and Lerman, A., 1981. Phanerozoic cycles of sedimentary carbon and sulfur.
1765 Proceedings of the National Academy of Sciences USA, 78(8): 4652-4656.
1766 Garrels, R.M. and Lerman, A., 1984. Coupling of the sedimentary sulfur and carbon cycles; an
1767 improved model. American Journal of Science, 284(9): 989-1007.
1768 Gillis, K.M. and Coogan, L.A., 2011. Secular variation in carbon uptake into the ocean crust. Earth and
1769 Planetary Science Letters, 302(3–4): 385-392.
1770 Glasspool, I.J., Edwards, D. and Axe, L., 2004. Charcoal in the Silurian as evidence for the earliest
1771 wildfire. Geology, 32(5): 381-383.

1772 Glasspool, I.J. and Scott, A.C., 2010. Phanerozoic concentrations of atmospheric oxygen
1773 reconstructed from sedimentary charcoal. Nature Geosci, 3(9): 627-630.
1774 Goddéris, Y., Donnadieu, Y., Le Hir, G., Lefebvre, V. and Nardin, E., 2014. The role of
1775 palaeogeography in the Phanerozoic history of atmospheric CO2 and climate. Earth-Science
1776 Reviews, 128: 122-138.
1777 Goddéris, Y., Le Hir, G., Macouin, M., Donnadieu, Y., Hubert-Théou, L., Dera, G., Aretz, M., Fluteau,
1778 F., Li, Z.X. and Halverson, G.P., 2017. Paleogeographic forcing of the strontium isotopic cycle
1779 in the Neoproterozoic. Gondwana Research, 42: 151-162.
1780 Graham, J.B., Dudley, R., Aguilar, N.M. and Gans, C., 1995. Implications of the late Palaeozoic oxygen
1781 pulse for physiology and evolution. Nature, 375: 117-120.
1782 Graham, J.B., Jew, C.J. and Wegner, N.C., 2016. Modeling Variable Phanerozoic Oxygen Effects on
1783 Physiology and Evolution. In: R.C. Roach, P.H. Hackett and P.D. Wagner (Editors), Hypoxia:
1784 Translation in Progress. Springer US, Boston, MA, pp. 409-426.
1785 Guidry, M.W., Arvidson, R.S. and Mackenzie, F.T., 2007. Biological and Geochemical Forcings to
1786 Phanerozoic Change in Seawater, Atmosphere and Carbonate Precipitate Composition. In:
1787 P.G. Falkowski and A.H. Knoll (Editors), Evolution of Primary Producers in the Sea. Academic
1788 Press, pp. 377-403.
1789 Halevy, I., Peters, S.E. and Fischer, W.W., 2012. Sulfate Burial Constraints on the Phanerozoic Sulfur
1790 Cycle. Science, 337(6092): 331-334.
1791 Halverson, G.P., Dudás, F.Ö., Maloof, A.C. and Bowring, S.A., 2007. Evolution of the 87Sr/86Sr
1792 composition of Neoproterozoic seawater. Palaeogeography, Palaeoclimatology,
1793 Palaeoecology, 256(3): 103-129.
1794 Haq, B.U., 2014. Cretaceous eustasy revisited. Global and Planetary Change, 113: 44-58.
1795 Haq, B.U. and Al-Qahtani, A.M., 2005. Phanerozoic cycles of sea-level change on the Arabian
1796 Platform. Geoarabia, 10: 127-160.

1797 Haq, B.U. and Schutter, S.R., 2008. A Chronology of Paleozoic Sea-Level Changes. Science, 322(5898):
1798 64-68.
1799 Hartmann, J., Jansen, N., Dürr, H.H., Kempe, S. and Köhler, P., 2009. Global CO2-consumption by
1800 chemical weathering: What is the contribution of highly active weathering regions? Global
1801 and Planetary Change, 69(4): 185-194.
1802 Hartmann, J., Moosdorf, N., Lauerwald, R., Hinderer, M. and West, A.J., 2014. Global chemical
1803 weathering and associated P-release — The role of lithology, temperature and soil
1804 properties. Chemical Geology, 363: 145-163.
1805 Hedges, J.I. and Keil, R.G., 1995. Sedimentary organic matter preservation: an assessment and
1806 speculative synthesis. Marine Chemistry, 49: 81-115.
1807 Helly, J.J. and Levin, L.A., 2004. Global distribution of naturally occurring marine hypoxia on
1808 continental margins. Deep Sea Research Part I: Oceanographic Research Papers, 51(9): 1159-
1809 1168.
1810 Holland, H.D., 1978. The Chemistry of the Atmosphere and Oceans. John Wiley.
1811 Horita, J., Zimmermann, H. and Holland, H.D., 2002. Chemical evolution of seawater during the
1812 Phanerozoic: Implications from the record of marine evaporites. Geochimica et
1813 Cosmochimica Acta, 66(21): 3733-3756.
1814 Horton, F., 2015. Did phosphorus derived from the weathering of large igneous provinces fertilize
1815 the Neoproterozoic ocean? Geochemistry, Geophysics, Geosystems, 16(6): 1723-1738.
1816 IPCC (Editor), 2013. Climate Change 2013: The Physical Science Basis. Contribution of Working Group
1817 I to the Fifth Assessment Report of the Intergovernmental Panel on Climate Change.
1818 Cambridge University Press, Cambridge, United Kingdom and New York, NY, USA, 1535 pp.
1819 Johnson, J.E., Gerpheide, A., Lamb, M.P. and Fischer, W.W., 2014. O2 constraints from
1820 Paleoproterozoic detrital pyrite and uraninite. Geological Society of America Bulletin, 126(5-
1821 6): 813-830.

1822 Kampschulte, A. and Strauss, H., 2004. The sulfur isotopic evolution of Phanerozoic seawater based
1823 on the analysis of structurally substituted sulfate in carbonates. Chemical Geology, 204(3–4):
1824 255-286.
1825 Kennedy, K.L., Gibling, M.R., Eble, C.F., Gastaldo, R.A., Gensel, P.G., Werner-Zwanziger, U. and
1826 Wilson, R.A., 2013. Lower Devonian coaly shales of northern New Brunswick, Canada: plant
1827 accumulations in the early stages of Terrestrial colonization. Journal of Sedimentary
1828 Research, 83(12): 1202-1215.
1829 Kolowith, L.C. and Berner, R.A., 2002. Weathering of phosphorus in black shales. Global
1830 Biogeochemical Cycles, 16(4): 1140.
1831 Kump, L.R., 1988. Terrestrial feedback in atmospheric oxygen regulation by fire and phosphorus.
1832 Nature, 335: 152-154.
1833 Kump, L.R. and Arthur, M.A., 1999. Interpreting carbon-isotope excursions: carbonates and organic
1834 matter. Chemical Geology, 161: 181-198.
1835 Lasaga, A.C., 1989. A new approach to isotope modeling of the variation of atmospheric oxygen
1836 through the Phanerozoic. American Journal of Science, 289: 411-435.
1837 Lee, C.-T.A., Shen, B., Slotnick, B.S., Liao, K., Dickens, G.R., Yokoyama, Y., Lenardic, A., Dasgupta, R.,
1838 Jellinek, M., Lackey, J.S., Schneider, T. and Tice, M.M., 2013. Continental arc–island arc
1839 fluctuations, growth of crustal carbonates, and long-term climate change. Geosphere, 9(1):
1840 21-36.
1841 Lenton, T.M., 2013. Fire Feedbacks on Atmospheric Oxygen. In: C.M. Belcher (Editor), Fire
1842 Phenomena and the Earth System: An Interdisciplinary Guide to Fire Science. Wiley-
1843 Blackwell, pp. 289-308.
1844 Lenton, T.M., Boyle, R.A., Poulton, S.W., Shields, G.A. and Butterfield, N.J., 2014. Co-evolution of
1845 eukaryotes and ocean oxygenation in the Neoproterozoic era. Nature Geoscience, 7(4): 257-
1846 265.

1847 Lenton, T.M., Crouch, M., Johnson, M., Pires, N. and Dolan, L., 2012. First plants cooled the
1848 Ordovician. Nature Geoscience, 5(2): 86-89.
1849 Lenton, T.M., Dahl, T.W., Daines, S.J., Mills, B.J.W., Ozaki, K., Saltzman, M.R. and Porada, P., 2016.
1850 Earliest land plants created modern levels of atmospheric oxygen. Proceedings of the
1851 National Academy of Sciences, 113(35): 9704-9709.
1852 Lenton, T.M. and Daines, S.J., 2017. Biogeochemical Transformations in the History of the Ocean.
1853 Annual Review of Marine Science, 9(1): 31-58.
1854 Lenton, T.M. and Watson, A.J., 2000a. Redfield revisited: 1. Regulation of nitrate, phosphate and
1855 oxygen in the ocean. Global Biogeochemical Cycles, 14(1): 225-248.
1856 Lenton, T.M. and Watson, A.J., 2000b. Redfield revisited: 2. What regulates the oxygen content of
1857 the atmosphere? Global Biogeochemical Cycles, 14(1): 249-268.
1858 Lenton, T.M. and Watson, A.J., 2011. Revolutions that made the Earth. Oxford University Press,
1859 Oxford.
1860 Li, G. and Elderfield, H., 2013. Evolution of carbon cycle over the past 100 million years. Geochimica
1861 et Cosmochimica Acta, 103(0): 11-25.
1862 Lowenstein, T.K., Timofeeff, M.N., Kovalevych, V.M. and Horita, J., 2005. The major-ion composition
1863 of Permian seawater. Geochimica et Cosmochimica Acta, 69(7): 1701-1719.
1864 Matthews, K.J., Maloney, K.T., Zahirovic, S., Williams, S.E., Seton, M. and Müller, R.D., 2016. Global
1865 plate boundary evolution and kinematics since the late Paleozoic. Global and Planetary
1866 Change, 146: 226-250.
1867 McArthur, J.M., Howarth, R.J. and Shields, G.A., 2012. Chapter 7 - Strontium Isotope Stratigraphy,
1868 The Geologic Time Scale. Elsevier, Boston, pp. 127-144.
1869 McKenzie, N.R., Horton, B.K., Loomis, S.E., Stockli, D.F., Planavsky, N.J. and Lee, C.-T.A., 2016.
1870 Continental arc volcanism as the principal driver of icehouse-greenhouse variability. Science,
1871 352(6284): 444-447.

1872 Mills, B., Daines, S.J. and Lenton, T.M., 2014a. Changing tectonic controls on the long-term carbon
1873 cycle from Mesozoic to present. Geochem. Geophys. Geosyst., 15: 4866-4884.
1874 Mills, B., Lenton, T.M. and Watson, A.J., 2014b. Proterozoic oxygen rise linked to shifting balance
1875 between seafloor and terrestrial weathering. PNAS, 111(25): 9073-9078.
1876 Mills, B., Watson, A.J., Goldblatt, C., Boyle, R. and Lenton, T.M., 2011. Timing of Neoproterozoic
1877 glaciations linked to transport-limited global weathering. Nature Geoscience, 4: 861-864.
1878 Mills, B.J.W., Belcher, C.M., Lenton, T.M. and Newton, R.J., 2016. A modeling case for high
1879 atmospheric oxygen concentrations during the Mesozoic and Cenozoic. Geology, 44(12):
1880 1023-1026.
1881 Mills, B.J.W., Scotese, C.R., Walding, N.G., Shields-Zhou, G.A. and Lenton, T.M., 2017. Elevated $CO_2$
1882 degassing rates prevented the return of Snowball Earth during the Phanerozoic. Nature
1883 Communications, 8: 1110.
1884 Monteiro, F.M., Pancost, R.D., Ridgwell, A. and Donnadieu, Y., 2012. Nutrients as the dominant
1885 control on the spread of anoxia and euxinia across the Cenomanian-Turonian oceanic anoxic
1886 event (OAE2): Model-data comparison. Paleoceanography, 27(4): PA4209.
1887 Moon, S., Chamberlain, C.P. and Hilley, G.E., 2014. New estimates of silicate weathering rates and
1888 their uncertainties in global rivers. Geochimica et Cosmochimica Acta, 134: 257-274.
1889 Moulton, K.L., West, J. and Berner, R.A., 2000. Solute flux and mineral mass balance approaches to
1890 the quantification of plant effects on silicate weathering. American Journal of Science,
1891 300(7): 539-570.
1892 Munhoven, G., 2002. Glacial–interglacial changes of continental weathering: estimates of the related
1893 CO2 and HCO3− flux variations and their uncertainties. Global and Planetary Change, 33(1–
1894 2): 155-176.
1895 Nelsen, M.P., DiMichele, W.A., Peters, S.E. and Boyce, C.K., 2016. Delayed fungal evolution did not
1896 cause the Paleozoic peak in coal production. Proceedings of the National Academy of
1897 Sciences, 113(9): 2442-2447.

1898 Ozaki, K. and Tajika, E., 2013. Biogeochemical effects of atmospheric oxygen concentration,
1899 phosphorus weathering, and sea-level stand on oceanic redox chemistry: Implications for
1900 greenhouse climates. Earth and Planetary Science Letters, 373: 129-139.
1901 Ozaki, K., Tajima, S. and Tajika, E., 2011. Conditions required for oceanic anoxia/euxinia: Constraints
1902 from a one-dimensional ocean biogeochemical cycle model. Earth and Planetary Science
1903 Letters, 304(1-2): 270-279.
1904 Paytan, A., Kastner, M., Campbell, D. and Thiemens, M.H., 1998. Sulfur Isotopic Composition of
1905 Cenozoic Seawater Sulfate. Science, 282(5393): 1459-1462.
1906 Planavsky, N.J., Rouxel, O.J., Bekker, A., Lalonde, S.V., Konhauser, K.O., Reinhard, C.T. and Lyons,
1907 T.W., 2010. The evolution of the marine phosphate reservoir. Nature, 467(7319): 1088-1090.
1908 Pohl, A., Donnadieu, Y., Le Hir, G., Buoncristiani, J.F. and Vennin, E., 2014. Effect of the Ordovician
1909 paleogeography on the (in)stability of the climate. Clim. Past, 10(6): 2053-2066.
1910 Pohl, A., Donnadieu, Y., Le Hir, G., Ladant, J.-B., Dumas, C., Alvarez-Solas, J. and Vandenbroucke,
1911 T.R.A., 2016. Glacial onset predated Late Ordovician climate cooling. Paleoceanography,
1912 31(6): 800-821.
1913 Porada, P., Lenton, T.M., Pohl, A., Weber, B., Mander, L., Donnadieu, Y., Beer, C., Poschl, U. and
1914 Kleidon, A., 2016. High potential for weathering and climate effects of non-vascular
1915 vegetation in the Late Ordovician. Nature Communications, 7: 12113.
1916 Quirk, J., Leake, J.R., Johnson, D.A., Taylor, L.L., Saccone, L. and Beerling, D.J., 2015. Constraining the
1917 role of early land plants in Palaeozoic weathering and global cooling. Proceedings of the
1918 Royal Society of London B: Biological Sciences, 282(1813).
1919 Regnier, P., Friedlingstein, P., Ciais, P., Mackenzie, F.T., Gruber, N., Janssens, I.A., Laruelle, G.G.,
1920 Lauerwald, R., Luyssaert, S., Andersson, A.J., Arndt, S., Arnosti, C., Borges, A.V., Dale, A.W.,
1921 Gallego-Sala, A., Goddéris, Y., Goossens, N., Hartmann, J., Heinze, C., Ilyina, T., Joos, F.,
1922 LaRowe, D.E., Leifeld, J., Meysman, F.J.R., Munhoven, G., Raymond, P.A., Spahni, R.,

1923 Suntharalingam, P. and Thullner, M., 2013. Anthropogenic perturbation of the carbon fluxes
1924 from land to ocean. Nature Geosci, 6(8): 597-607.
1925 Ronov, A.B., 1993. Stratisfera-Ili Osadochnaya Obolochka Zemli (Kolichestvennoe Issledovanie).
1926 Nauka, Moskva.
1927 Royer, D.L., 2014. Atmospheric CO2 and O2 During the Phanerozoic: Tools, Patterns, and Impacts. In:
1928 H.D. Holland and K.K. Turekian (Editors), Treatise on Geochemistry (Second Edition). Elsevier,
1929 Oxford, pp. 251-267.
1930 Royer, D.L., Berner, R.A. and Park, J., 2007. Climate sensitivity constrained by CO2 concentrations
1931 over the past 420[thinsp]million years. Nature, 446(7135): 530-532.
1932 Royer, D.L., Donnadieu, Y., Park, J., Kowalczyk, J. and Goddéris, Y., 2014. Error analysis of CO2 and O2
1933 estimates from the long-term geochemical model GEOCARBSULF. American Journal of
1934 Science, 314(9): 1259-1283.
1935 Saltzman, M.R. and Thomas, E., 2012. Chapter 11 - Carbon Isotope Stratigraphy. In: F.M. Gradstein,
1936 J.G.O.D. Schmitz and G.M. Ogg (Editors), The Geologic Time Scale. Elsevier, Boston, pp. 207-
1937 232.
1938 Schaller, M.F., Wright, J.D. and Kent, D.V., 2011. Atmospheric Pco2 Perturbations Associated with
1939 the Central Atlantic Magmatic Province. Science, 331(6023): 1404-1409.
1940 Scott, A.C. and Glaspool, I.J., 2006. The diversification of Paleozoic fire systems and fluctuations in
1941 atmospheric oxygen concentration. Proceedings of the National Academy of Sciences of the
1942 United States of America, 103(29): 10861-10865.
1943 Shampine, L.F. and Reichelt, M.W., 1997. The MATLAB ODE Suite. SIAM Journal on Scientific
1944 Computing, 18(1): 1-22.
1945 Sleep, N.H., 2005. Dioxygen over geological time. In: A. Sigel, H. Sigel and R.K.O. Sigel (Editors), Metal
1946 Ions in Biological Systems, Volume 43 - Biogeochemical Cycles of Elements. Taylor & Francis,
1947 Boca Raton, FL, pp. 49-73.

1948 Slomp, C.P. and Van Cappellen, P., 2007. The global marine phosphorus cycle: sensitivity to oceanic
1949 circulation. Biogeosciences, 4(2): 155-171.
1950 Sperling, E.A., Knoll, A.H. and Girguis, P.R., 2015a. The Ecological Physiology of Earth's Second
1951 Oxygen Revolution. Annual Review of Earth and Planetary Sciences, 46: 215-235.
1952 Sperling, E.A., Wolock, C.J., Morgan, A.S., Gill, B.C., Kunzmann, M., Halverson, G.P., Macdonald, F.A.,
1953 Knoll, A.H. and Johnston, D.T., 2015b. Statistical analysis of iron geochemical data suggests
1954 limited late Proterozoic oxygenation. Nature, 523(7561): 451-454.
1955 Staudigel, H., Hart, S.R., Schmincke, H.-U. and Smith, B.M., 1989. Cretaceous ocean crust at DSDP
1956 Sites 417 and 418: Carbon uptake from weathering versus loss by magmatic outgassing.
1957 Geochimica et Cosmochimica Acta, 53(11): 3091-3094.
1958 Torres, M.A., West, A.J. and Li, G., 2014. Sulphide oxidation and carbonate dissolution as a source of
1959 CO2 over geological timescales. Nature, 507(7492): 346-349.
1960 Tostevin, R., Turchyn, A.V., Farquhar, J., Johnston, D.T., Eldridge, D.L., Bishop, J.K.B. and McIlvin, M.,
1961 2014. Multiple sulfur isotope constraints on the modern sulfur cycle. Earth and Planetary
1962 Science Letters, 396: 14-21.
1963 Van Cappellen, P. and Ingall, E.D., 1994. Benthic phosphorus regeneration, net primary production,
1964 and ocean anoxia: A model of the coupled marine biogeochemical cycles of carbon and
1965 phosphorus. Paleoceanography, 9: 677-692.
1966 Van Cappellen, P. and Ingall, E.D., 1996. Redox stabilisation of the Atmosphere and Oceans by
1967 Phosphorus-Limited Marine Productivity. Science, 271: 493-496.
1968 Van Der Meer, D.G., Zeebe, R.E., van Hinsbergen, D.J.J., Sluijs, A., Spakman, W. and Torsvik, T.H.,
1969 2014. Plate tectonic controls on atmospheric CO2 levels since the Triassic. Proceedings of
1970 the National Academy of Sciences, 111(12): 4380-4385.
1971 Veizer, J. and Mackenzie, F.T., 2003. Evolution of Sedimentary Rocks, Treatise on Geochemistry:
1972 Sediments, Diagenesis and Sedimentary Rocks. Elsevier, pp. 369-407.

1973 Vollstaedt, H., Eisenhauer, A., Wallmann, K., Böhm, F., Fietzke, J., Liebetrau, V., Krabbenhöft, A.,
1974 Farkaš, J., Tomašových, A., Raddatz, J. and Veizer, J., 2014. The Phanerozoic δ88/86Sr record
1975 of seawater: New constraints on past changes in oceanic carbonate fluxes. Geochimica et
1976 Cosmochimica Acta, 128: 249-265.
1977 Walker, J.C.G., Hays, P.B. and Kasting, J.F., 1981. A negative feedback mechanism for the long-term
1978 stabilisation of Earth's surface temperature. Journal of Geophysical Research, 86(C10): 9776-
1979 9782.
1980 Willenbring, J.K. and von Blanckenburg, F., 2010. Long-term stability of global erosion rates and
1981 weathering during late-Cenozoic cooling. Nature, 465(7295): 211-214.

1982